

UNIVERSITÄT BASEL
Basel

**The reaction flow during
explosive nuclear burning on an
accreting neutron star**

Inauguraldissertation

zur

Erlangung der Würde eines Doktors der Philosophie

vorgelegt der

Philosophisch-Naturwissenschaftlichen Fakultät
der Universität Basel

von

Jacob Lund Fisker
aus Dänemark

Basel, 2005

Genehmigt von der Philosophisch-Naturwissenschaftlichen Fakultät
auf Antrag von
Prof. Dr. F.-K. Thielemann und Prof. Dr. H. Schatz
(Mitglieder des Dissertationskomitees)

Basel, den 3. Februar 2004
(Datum der Fakultätssitzung)

Prof. Dr. M. Tanner
Dekan

Contents

1	Introduction	1
1.1	The astrophysical site	1
1.2	The neutron star atmosphere	3
1.2.1	The thermal instability	3
1.3	Nuclear reactions	5
1.3.1	The thermonuclear runaway	6
1.3.2	Breakout and explosive burning	6
1.4	Why investigate the reaction flow?	7
1.4.1	A list of reasons	8
1.5	Theory vs. observations	10
1.5.1	The observational constraints	10
1.6	Goals of this work	12
2	Modeling the X-ray burst	13
2.1	Numerical models of the reaction flow	13
2.1.1	A new 1D multi-zone burst model	15
2.2	Computational outlay and details	16
2.2.1	Setup	17
2.3	Model analysis	18
2.3.1	Goals of the analysis	20
3	The Mixed H/He ignited flash	21
3.1	Quiescent burning	21
3.1.1	Quiescent <i>rp</i> -process	25
3.2	Explosive burning	26
3.2.1	Ignition point	29
3.2.2	Above the ignition point	35
3.2.3	Convective region	42
3.2.4	Surface	44
3.2.5	Ocean (ashes)	45

4	The He ignited flash	49
4.1	The He flash	49
4.2	<i>sd</i> -shell structure	51
4.2.1	The waiting point isotopes	52
4.2.2	The paths around the waiting points	53
4.3	The reaction flow	53
4.4	Observational features (double peaks)	56
4.4.1	Mass ejection and spectral lines	57
4.5	Specific reaction rate effects	58
4.5.1	$^{30}\text{S}(\alpha, p)^{33}\text{Cl}$ and $^{34}\text{Ar}(\alpha, p)^{37}\text{K}$	58
5	Summary	63
A	The computational model	65
A.1	General discussion	65
A.2	Hydrodynamics	66
A.2.1	Shift vector solution	66
A.2.2	Adaptive grid modification	68
A.3	Boundary conditions	69
A.3.1	The outer boundary	70
A.3.2	The grey photosphere	70
A.3.3	The ocean	72
A.4	Opacities and conductance	72
A.5	Convection	74
A.5.1	Shortcomings of mixing length theory	75
A.6	Equation of state	76
A.7	Neutrino bremsstrahlung	76
A.8	Reaction network	77

Abstract: This dissertation contains the first extensive investigation of the detailed reaction flow of an X-ray burst under realistic conditions. It was made possible by building a new computational model. This model distinguishes itself by introducing for the first time: full general relativistic (GR) hydrodynamical equations, GR corrected atmosphere, GR corrected convection, modern approximations of the opacities and conductivities, neutrino losses, and a GR inner boundary of the core luminosity.

We use conservative equations allowing a precise tracking off all released energy which reveals unprecedented details in the luminosity. The simulations show that –

- An interplay between the helium flash and the rp-process produces an identifiable double-peaked structure, which has been observed.
- The burst temperature is lower than previously assumed, so the Te-cycle is not reached. The average mass of the ashes is ~ 64 . Carbon is destroyed by helium captures before reaching the ocean.
- Convection does not hit the surface for mixed hydrogen/helium bursts. Therefore we predict that burst spectral lines are not from material from deeper layers.
- Convection extends to the surface in helium ignited bursts. We predict a sudden rise in helium and sulfur as the turbulent overturn breaches the surface.

We also give a complete description of the X-ray burst reaction flow including branchings and waiting points as a guide to future experiments and observations.

Chapter 1

Introduction

The purpose of this dissertation is to understand the nuclear reaction flow during an X-ray burst on an accreting neutron star. This will be done by coupling a detailed yet tractable numerical hydrodynamical model to a reaction network. This coupling is crucial, since charged particle capture rates depend strongly on the correct temperature, density and the material composition, which must therefore be as realistic as possible. Following a general introduction of the field and a review of other models of the reaction flow, two models are computed, where the reaction flow and its relevance to observations is analysed in detail.

1.1 The astrophysical site

According to Lewin et al. (1995) and Liu et al. (2001) the 63 known X-ray burst (XRB) sources are all low mass X-ray binaries¹ (LMXB) containing a neutron star and low mass ($M \leq 1M_{\odot}$) secondary which is either a late-type main sequence star, a white dwarf, or a giant branch star. Exceeding the

¹The formation and evolution of such a system is rather exotic and subjected to several constraints which partially explain the rarity of the LMBXs though no quantitative results can be given (Kalogera & Webbink (1998)). The progenitor is based on a massive primary which must fill its Roche lobe and transfer mass to the secondary on a timescale which is much shorter than both the nuclear and the thermal timescale of the secondary. This calls for an extreme mass ratio. Yet since the donated matter does not thermally relax onto the secondary, it ensures the development of a common envelope. This significantly reduces the orbital radius and period, which can be reduced to the order of hours (Pedersen et al. (1981)). Following the common envelope phase the primary has turned into a bare helium star, which turns into a neutron star following a supernova explosion. If the supernova explosion is asymmetric, the kick velocity must be sufficiently small, so the binary is not destroyed (Kalogera (1998)). The reverse mass transfer from the secondary to the primary, which is now a neutron star, must subsequently be sufficiently slow to allow enough of these systems to remain observable.

Roche lobe of the secondary (donor) by orbital shrinkage from loss of angular momentum due to gravitational radiation or by nuclear evolution starts a mass transfer to the neutron star (accretor), where it eventually impacts and lights up the otherwise unremarkable binary to make it observable (see Kalogera & Webbink (1996)). It is crucial that the rate of mass transfer is below the Eddington critical accretion rate², so the site survives sufficiently long to observe it (van den Heuvel (1975)).

If the angular momentum of the thin stream of matter, which is transferred through the first Lagrange point, exceeds $\sim r_I c$, where r_I is the radius of the innermost stable orbit, it forms an accretion disk (Prendergast & Burbidge (1968)). Entering the disk, matter, which may even be burning (Taam (1985)), interacts energetically by turbulence and magnetic fields, until it is either deposited on the neutron star surface or returned to the donor star or entirely thrown out of the system through the second Lagrange point (Shapiro & Teukolsky (1983)). In the disk about half of the potential energy of the matter stream is dissipated by hydrodynamical and magnetic turbulence while the rest is dissipated close to the neutron star surface, where the matter decelerates from the Keplerian velocity to the spin velocity of the neutron star surface (Lapidus & Sunyaev (1985)). This heats the photosphere to a few hundred million degrees resulting in a persistent X-ray emission which escapes since the photosphere (by definition) is transparent to X-rays (Hansen & van Horn (1975)). Assuming that matter enters from infinity, the total energy release from mass transfer is given by

$$L = \left[1 - \sqrt{1 - 2GM/Rc^2}\right] \dot{M}c^2 \approx \frac{GM}{R} \dot{M}, \quad (1.1)$$

where c is the speed of light, $G = 6.673 \cdot 10^{-8} \text{ dyn cm}^2 \text{ g}^{-2}$ is the gravitational constant, M and R is the gravitational mass and the local radius of the NS respectively, where $GM/R \sim 180 \text{ MeV s nucleon}^{-1}$ and \dot{M} is the total mass transfer rate. Since the total persistent luminosity includes $> 10\%$ disk luminosity and since it depends on the geometry of the accretion flow, the luminosity is not a precise indicator of the instantaneous accretion rate, which fluctuates in time (van der Klis et al. (1990)).

The accreted material has the isotopic composition of the donor star's surface, which is a mixture of hydrogen and helium for late-type zero-age main sequence (ZAMS) donors or pure helium for white dwarf donors (giant branch donors are rare). Since the neutron star surface has a gravitational

²While not very relevant to neutron star bursters by itself, the Eddington critical accretion rate is useful as a measuring stick, because it yields "convenient" numbers. It equals $1.1 \cdot 10^{18} \text{ g/s}$ and assumes temperature independent Thompson scattering in an atmosphere with a solar composition for a standard NS of $M = 1.4M_{\odot}$ and $R = 10 \text{ km}$.

field of $g \sim 10^{14} \text{ cm s}^{-2}$ the hydrostatic balance requires a very high pressure and thus a density which is far in excess of the densities found in any other stellar object. The combination of high pressures and high temperatures eventually allows the hydrogen and helium to fusion beyond ^{56}Fe and release energy.

As the gravitational energy release of eq. [1.1] is $\sim 180 \text{ MeV nucleon}^{-1}$ and the nuclear energy release is only $Q_{nuc} \sim 8.4 \text{ MeV nucleon}^{-1}$ for hydrogen burning and $Q_{nuc} \sim 1.7 \text{ MeV nucleon}^{-1}$ for helium burning (Lewin et al. (1995); Bildsten (1998b)), the nuclear aspect of the site would not be observable, if the nuclear energy could not be stored and released in a burst, where it exceeds the persistent luminosity by a couple of orders of magnitude.

1.2 The neutron star atmosphere

Following the collision of the accreted matter with the photosphere the now fully ionized matter slowly sinks into the NS atmosphere (see Fig. 1.1) while undergoing a gradual compression as freshly accreted matter is continuously piled on top. Spatial compression of electron wavefunctions quickly fills the available electron phase-space and makes the electrons degenerate, so they effectively approximate a stiff temperature-independent Fermi-Dirac gas. The nuclei behave differently: Since the Compton wavelength of the nuclei is much shorter, the phase-space is not filled and the nuclei behave like a temperature dependent ideal gas³.

1.2.1 The thermal instability

However, the partial pressure of the thermal nuclei is small compared to the partial degenerate pressure of the electrons, whence the total pressure of the ionized gas hydrodynamically behaves like a degenerate gas. This means that the atmosphere does not respond to perturbations in temperature by expanding or contracting like ordinary stars. Instead it has to rely on heat transport by radiation, conduction, or convection. This allows a “thin-shell” thermal instability, which was initially discussed by Hansen & van Horn (1975) and identified as the cause of the observable XRB by Woosley & Taam (1976) already within a year of the independent discoveries of the first

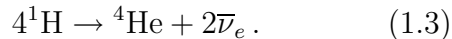
³It is only when the matter sinks into the crust that increasing densities make the nucleons degenerate and the electron Fermi energy exceeds the chemical potential of the $e^- + p \rightarrow n + \nu_e$ reaction turning the matter into free neutrons from which the neutron star derives its name. This also explains why neutron induced reactions are negligible in the XRB.

XRB by Grindlay et al. (1976) and Belian et al. (1976). In a degenerate atmosphere such an instability obtains and ensures a runaway, if and only if the nuclear energy release rate becomes more sensitive to temperature perturbations than the corresponding cooling rate (Rakavy & Shaviv (1967))

$$\frac{d\epsilon_{nuc}}{dT} \geq \frac{d\epsilon_{cool}}{dT}, \quad (1.2)$$

where ϵ_{cool} is the divergence of the heat flux and ϵ_{nuc} is the time rate of nuclear energy release.

The temperature sensitivity of the nuclear energy release changes as the dominating nuclear reaction type changes from hydrogen burning to helium burning as the matter moves into the star (Joss (1981). Starting at the surface with temperatures of 0.1–0.2 billion Kelvin the most important process is the hot-CNO cycle (see Audouze et al. (1973) and references therein) whose net reaction is the helium producing reaction



Since the β^+ -decays of ^{14}O ($T_{1/2} = 76.4\text{s}$) and ^{15}O ($T_{1/2} = 122.2\text{s}$) are much slower than the proton captures in the cycle for this temperature range, the hot CNO cycle quickly saturates and becomes temperature independent. A thermal runaway is impossible before the reactions in the matter become thermally sensitive either by the triple-alpha reaction or by the rp -process (Wallace & Woosley (1981); van Wormer et al. (1994); Schatz et al. (1998)), which starts from a *break out* from the long-lived oxygen isotopes in the hot CNO cycle

(Wiescher et al. (1999)). The exact nature of the trigger depends on the material composition at the point of ignition which depends on the accretion rate and the neutron star mass and radius (see sections 2.2 and 3.1, and appendix A) (Fushiki & Lamb (1987)). Due to the asymmetry of magnetic fields, rotation, and the gravitational interaction with the secondary, it is unlikely that the runaway starts simultaneously over the entire surface, so the ignition gives rise to a propagating burning front, which ignites other parts of the star (Shara (1982); Miller (1999)). If the matter is ignited at a density

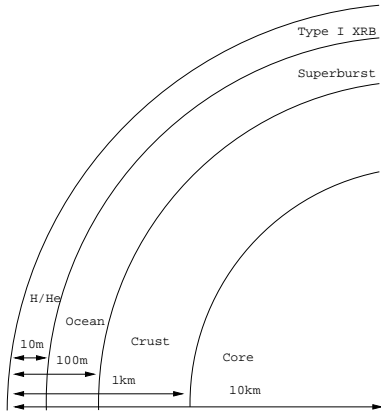


Figure 1.1: A cut through the NS showing the shell structure along with the physics of that region. Since the time scale between different shells differ widely the boundaries do not need dynamical treatment (see appendix A.1).

larger than $\rho > 10^8 \text{ g cm}^{-3}$, which may be the case for a helium accreting neutron star with a slow accretion rate, the burning spreads by a detonation wave moving with a velocity of $\sim 10^9 \text{ cm s}^{-1}$ (Fryxell & Woosley (1982b)). If the matter ignites in a thin shell with at a lower density of $\rho < 10^7 \text{ g cm}^{-3}$ the burning proceeds via a convective deflagration front, which is about a meter wide and moves with a velocity of $v \sim 5 \cdot 10^5 \text{ cm s}^{-1}$ circumnavigating the neutron star in $\tau \sim \pi R/v \sim 2\text{s}$ (Fryxell & Woosley (1982a)). The combination of asymmetric hot zones, which exist prior to the global ignition of the neutron star atmosphere, and the rotational period of the neutron star causes quasi-periodic oscillations (QPOs) in the luminosity (Strohmayer et al. (1998); Spitkovsky et al. (2002)). If convection is absent, the burning spreads slowly ($v \sim 300 \text{ cm/s}$) by conduction resulting in "rings of fire" whose asymmetry also yields QPOs (Bildsten (1993, 1995)).

1.3 Nuclear reactions

The nucleon momentum is on average much larger than the electron momentum because of the equipartition theorem and therefore the nucleons are non-degenerate and Boltzmann distributed. The *reaction rate* between two nuclei, i and j , is proportional to their densities and their reaction cross section folded with the distribution function of the relative energy between the two Boltzmann distributions in the center-of-mass system (Fowler et al. (1967); Cox & Guili (1968))

$$\langle \sigma v \rangle = \sqrt{\frac{8}{\pi \mu}} \frac{1}{k_B T^{3/2}} \int_0^\infty \sigma_{i,j}(E) E \exp(-E/k_B T) dE, \quad (1.4)$$

where μ is the reduced mass and T is the stellar temperature.

The reaction rates which determine the reaction flow are *ceteris paribus* sensitive to density and temperature of the stellar environment; the reaction rate scales linearly with the density for two particle reactions and quadratically for three particle reactions, and the temperature determines the location and width of the Gamow window, which essentially determines which resonances that contribute to the cross section.

Thus the reaction rate is uncertain due to uncertainties in the hydrodynamical model but also due to uncertainties in the number, position, and strength (energy, spectroscopic factor, and spin) of the resonances. In addition the reverse rate is very sensitive to the Q -value, which again depend on masses. This is most important for reactions between highly radioactive isotopes close to the proton drip-line where the uncertainty in mass-values causes a noticeable difference in the reaction flow (e.g. Brown et al. (2002)).

1.3.1 The thermonuclear runaway

If matter burns as fast as it is accreted the burning is *stable* (Rembges (1999); Schatz et al. (1999); Fisker et al. (2003)), otherwise unburned matter accumulates on the surface until it eventually ignites.

The electrons are degenerate and therefore an increase in temperature, which is nothing more than a change in the distribution function, does not change the electron distribution and thus does not change the pressure to any large extent. The nucleons, however, respond by moving faster which furthers the reactions in a positive feedback. Therefore the condition for the thermonuclear runaway (eq. [1.2]) depends on the temperature-sensitivity of the sum of the nuclear energy generation rate over all possible reactions

$$\epsilon_{nuc} = \sum \epsilon_i, \quad (1.5)$$

where a few reactions tend to dominate the thermal release, which feeds back and increases all reaction rates until the runaway ensues. The leading reaction, which triggers the runaway is the the triple-alpha reaction (Nomoto et al. (1985)). This reaction converts three ${}^4\text{He}$ nuclei into ${}^{12}\text{C}$ which is very sensitive to the helium concentration as well as the temperature, whence it violates eq. [1.2] once the accreted matter reaches a specific depth. The ensuing energy generation from the triple-alpha reaction heats the matter sufficient to trigger the *break-out* reactions, which involve the most abundant isotopes in the hot CNO cycle: ${}^{14}\text{O}$ and ${}^{15}\text{O}$.

1.3.2 Breakout and explosive burning

Prior to the runaway most of the material at the ignition point is in the form of hydrogen (${}^1\text{H}$), helium (${}^4\text{He}$), and oxygen (${}^{14}\text{O}$, ${}^{15}\text{O}$), and since the triple alpha process creates carbon, few heavier particles can be made barring a break out of the hot CNO cycle.

The hot CNO break-out reactions are ${}^{14}\text{O}(\alpha, p) {}^{17}\text{F}(p, \gamma) {}^{18}\text{Ne}(\alpha, p) {}^{21}\text{Ne}$ and ${}^{15}\text{O}(\alpha, \gamma) {}^{19}\text{Ne}$ (Audouze et al. (1973); Wiescher et al. (1999)). While there are no paths which return to the hot CNO cycle from ${}^{19}\text{Ne}$, ${}^{18}\text{Ne}$ can β^+ -decay ($T_{1/2} = 1.67\text{s}$) to ${}^{18}\text{F}$ whose proton capture is alpha unbound returning to ${}^{15}\text{O}$ (Wiescher et al. (1986)). This cycle is known as the hot CNO bi-cycle from which a break-out is possible once the a ${}^{18}\text{Ne}(\alpha, p) {}^{21}\text{Ne}$ -reaction becomes stronger than the β^+ -decay (Groombridge et al. (2002)).

Following the breakout of the hot CNO cycle the flow up to ${}^{40}\text{Ca}$ is determined by a competition between the (α, p) process (Wallace & Woosley (1981)), which is very temperature dependent, because of the strong Coloumb-barrier against alpha-capture, and the *rp*-process (rapid proton

process) (Wallace & Woosley (1981); van Wormer et al. (1994); Schatz et al. (1998)), which is a competition between very fast proton captures and β^+ -decays and therefore only temperature dependent in the sense that the temperature determines the ratio of the proton-rich isotopes within an isotone and thus which isotopes β^+ -decay and move the flow between the isotonic chains (Rembges et al. (1997)). For high temperatures photodisintegration prevents the formation of isotopes with low proton separation energies (Thielemann et al. (1994)), causing the reaction flow to pass through longer-lived less proton-rich isotopes (Brown et al. (2002)).

Unless the hydrogen is exhausted earlier, the rp -process continues beyond the iron-group nuclei, until the end-point is reached at ^{107}Te and ^{108}Te where the rp -process is definitely terminated by (γ, α) -photodisintegration (Schatz et al. (2001a)).

1.4 Why investigate the reaction flow?

The reaction flow is determined by the temperature, density, and composition, which vary in time and depth during the burst and from burster to burster and the nuclear structure data that determine the properties of the reactions, which are identical to all bursters.

The number of potentially relevant weak (decay) and strong (particle) reactions range in the thousands and are generally only known theoretically due to the presently unsurmountable task of measuring them. They are assembled from large compilations such as Fowler et al. (1967), Fowler et al. (1975), Woosley et al. (1978), Rauscher & Thielemann (2000), Fisker et al. (2001a), and Iliadis et al. (2001) bolstered by experimentally measured reaction rates. Measuring such rates are generally difficult due to the highly radioactive isotopes involved and time-consuming due to the sometimes very weak rates requiring a lot of data to get good statistics.

In many cases the theoretical determination of reaction rates is flawed with uncertainties of many orders of magnitude due to uncertainties in the number, position and strength of the resonances (Rauscher et al. (1997); Iliadis et al. (2001)). However, it is an enormous undertaking to measure all rates some of which might not even be relevant, because conditions are never such that those reactions either become active during a burst or are active at all during the quiescent phase. To alleviate the situation and resolve which reactions really matter, several investigations of the reaction flow has been undertaken (see section 2.1) typically for fixed temperatures and densities (post-processing) (Champagne & Wiescher (1992); van Wormer et al. (1994); Schatz et al. (1998)) but also using simple “one-zone” models (Hanawa &

Sugimoto (1983); Koike et al. (1999)), and more complicated “multi-zone” models (Woosley et al. (2004)). A resolution has become more urgent since facilities such as GANIL, GSI, NSCl/MSU, and ISOLDE/CERN, or the planned RIA, where recent developments in experimental methods has made high-intensity radioactive ion beams (RIB) possible, have put or will put more reactions within the reach of experimenters (Wiescher (2001); Wiescher & Schatz (2001); Schatz (2002)). It is therefore necessary to know which reactions are important and which to measure. A naive and all-inclusive approach would be to measure all reaction rates in the flow. However, some rates in the flow are more important than others. Therefore theoretical simulations are necessary to determine the most important reactions. Since the timescale to reach nuclear equilibrium is longer but comparable to the hydrodynamical timescale, the interaction with the hydrodynamics should not be overly simplified. In addition both temperature and density evolution as well as the exact accreted fuel mixture at the burning location are important to determine the reaction flow of the explosive hydrogen burning.

1.4.1 A list of reasons

- The reaction flow determines the composition of the ashes which influence many aspects of the NS (Miralda-Escudé et al. (1990)):
 - The heat transport, which self-consistently feeds back to determine the temperature profile of the burning region.
 - It determines crustal properties such as the electric conductivity, which is related to the Ohmic dissipation rate of the magnetic field (Haensel et al. (1990); Urpin & Geppert (1995); Pethick & Sahrling (1995)), the amount of heat deposited directly in the crust (Miralda-Escudé et al. (1990); Haensel & Zdunik (1990)), and the competing neutrino loss rate (Haensel et al. (1996)), both of which determine the equilibrium core temperature relevant for probing the equation of state of the interior neutron star (Brown & Bildsten (1998)).
 - Additionally it has been speculated (Bildsten & Cutler (1995); Bildsten & Cumming (1998)) that yet unobserved ocean g-modes which also depend on the crustal composition may provide an explanation for the quasi-periodic oscillations which has been observed in Z sources (see Hasinger & van der Klis (1989)).
 - Fluctuations in the very temperature-sensitive e^- -capture reactions in the sinking XRB ashes cause horizontal density varia-

tions in the crust layers resulting in a mass quadrupole moment which emits gravitational radiation. This would be detectable by future gravitational wave interferometers (Bildsten (1998a) and Ushomirsky et al. (2000)).

- It is an important factor to decide whether the current theory of the eight observed superbursts is viable since the composition of the ashes provide the fuel for the superburst (Cumming & Bildsten (2001); Schatz et al. (2003), and Irion (2002) for a popular account).
- Some superbursts have shown progenitors, which look like type I X-ray bursts (Strohmayer & Brown (2002)) suggesting that superbursts are somehow connected with ordinary type I bursts, which also cease following a month after the superburst (Kuulkers (2002); Cornelisse et al. (2002)). Cumming & Bildsten (2001) suggested that this is because the H/He bursting layers are thermally stabilized by the heat flux from the crustal carbon layer.
- Convection may bring deep material to the surface, though this is excluded in static simulations, since the inverse entropic gradient in a radiation dominated atmosphere ensures convective stability. Yet inertial turbulence (Kuhfuss (1986)), which is visibly demonstrated by the FLASH-code simulations, shows that matter may be thrown up as much as 10km (Zingale et al. (2001)), where the composition might be observed directly from the now nonthermalized spectral lines (London et al. (1986)) which the newest X-ray satellites are capable of observing (Bautista et al. (1998); Asai et al. (2000); Cottam et al. (2002); Parmar et al. (2002)).
- The mass-radius relation, which is important to constrain the possible nuclear equations of state of the NS, can be derived from the burst spectrum (Swank et al. (1977); Marshall (1982)). This would also be possible through direct identification of spectral emission lines (Lewin et al. (1995)).
- Fisker et al. (2004) has shown that significant waiting points in the reaction flow directly influence the bolometric luminosity of the burst. However, this initial study was limited to the reactions of only four isotopes.
- If matter expulsion is possible (see section 1.1) then XRBs might contribute to p -nuclei nucleosynthesis (Schatz et al. (2001a)).

- The type of burning determines the transition point between stable and unstable burning (Rembges (1999) and Fisker et al. (2003)). The transition point can be used to constrict the accretion area i.e. to determine whether B-fields funnel accreted matter onto a limited area of the neutron star (Bildsten & Brown (1997)).
- Koike et al. (1999), Fisker et al. (2001b) and Wiescher et al. (2002) showed that specific reactions affect the burst behavior. Preliminary runs also show that the recurrence time and therefore the peak luminosity and total burst energy are also affected (see Taam (1982) and references therein for other theories).

1.5 Theory vs. observations

Another challenge is the need to keep up with the increasing amount of ever more detailed observations: Following the initial discovery of extra solar X-ray sources by Giacconi in 1962 and subsequently the first X-ray burst, which was discovered by Grindlay et al. (1976) while analyzing ANS data of the 3U 1820-30 system⁴, they have been tracked and are being tracked by a large number of satellites such as Vela(1969), Uhuru(1970), ANS(1974), SAS-3(1975), EXOSAT(1983), ROSAT(1990), RXTE(1995), Chandra(1999), XMM(1999), and Integral(2002) (and yet more planned) with each mission emphasizing a different aspect of the sources. This has resulted in an enormous amount of observational data much of which is not quantitatively explained by the theoretical models, which must therefore progress slowly limited by the sophistication of the models and the increasing amounts of available computing power.

1.5.1 The observational constraints

Bursting LMXBs show a large variation in behavior: Recurrence times vary from minutes to days and some sources may even shut off for months (Lewin (1977)). In addition most sources show a variation in the behavior of their bursts and may demonstrate both fast rise times ($< 1-2$ s) and long rise times and corresponding short and long decay times respectively, which are anti-correlated with the persistent flux (see e.g. Gottwald et al. (1986) for

⁴While astrophysicists usually and jokingly refer to these names as “license plate”-numbers or “phone”-numbers, observers equivocally use them to tell catalogue and galactic position e.g. 3U 1820-30 is the source listed in the 3rd Uhuru catalogue with a right ascension of 18 hours and 20 minutes and a declination of -30 degrees.

EXO 0748-676 and also Murakami et al. (1980)). In fact only one source, GS 1826-238 (see Kong et al. (2000)), shows nearly identical bursts, because of its very stable accretion flow (Galloway et al. (2004)). This source is also known as “the clocked burster” (Ubertini et al. (1999)) or “the text-book burster” (Bildsten (2000)), since it is the only source, which fits the thermonuclear flash model so well (Cumming (2003)).

Such affective names indicate that a quantitative theoretical description of the detailed observations is not trivial. The thermonuclear flash model which was described in sections 1.2 and 1.3 must account for a variety of observational facts: First and foremost is the α -ratio, defined by the ratio of the persistent fluence, E_p , to the burst fluence, E_b ,

$$\alpha \equiv \frac{E_p}{E_b} = \frac{\int_t^{t+\Delta t} F_p dt}{\int_t^{t+\Delta t} F_b dt} \approx \frac{GM/R}{Q_{nuc}}, \quad (1.6)$$

where Δt is the recurrence time between subsequent bursts, F_b is the burst flux, F_p is the persistent flux, and the last term relates the observations to the interpretations of the flash model. Using the values of section 1.1 suggests that $\alpha \sim 20$ –110, which has been observationally confirmed. Quiescent burning (see sections 3.1.1 and 1.2.1) may inflate α to arbitrarily high values (Lewin et al. (1987); van Paradijs et al. (1988); Gottwald et al. (1989)) whereas unburned fuel of the preceding burst in the upper atmosphere may push the α -ratio to lower values (Fujimoto et al. (1987b)).

Many sources show that α is anti-correlated with the burst duration, which is defined as $\tau = E_b/\max(F_b)$, and correlated with $\gamma = F_p/\max(F_b)$, which is the ratio of the persistent flux to the peak burst flux, (van Paradijs et al. (1988)) as long as that relation does not saturate, which happens for large peak fluxes, when the Eddington limit is reached resulting in photospheric radius expansions (see e.g. Paczyński (1983a)). In addition Gottwald et al. (1986) showed that for EXO 0748-676 the burst fluence is correlated with the recurrence time. However, for several sources, e.g. 4U 1705-44 (Langmeier et al. (1987); Gottwald et al. (1989)), the recurrence time seems to be correlated with the persistent luminosity (accretion rate) which defies the thermonuclear flash model. As a response Bildsten (2000) speculated that this “inconsistency” is caused by a change in the accretion flow at the interface between the disk and the surface.

The analysis of the data, which gives black body temperature, bolometric flux, black body radius, but also fast-timing and spectroscopic information, is complicated by the possibility of false assumptions about the burst/disk interplay (van Paradijs et al. (1988); Walker & Mészáros (1989)), anisotropic flux (Sztajno et al. (1987)), radiation falling outside the satellite detector

bands due to accretion disk absorption and re-emission (Lapidus & Sunyaev (1985)), or photospheric Comptonization which distorts the black body spectrum (London et al. (1984); Nakamura et al. (1989)) — comparing theory to “experiments” is not a trivial matter in this field.

1.6 Goals of this work

It will be the challenge of future theoretical models to explain the increasing levels of details revealed by the observers. This will likely include multidimensional models to study the observed QPOs and include the disk interface and the required radiation transport and wind-equations to describe the matter flow in the relatively thin layers in the upper atmosphere.

The ultimate goal of this work is to acquire an understanding of the nuclear reaction flow of the burst, which is as realistic as possible. This requires a model of the burning environment’s response to the nuclear energy release. Several such models have been used before and they are described in chapter 2 along with our newly developed computer code (details in appendix A).

The behavior of X-ray burst sources mainly depend on their accretion rate. Therefore we model two different sources⁵, which only differ by their accretion rate: A mixed hydrogen/helium ignited flash and a pure helium ignited flash, which are described in chapter 3 and chapter 4 respectively. In chapter 3 we show how the burst behavior depends on the composition profile at ignition using a simple semianalytic calculation. We also describe the detailed reaction flow in a time-dependent matter as a function of depth. The burst ashes are considered due to their importance in validating the current theory of superbursts that occur from sources with this accretion rate. In chapter 4 we demonstrate how an interplay between convection and reaction flow waiting points creates bursts characterized by two separate peaks in the bolometric luminosity. We also consider the importance of convection and how it may transport waiting point isotopes to the surface where they may be observed. Finally we make a small start on a future project of understanding the flow as a function of individual reaction rates.

⁵There are basically four different behaviors: unstable hydrogen burning, which require an advanced treatment of convective diffusion; stable hydrogen burning followed by unstable helium burning in a base layer; stable hydrogen burning followed by unstable burning of mixed hydrogen and helium; and stable burning, which can be treated in a static model (Schatz et al. (1999))

Chapter 2

Modeling the X-ray burst

The burning of the accreted material depends on the density, temperature, and composition of the envelope at the time of ignition. The composition is determined by the time the matter has spent in the envelope which is related to the accretion rate. The temperature and density is related to the pressure which is related to the mass and radius of the neutron star. It is shown that the thermonuclear flash model roughly divides accreting neutron stars into four types of burning according to their mass, radius and accretion rate parameters. A simple model can be devised to calculate the composition and determine the instability.

2.1 Numerical models of the reaction flow

The nuclear burning of the bursting region is determined by the temperature, the density, and the composition of the matter, which are thermodynamically intensive (local) variables. Yet these variables depend on interactions with nonlocal regions, and thus a calculation of the reaction flow must include a model describing the temperature, the density, and the composition, whence different models of varying complexity, typically limited by available CPU-time at the time of the study, have been used to investigate the reaction flow. The models can be classified as follows:

Zero dimensional models comprise post-processing and so-called one-zone models. Post-processing means presetting the temperature and density as a function of time typically to constant values, and investigating how the composition changes (see e.g. Wallace & Woosley (1981); Champagne & Wiescher (1992); van Wormer et al. (1994); Herndl et al. (1995); Schatz et al. (1998)). The one-zone models add a layer of complexity by considering the heat transport in and out of the zone (Paczyński (1983b); Hanawa &

Sugimoto (1983); Koike et al. (1999)) and may even include lateral heat transport (Nozakura et al. (1984)). Aside from uncertainties in the nuclear reaction flow, such models have typically been used to investigate the effects of nuclear uncertainties (Brown et al. (2002)), details of the nucleosynthesis such as the definite end-point (Schatz et al. (2001a,b)) or the response of the ashes (Schatz et al. (2003)). The primary strength of the 0D models is their speed allowing a fast computation of many different reaction rates that even allows Monte-Carlo studies of the reaction rate uncertainties (see e.g. Hix et al. (2003)).

One dimensional models typically assume spherical symmetry and divides the radial component into several discrete zones. One dimensional models are typically based on adopted stellar numerical codes and treat ignition self-consistently by incorporating thermal inertia (Taam (1980)) as well as compositional inertia (Taam (1993)).

In addition, they naturally include a consideration of the flash-type as a function of the accretion rate (Taam (1981, 1982)) and produce realistic luminosity curves which was a major factor contributing to the acceptance of the thermonuclear flash model (Joss (1978); Joss & Li (1980); Taam & Picklum (1979); Taam (1980); Ayasli & Joss (1982); Wallace et al. (1982)). They have even been used to explain individual bursts (Fushiki et al. (1992); Cumming (2003); Fisker et al. (2004)). One dimensional models typically include more realistic boundary conditions and heat transport by conduction and radiation, which can be handled by diffusion laws (Fourier's law and Fick's law respectively), since the mean free path of the bursting region is short ($l \sim 10^{-1}$ cm) compared to the scale of the bursting region ($L \sim 10^2$ cm). Turbulent convection, which is a three-dimensional phenomenon, transports heat and mixes the composition between layers very effectively, whence it is a crucial ingredient in determining the dynamical evolution of temperature and composition in the various layers. Since convective turnover is excluded in one dimension, one-dimensional implementations (Rembges (1999); Woosley et al. (2004) and this work) rely on mixing length theory (MLT), which is a phenomenological model depending on an a priori value of the mixing length, Λ (see discussion in appendix A.5). Until recently the computational demands of including a detailed reaction network were prohibitive and burst calculations were carried out with approximate or reduced networks. Meanwhile CPU power has now reached a level, where a full reaction network can be included in burst calculations (Rembges (1999); Woosley et al. (2004)).

Two dimensional models are based on an Eulerian grid, and because of the large amount of zones they are evolved explicitly. This requires small timesteps severely reducing the size of the nuclear network and restricting the total simulation time to seconds. While this excludes self-consistent ignition, a two dimensional model in the (x, z) -space has been used to study more realistic models of convection (Zingale et al. (2001)). Another model in the (θ, ϕ) -space has been used to study the spreading of the burning front on the neutron star (Spitkovsky et al. (2002)). Naturally two-dimensional models would be the next to include realistic reaction networks.

Three dimensional models are also explicit so including the self-consistent accretion process or realistic networks would either take a very long time or require faster computers than what is available in the near future. To compare with the calculations in this work a typical burst on an AMD Athlon 2000+ machine takes 4-7 days using a 298 isotope network in 103 zones. Most of the CPU time goes into solving the nuclear reaction network, whence a three-dimensional calculation with a similar resolution would require a factor 10^5 more computer time. Such a calculation would require more than a thousand years to complete not allowing for the fact that smaller timesteps would be required extending this timeframe even further (also see appendix A.1).

2.1.1 A new 1D multi-zone burst model

The computational model that is used and has been built as part of this study is described in detail in appendix A. It couples a triad comprising a nuclear reaction network, a hydrodynamical model, and a convective model to treat the complex interplay between the nuclear burning, the hydrodynamical response, and the convective mixing of the composition between the different layers (A.1). The hydrodynamical part (A.2) is based on the code of Liebendörfer et al. (2002), which solves the general relativistic spherically symmetric model in a conservative formulation allowing a very accurate tracking of the energy and therefore a precise determination of the temperature, which is crucial to determine the reaction flow realistically. The code has been rediscritized (A.2.1) to allow an arbitrarily large span in zone masses as long as two adjacent zones do not differ by more than $\sim 20\%$ in mass. While this work does not exploit this capability, the groundwork has been laid to use this model for future self-consistent simulations of superbursts. The inner boundary, i.e. towards the neutron star crust, has been improved compared to previous work which used either a massive substrate (Woosley et al. (2004)) or parameter values (Rembges (1999)). This work

uses the neutron star core code of Brown (2000, 2003) that calculates the thermal luminosity emanating from the crust given the temperature at the atmosphere-ocean interface (A.3.3). The outer boundary, i.e. towards the photosphere, is described by a *grey* atmosphere. This does not include radiation transport beyond the diffusion approximation and does not consider Comptonization effects either. Compared to the above-mentioned previous works the present version is slightly more sophisticated (A.3.2). This implementation sacrifices an accurate photospheric temperature for an accurate energy transport so the nuclear energy that is released during the burst shows up accurately in the calculated luminosity curve. Heat transport is carried out by a diffusion approximation using conductances and opacities which are also functions of temperature, density, and composition (A.4). Different types of convection (A.5) occur when thermal fluctuations cause instabilities to grow. Their rate of growth determine the eddy-velocity, whence all instabilities can be treated by the MLT implementation. The present work only includes the Schwarzschild-Ledoux instability (others are prepared), because it is the dominant form of convection during the burst, whereas secular instabilities (e.g. semi-convection) occur in between bursts and are negligible at high accretion rates, because the diffusion speed is smaller than the advection speed of the accretion. The equation of state is based of K. Nomoto's code and describes the fully ionized atoms of the atmosphere (A.6). The code includes pair, photo, and plasmon neutrino emission (A.7). This effect is only a few percent, but still bigger than the hydrodynamical uncertainty. The nuclear reaction network (A.8) is based on the code of Hix & Thielemann (1999) which scales to an arbitrary size. It computes the nuclear transmutations and their respective energy releases in binding energy and neutrino energy.

2.2 Computational outlay and details

As was pointed out in the introduction (1.5.1), there are bursts, which differ from each other qualitatively in the sense that different bursts can have fast rise times ($< 1-2$ s) and long rise times and corresponding short and long decay times respectively (Ergma & Tutukov (1980); Murakami et al. (1980)). This bursting behavior has long been understood to depend on essentially three parameters: the mass and radius of the neutron star, and the accretion rate (Fujimoto et al. (1981); Hanawa & Fujimoto (1982); Fushiki & Lamb (1987)). Therefore this work investigates the reaction flow on bursters, which have a fixed accretion rate of $\dot{M} = 1 \cdot 10^{17} \text{ g s}^{-1}$ and $\dot{M} = 5 \cdot 10^{16} \text{ g s}^{-1}$ corresponding to cases (1) and (2) of Fujimoto et al. (1981) respectively.

Hanawa & Fujimoto (1982) showed that it is the strength of the gravitational field at the surface rather than the mass and radius, which really determines the burst characteristics. In this work mass and radius are fixed to $M_\infty = 1.4 M_\odot$ and $R_\infty = 10 \text{ km}$. As such this work does not attempt a global study of the burst behavior as a function of the (\dot{M}, M, R) parameter-space, rather it is just two points or at best a cut through the surfaces of Fushiki & Lamb (1987) (also see Lewin et al. (1995); Lamb (2000)).

The rest of this chapter describes the setup ($t = 0$ boundary condition) of the code (2.2.1); the preburst conditions, which are calculated by our model in sec. 3.1 and compared to analytic results. Chapter 3 contains a description of the reaction flow of the mixed hydrogen/helium flash and an investigation of the most important uncertainties of the nuclear reaction rates. Chapter 4 deals with the detailed interactions of the burning regions, which cause bolometrically double peaked bursts.

2.2.1 Setup

As long as the accretion rate is not too low (Brown et al. (1998)), thermal inertia (Taam (1980); Fujimoto et al. (1984); Fushiki et al. (1992)) as well as compositional inertia (Taam (1993); Taam et al. (1996)) plays a crucial role in establishing the burning region's temperature profile, which depends on an interplay between nuclear burning and neutrino radiation loss, and radiative and conductive heat transported towards the surface and core of the neutron star respectively. Therefore many burst cycles are necessary to self-consistently determine the composition of the ashes (Miralda-Escudé et al. (1990)), because the composition of the ashes needs to be made ab initio to self-consistently determine the outflux of the crust of the limit cycle equilibrium¹. Fujimoto et al. (1987b) observed that the behavior of the burst is very dependent on the [relative] abundance of the HCNO elements. As in Rembges et al. (1997) this study only considers solar abundances (Anders & Grevesse (1989)), since most X-ray bursting neutron stars accrete from an unevolved star (Bildsten (1998b)).

The local rest mass accretion rate is fixed to constant values: $\dot{M} = 1 \cdot 10^{17} \text{ g s}^{-1}$ (chapter 3) and $\dot{M} = 5 \cdot 10^{16} \text{ g s}^{-1}$ (chapter 4). Rather than accreting onto an artificial iron-atmosphere for each run, the $t = 0$ model

¹In principle the limit cycle is never reached due to the steady increase of mass due to accretion; but we ignore this fact, as the entire mass of the model is replaced in about $\sim 6 \times 10^5 \text{ s}$ at an accretion rate of 10^{17} g s^{-1} and the mass of the entire neutron star is eleven orders of magnitude larger. Therefore the gravitational field does not change substantially in the time it takes to reach the limit cycle equilibrium for a given mass and radius of the neutron star

was made by following the base model until a limit cycle equilibrium was reached. Subsequently the composition of the burst ashes was copied to the bottom of the model-envelope after which the limit cycle equilibrium was reached as the model adjusted boundary conditions to the new temperature profile resulting from the changed thermal conductivity in the copied shells. This creates a model, which is physically independent of the starting conditions and which is self-consistent with the chosen reaction library, while at the same time avoiding the need to compute the evolution long enough to replace the entire model envelope (true self-consistency). This model will be referred to as the *base model*. The reaction library of the base model is given by Schatz (2003).

2.3 Model analysis

Though the governing equations provide a complete prescription for the next time step their non-linearity makes it impossible to separate cause and effect, whence one is confined to consider contributing factors only. The difficulties this causes in analysing the reaction flow in the XRB-model are also demonstrated in fig. 2.1 which shows a graph of the important events as they are described by the governing equations. The time-axis describes the different burning phases of the accreting neutron stars as it passes through the quiescent phase, followed by the ignition, reaching peak temperature and the cooling phase. The radius-axis describes the burning in the different onion-layered shells of our model: The surface regions, where the density is relatively low, the region around the ignition point, and the regions below it. The last axis describes the nuclear reaction flow as it passes through increasingly heavier isotopes during the explosive burning.

From the figure it then becomes clear that e.g. a faster reaction rate in the (α, p) -process at ignition (ignition region, ignition time, (α, p)) would contribute to a faster increase in temperature in this region thus creating a steeper temperature gradient causing a greater heat flux to the adjacent regions in turn causing a different reaction flow in the breakout reactions of the surface region, while the ignition region was peaking e.g. (surface, peak temperature, breakout). Therefore it is impossible to analyse one region separately in terms of the effects of individual reaction rates – the entire model must be considered as a whole.

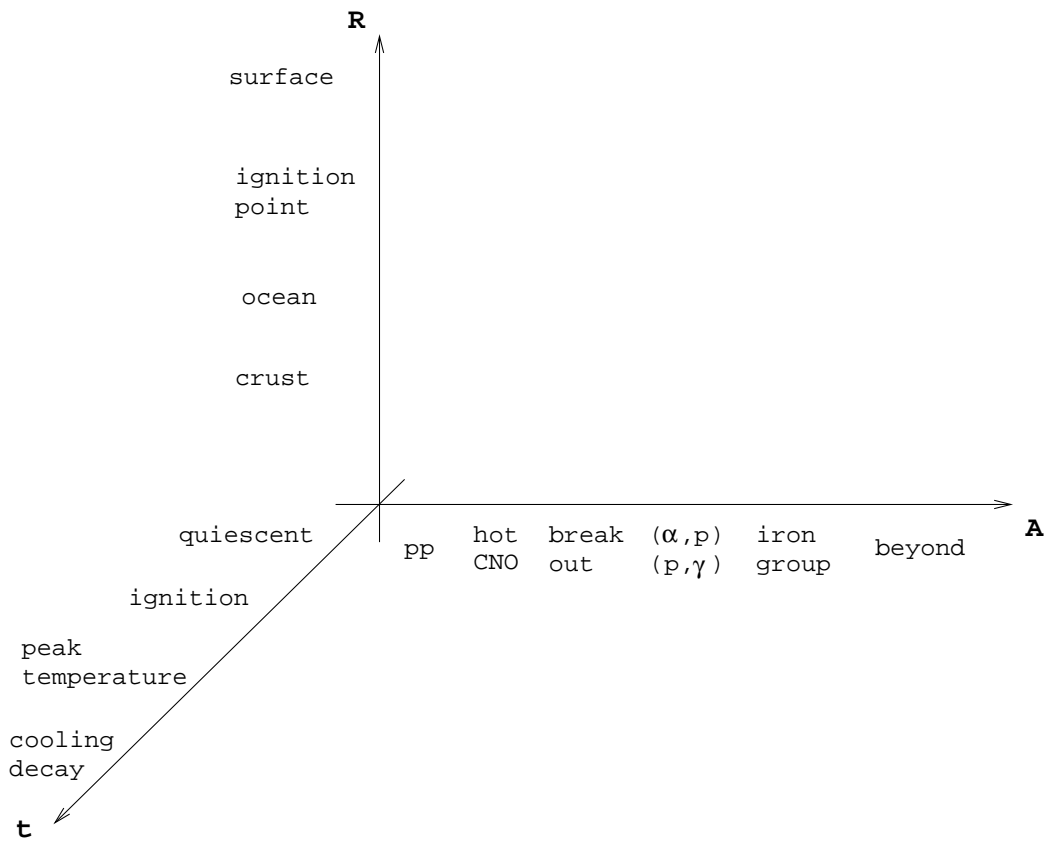


Figure 2.1: The figure illustrates the reaction flow (A) as a function of time (t) and depth/composition (R). A complete description of the reaction flow would be a description of the entire volume spanned by the three axes

2.3.1 Goals of the analysis

Another problem then becomes that of determining how the observables are related to the incompleteness of the model itself and the uncertainty of the model parameters. The observables are currently given by fast timed satellite counters with a spectral resolution sufficiently detailed to pick up individual spectral lines. This means that observables such as bolometric luminosity, detailed spectra including the shape, oscillations, etc. are available. The derived observables such as effective temperature are obscured by the incompleteness of our model, which only consider the burning regions in spherical symmetry and utilizes a phenomenological convection model and a very simple atmospheric model while disregarding the accretion disk interaction. Finally uncertainty in the model parameters may cause misinterpretations of observables. For instance fluctuations in the accretion rate, which seems to be a fluctuating and instantly immeasurable quantity in all but a single burster, GS 1826-238, can change the recurrence time by thousands of seconds (Nozakura et al. (1984)). Other quantities which are not controlled are the mass and radius of the neutron star, which determine the gravitational field and thus the pressure in the burst region (Hanawa & Fujimoto (1982)).

The output of an analysis should therefore be variables which are not compromised by uncertainties. These are e.g.:

- The composition of the surface region as a function of time, which can serve as an input in a solution of radiation transport, which would determine the detailed spectrum of the burst. This has also been suggested by Woosley et al. (2004).
- A strength of our model is its detailed tracking of temperature and density allowing a more accurate calculation of the reaction flow. Only reaction rates in the reaction flow are important to spend resources measuring.
- The ashes of the burning constricts other indirect observables of the neutron star such as e.g. magnetic fields, accretion area, crustal composition, superburst interpretation, gravitational waves, . . . making them useful to a lot of different fields.

Chapter 3

The Mixed H/He ignited flash

We consider and analyze the reaction flow of a typical X-ray burst of a source, where $\dot{M} = 1 \cdot 10^{17}$ g/s, $M_\infty = 1.4M_\odot$, and $R_\infty = 10$ km. It is demonstrated that a mixed H/He burst obtains due to the conditions which are built up during the quiescent phase. The reaction flow of the explosive burning is subsequently analyzed for five interacting depths. The composition of the ashes is given.

3.1 Quiescent burning

Since different layers burn differently depending on their composition, the overall characteristics of the burst can be understood by the composition as a function of depth or the position of the fuel surfaces as described by Fujimoto et al. (1981); Hanawa & Fujimoto (1982); Fushiki & Lamb (1987); Lewin et al. (1995) and Lamb (2000). In Fig. 2.1 these fuel surfaces correspond to a projection of the composition on the (R, A) -plane at a time, t_0 , just prior to the ignition of the burst.

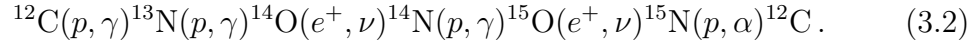
The fuel surfaces are built as the infalling matter settles on the neutron star surface, where it is slowly compressed and pushed into the neutron star atmosphere by the continuously infalling material above it, building up a layered structure. Assuming a constant and spherically symmetric accretion the column depth, $y \equiv \int_{R-r}^R \rho dr$, of a layer as a function of time can be written as

$$y = \frac{\dot{M}}{4\pi R^2} t, \quad (3.1)$$

where \dot{M} is the global mass accretion rate and t is the time that has passed since the clump settled on the surface. At an accretion rate of $\dot{M} = 10^{17}$ g/s it takes about a day for a clump of fuel to reach the ignition point. Since the advection velocity, $dy/dt = \dot{M}/4\pi R^2$, is higher than the diffusion velocity,

the latter can be ignored, whence the isotopes of the different layers do not mix with each other.

At solar temperatures hydrogen burning proceeds via the pp -chains and the CNO-cycle. At higher temperatures the CNO cycle starts to dominate and at even higher temperatures the proton capture on ^{13}N becomes faster than its β^+ -decay and matter is processed via the hot CNO cycle which is given by



When the solar composition matter enters the outermost zone ($T_9 = 0.193$ and $\rho = 1.32 \times 10^5 \text{g/cm}^3$) it is not in equilibrium (see Fig. 3.1) and protons immediately capture on ^{12}C , ^{13}N , and ^{14}N increasing the relative abundance of the β^+ -unstable ^{14}O ($T_{1/2} = 76.4\text{s}$) to the ^{15}O ($T_{1/2} = 122.2\text{s}$). At the same time the $^{15}\text{N}(p, \alpha)^{12}\text{C}$ reaction releases additional ^4He whose abundance increases. The accreted nitrogen and carbon is quickly exhausted enhancing the fraction of ^{14}O , ^{15}O and the hot CNO cycle enters the beta-limited equilibrium cycle (see Fig. 3.1) which has a reaction rate (for hydrogen) given by

$$r_{\text{H}} = \frac{1}{4} \frac{\lambda_{^{15}\text{O}} \lambda_{^{14}\text{O}}}{\lambda_{^{15}\text{O}} + \lambda_{^{14}\text{O}}} X_{\text{hot CNO}} \text{ s}^{-1}, \quad (3.3)$$

where $X_{\text{hot CNO}} = X_{^{15}\text{O}} + X_{^{14}\text{O}}$ is the sum of the nucleon fractions and $\lambda = \ln(2)/T_{1/2}$ defines the decay constants. The helium is converted into ^{12}C via the temperature sensitive triple-alpha reaction. Here we use the rate given by Caughlan & Fowler (1988) which is the same rate employed in our numerical calculation. As ^{12}C quickly captures two protons to become ^{14}O the triple-alpha process enhances the the reaction rate of the hot CNO cycle. Similarly the (p, α) process in the hot CNO-cycle feeds the triple-alpha process. At low temperatures near the surface of the neutron stars one may ignore charged particle reaction aside from those described above. Therefore the hydrogen and helium nucleon fractions can be described by the following set of coupled equations

$$\frac{dX_{\text{H}}}{dt} = -r_{\text{H}} \quad (3.4)$$

$$\frac{dX_{\text{He}}}{dt} = -4r_{\text{He}} + r_{\text{H}} \quad (3.5)$$

$$\frac{dX_{\text{hot CNO}}}{dt} = 4r_{\text{He}} \quad (3.6)$$

These equations can be solved together with eq. (3.1) and a profile of (ρ, T) , which have been determined using our selfconsistent numerical model, and

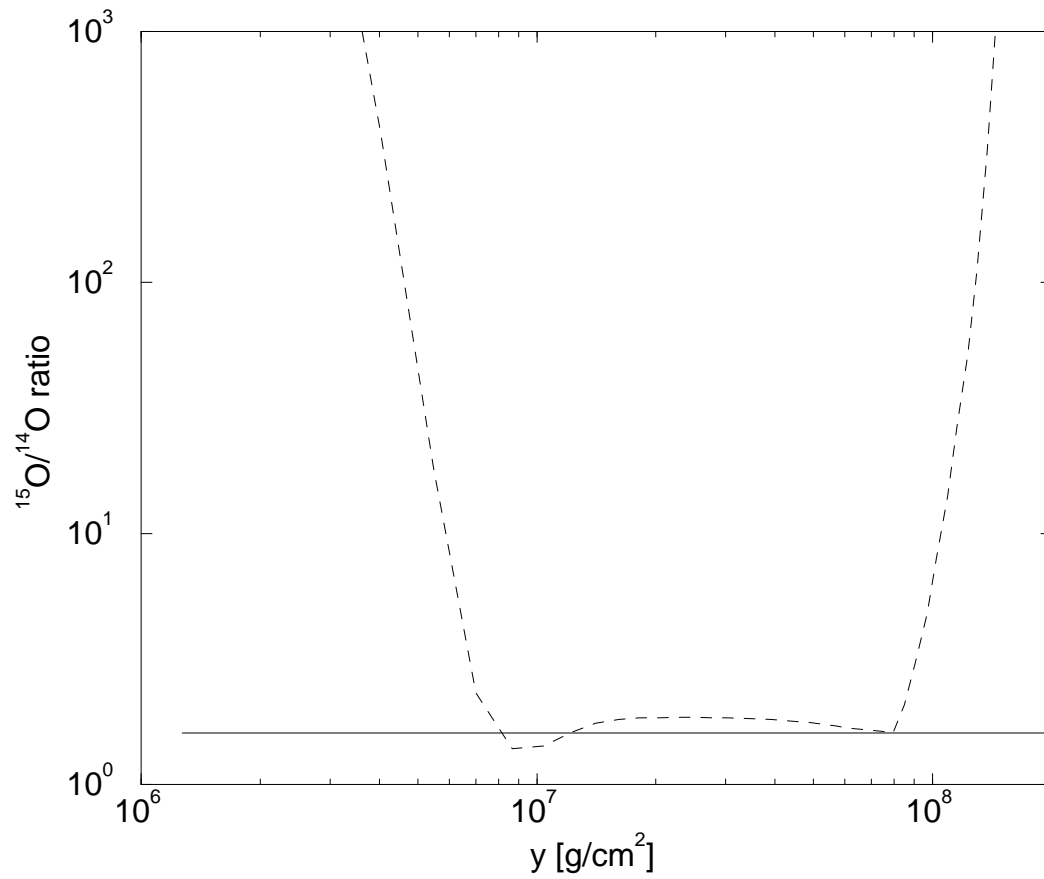


Figure 3.1: The ratio between the weakly decaying waiting point nuclei, ^{14}O ($T_{1/2} = 76.4\text{s}$) and ^{15}O ($T_{1/2} = 122.2\text{s}$), in the hot CNO beta-limited approximation (solid line) compared to our numerical result (dashed line).

using the accreted solar abundances of Anders & Grevesse (1989) as a boundary condition. Our solution for hydrogen and helium is given by the long dashed lines in Fig. 3.2. The steady state profile, calculated using these

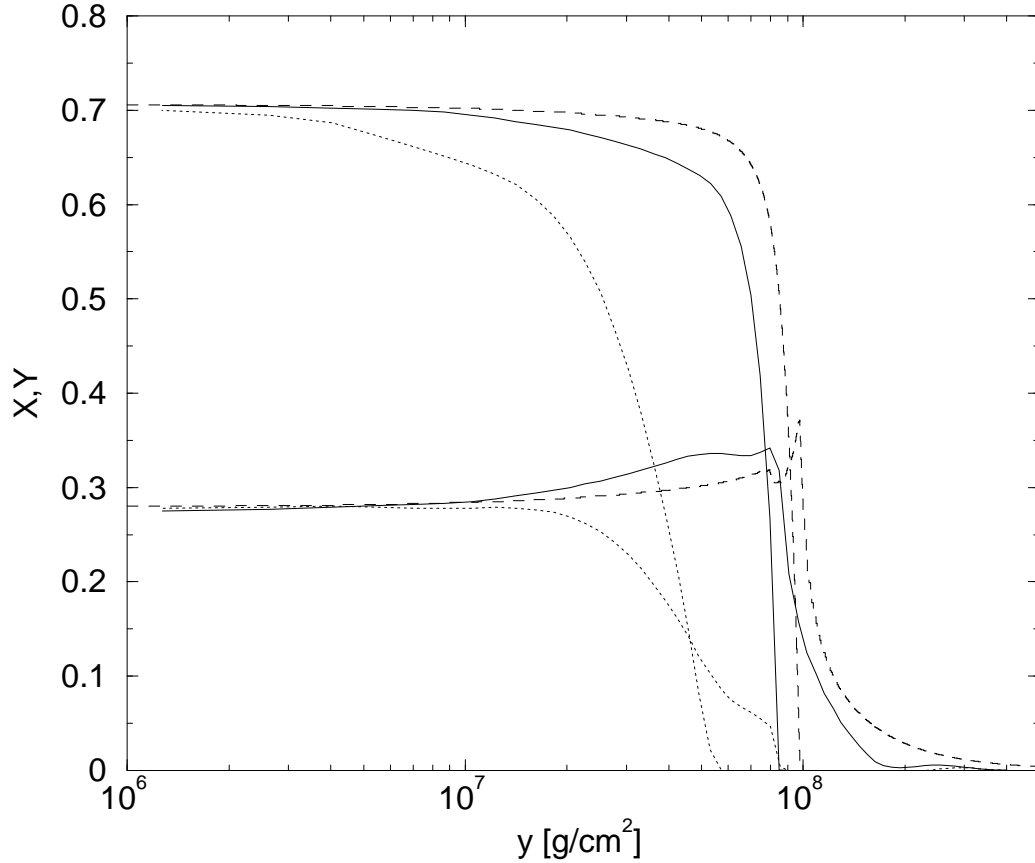


Figure 3.2: The nucleon fractions of hydrogen and helium are shown as a function of column depth prior to the burst (solid lines) where the hydrogen fuel surface lies on top of the ignition surface. The fuel surfaces after the burst are shown with dotted lines. The long dashed lines shows the prediction of the fuel surfaces from our simple estimate (see text).

simple assumptions, determines the upper limit to the amount of hydrogen that can be accreted since no other hydrogen consuming reactions are accounted for. In both the steady state approximation and the numerical model the fastest hydrogen-consuming reaction during the dormant stage is the hot CNO-cycle, the rate of which depends on the abundance of the “hot CNO” nuclei (Hanawa & Sugimoto (1983)). These are determined by the experimentally poorly known triple-alpha process. It can be shown that in-

creasing this reaction rate by a factor of five decreases the critical amount of hydrogen by 15% in the steady-state approximation. The steady state approximation can be compared to the self-consistent dynamical solution at the point just prior to ignition where the maximum (critical) amount of hydrogen and helium has been accreted. The dynamical solution is shown in Fig. 3.2 by the solid lines. The agreement is reasonable, but we note that hydrogen is exhausted earlier in the selfconsistent model. Fig. 3.2 shows that in the dynamical model the helium fraction increases at the same rate as the hydrogen fraction decreases, whence the discrepancy is explained by the beta-limited approximation up to a column depth of $\sim 4 \times 10^7 \text{g/cm}^2$, which is shown in Fig. 3.1. Beyond this point hydrogen is exhausted at a faster rate than helium: This is due to proton captures on other isotopes which becomes competitive with the hot CNO-cycle.

3.1.1 Quiescent rp -process

A few thousand seconds prior to the burst first significant hydrogen consuming reactions below $y \sim 4 \times 10^7 \text{g/cm}^2$ appear after the $^{15}\text{O}(\alpha, \gamma)^{19}\text{Ne}$ branch becomes competitive with the β^+ -branch regulating the hot CNO-cycle rate, thus providing a feed to heavier isotopes - knowing the low temperature characteristics of this rate is therefore important to determine the formation rate of seed nuclei for the quiescent rp -process. In this temperature range ($T_9 \sim 0.27$), the triple-alpha process is feeding the hot CNO-cycle via the carbon, thus the activity of the ^{15}O -decay actually increases thus increasing the hydrogen consumption. The reaction flow proceeds through the so-called NeNaMg-cycle, however, the $^{22}\text{Na}(p, \alpha)^{19}\text{Ne}$ is very slow compared to the proton capture on ^{22}Na , therefore no helium is produced via the ineffective cycle putting a damper on the original breakout of the hot CNO-cycle. Hydrogen is then slowly (compared to the hot CNO cycle) burned until the double magic ^{40}Ca is reached which at this temperature puts a strong damper on the continued reaction flow. Here the $^{43}\text{Sc}(p, \alpha)^{40}\text{Ca}$ contributes about 1% of the helium compared to the hot CNO cycle.

In total this “dormant” or quiescent rp -process is responsible for 10–20% of the hydrogen-consumption for a period of thousands of seconds at an accretion rate of $\dot{M} = 10^{17} \text{g/s}$. The effect is that the helium/hydrogen ratio is raised leading to a smaller accumulation of hydrogen before the helium reaches a critical depth and thus a weaker burst obtains compared to a simpler model that excludes this process. Furthermore the composition is changed towards better bound nuclei, which also impedes the impending explosive runaway.

Note! Because of the interaction of the quiescent *rp*-process the hydrogen and helium fuel surfaces defined and discussed in Fushiki & Lamb (1987) do not lie superposed (even at our high accretion rate) and as a result the bursting splits into three scenarios, which can be described separately, namely: Helium-burning in a hydrogen poor background of ashes; Mixed hydrogen/helium burning (with an enhanced ratio of H/He compared to the accreted material) (the trigger happens at the bottom of this region) – this is the burning region which produces the heaviest ashes. Finally there is mixed hydrogen helium burning in the atmosphere, which does not result in a runaway due to the lower density.

3.2 Explosive burning

Runaways occurring in a mixed H/He layer mainly proceed via the *rp*-process (Wallace & Woosley (1981)), where the characteristic timescale, $\tau_{rp} \sim \sum T_{1/2}$, is given by the sum of the half-lives of the β -decays in the reaction flow (van Wormer et al. (1994)). However, depending on the flow pattern a simultaneously occurring (α, p)-process, which does not depend on β -decays, may decrease the timescale through the *sd*-shell nuclei (Wallace & Woosley (1981); Schatz et al. (1998)). As the runaway lasts several seconds in this case, the temperature gradient only produces a minor convective instability.

Since the different layers interact and also burn differently due to different compositions and temperature, the burst can not be understood based on the burning of one layer only, but must be analyzed for several different burning layers, since they all contribute to the observables mentioned in sec. 2.3.1. Therefore the analysis is split into four regions: the region around the ignition point, the convective region, the surface, and the ocean, which are sufficiently different to merit separate attention. This would correspond to making (four) cuts parallel to the (A, t)-plane (See Fig. 2.1) for $R = \text{ocean}$, $R = \text{ignition region}$, $R = \text{convective region}$, and $R = \text{surface}$ respectively. These cuts are shown in Fig. 3.3, which shows a trace of the burst conditions for different depths (pressures) during a complete revolution of the limit cycle. Following the cooling of the previous burst, the individual layer reach their lowest temperature and highest density of the cycle. The subsequent accretion, which was described in sec. 3.1, increases the hydrogen content of the layer, which in turn lowers the density, because the increased electron abundance of hydrogen requires less mass to maintain the hydrostatic pressure (Joss (1977); Joss & Li (1980)) compared to the heavier and more neutron-rich ashes (Hanawa & Fujimoto (1984)). This is most clearly seen in

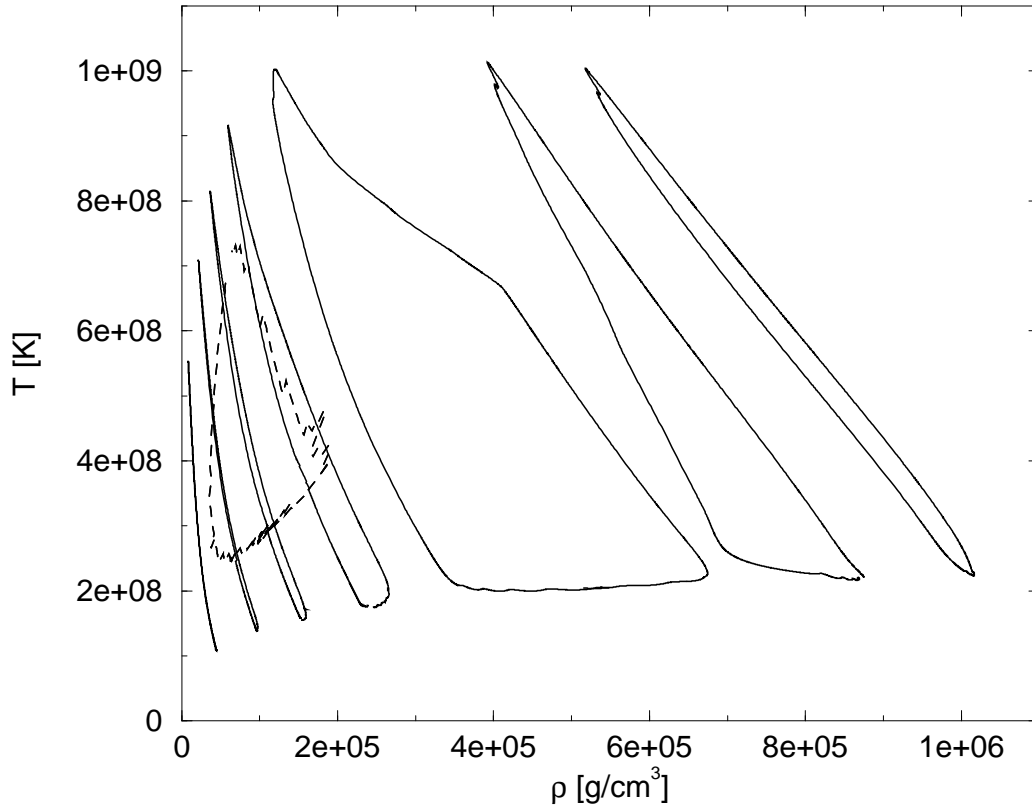


Figure 3.3: From left to right (solid line): $y = 2.1 \times 10^6 \text{g/cm}^2$ (surface), $y = 9.5 \times 10^6 \text{g/cm}^2$ (top of the convective region), $y = 1.9 \times 10^7 \text{g/cm}^2$, $y = 3.3 \times 10^7 \text{g/cm}^2$ (bottom of the convective region), $y = 6.2 \times 10^7 \text{g/cm}^2$ (above ignition), $y = 8.3 \times 10^7 \text{g/cm}^2$ (ignition point), and $y = 1.1 \times 10^8 \text{g/cm}^2$ (ocean). The dashed line indicate the region which is convective during the rising of the burst.

Fig. 3.3 just above the ignition region, which decreases its density by about a factor two during the quiescent phase, as the electron-rich surface ashes of the previous burst sink into this region. For an accretion rate of $\dot{M} = 1 \cdot 10^{17} \text{ g s}^{-1}$ and a recurrence time of $\Delta t \approx 11000 \text{ s}$ (see sec. 1.5), the neutron star accretes a mass of $\Delta M = \dot{M} \cdot \Delta t \approx 1.1 \cdot 10^{21} \text{ g}$ ($5.5 \cdot 10^{-13} M_{\odot}$) in between bursts. This means that matter above a column density of $y = 5.8 \times 10^7 \text{ g cm}^{-2}$ is freshly accreted, whereas matter below comprise the old surface ashes of the previous burst(s), whence the composition in the ignition region actually consist of heavier ashes with a comparably lower hydrogen/helium abundance. When eq. [1.2] is finally violated, the matter ignites and the nuclear runaway causes a rising temperature, which eventually affects the degeneracy of the electrons and decreases the density further as the trace runs up the left leg of the cycle in Fig. 3.3, until the fuel is exhausted as it burns into heavier ashes shortly after the peak temperature is reached. The β^+ -decays during and subsequent to the rp -process decrease the electron abundance and brings the trace down the right leg as the envelope cools. Therefore the separation in density between the rising leg and the decaying leg accounts for the change in composition, whence the largest change happens around the ignition regions, whereas the surface does not change its composition much – this can also be seen in Fig. 3.2, which shows the hydrogen and helium mass fractions as a function of depth before and after the burst respectively.

The different compositions and hydrostatic pressures with corresponding temperatures and densities of the burning regions change dynamically on a nuclear timescale¹. Therefore the analysis of the nuclear reaction flow proceeds in a different way compared to previous works, which assumed solar abundances burning at fixed densities and temperatures and described the integrated flow over many minutes (van Wormer et al. (1994); Rembges et al. (1997)); instead the instant flow rate is described as the thermodynamic state variables change.

The net reaction flow rate from isotope i to isotope j is defined by

$$f_{ij} = -f_{ji} = \dot{Y}_{i \rightarrow j} - \dot{Y}_{j \rightarrow i}, \quad (3.7)$$

where $\dot{Y}_{i \rightarrow j}$ is the time rate-of-change of the i th isotope resulting from all reactions converting isotope i to isotope j . The flow-rates for the different times of Fig. 3.3 will be demonstrated in the flowcharts of the following

¹Due to the hydrostatic approximation the dynamical timescale is essentially irrelevant in describing the envelope, because the gravitational energy is much higher than nuclear energy, which can be converted into the kinetic energy (Joss (1977); Joss & Li (1980) and sec. 1.1). Therefore the pressure at a certain depth stays constant to a very good approximation at all times relating the state variables through $P(y) \approx P(\rho, T, \vec{X})$, where y is the column density.

sections, which describe the reaction flow rates at the ignition point, the region above it, the convective zone, the surface (of our model), and the ashes going into the ocean. In these figures the main reaction-flow is described by the heavy lines with the exception of isotopes, which are in $(p, \gamma)(\gamma, p)$ -equilibrium, because the calculation of the flow-chart are based on an explicit extrapolation of eq. [A.31], whence they give erroneous numerical results, since large rates, which would cancel in reality, do not cancel numerically. The numerical uncertainty in the maximum flow rate makes it impossible to normalize the flow rate to a maximum value. Therefore flow rates are plotted with a thickness set by the logarithm of the flow rate. In this way thin lines indicate a flow rate just above $10^{-6} \text{ mol g}^{-1} \text{ s}^{-1}$ increasing their thickness logarithmically to a maximum after which they stay constant. Very thick lines indicate $(p, \gamma)(\gamma, p)$ -equilibrium.

3.2.1 Ignition point

During the quiescent phase the fuel surface slowly move toward the ignition surface. The fuel surface comprise heavier ashes of the previous burst which are mixed with increasing amounts of about 10% helium (no hydrogen). As the temperature increases traces of the latter begin to capture on light stable daughter nuclei: ^{15}N , ^{18}O , ^{18}F , ^{19}F , and ^{23}Na (see Görres et al. (1989)) which become alpha-unbound. In addition protons capture on ^{34}S and on all $T_z = (N - Z)/2 = -1/2$ isotopes between neon and silicon. These (p, α) -reactions explain the temperature fluctuations of the ignition region, which can be seen in Fig. 3.4) – they are, however, too weak to cause a runaway. Behind the very front of the fuel surface a constantly burning hot CNO cycle turns ^1H into ^4He in the manner described in sec. 3.1. As the triple-alpha process becomes increasingly faster due to the increasing density and temperature, the fraction of ^{14}O ($T_{1/2} = 76.4\text{s}$) increases. The hot CNO cycle in turn increases the ^4He concentration until a runaway of the triple-alpha ensues². This runaway creates ^{12}C which immediately captures two protons to become ^{14}O , causing the $^{14}\text{O}/^{15}\text{O}$ -ratio to increase, since ^{14}O ($T_{1/2} = 76.4\text{s}$) decays too slowly. This is evident from Fig. 3.5 and Fig. 3.1. We now describe the reaction flow in terms of temperature, density, and proton and alpha fractions as the time develops. The time is synchronized, so $t = 0$ coincides with the peak surface luminosity.

²Originally we were concerned about the reaction flow through the heavier ashes, so reactions on light isotopes e.g. the pp -chains and the rap -processes of Wiescher et al. (1989) were neglected. They will be included in future runs, because they are within easy reach of radioactive ion beam experiments (Hass (2003)).

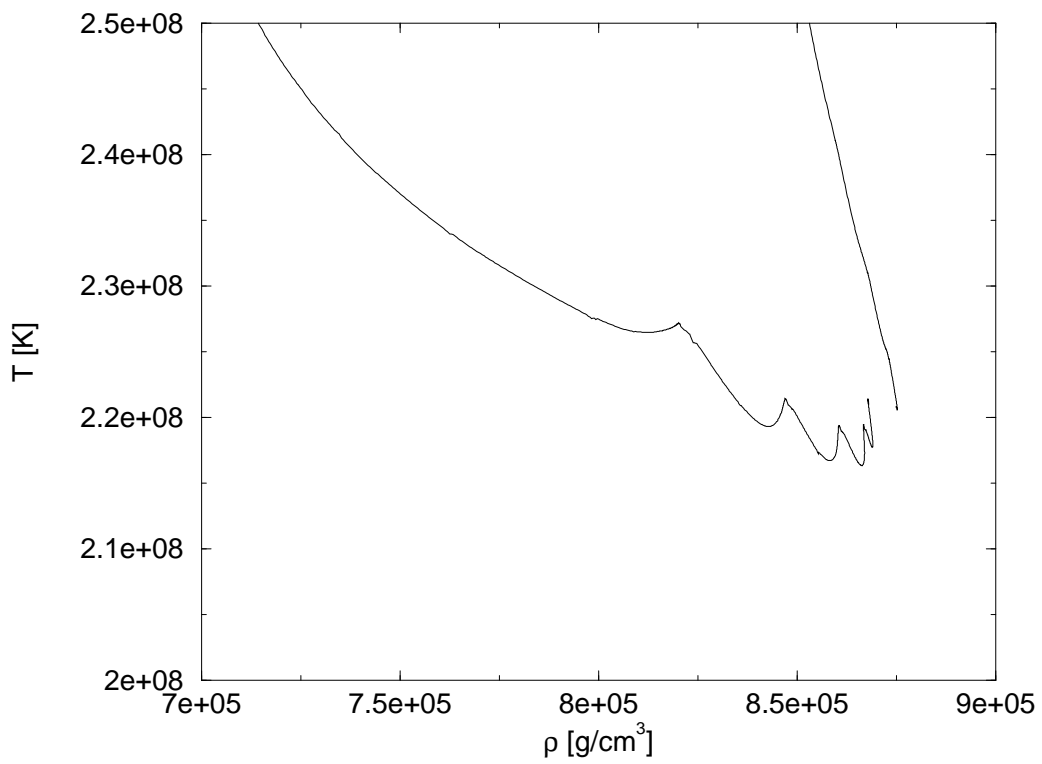


Figure 3.4: A magnified plot of the (ρ, T) -trace at the ignition point of Fig. 3.3.

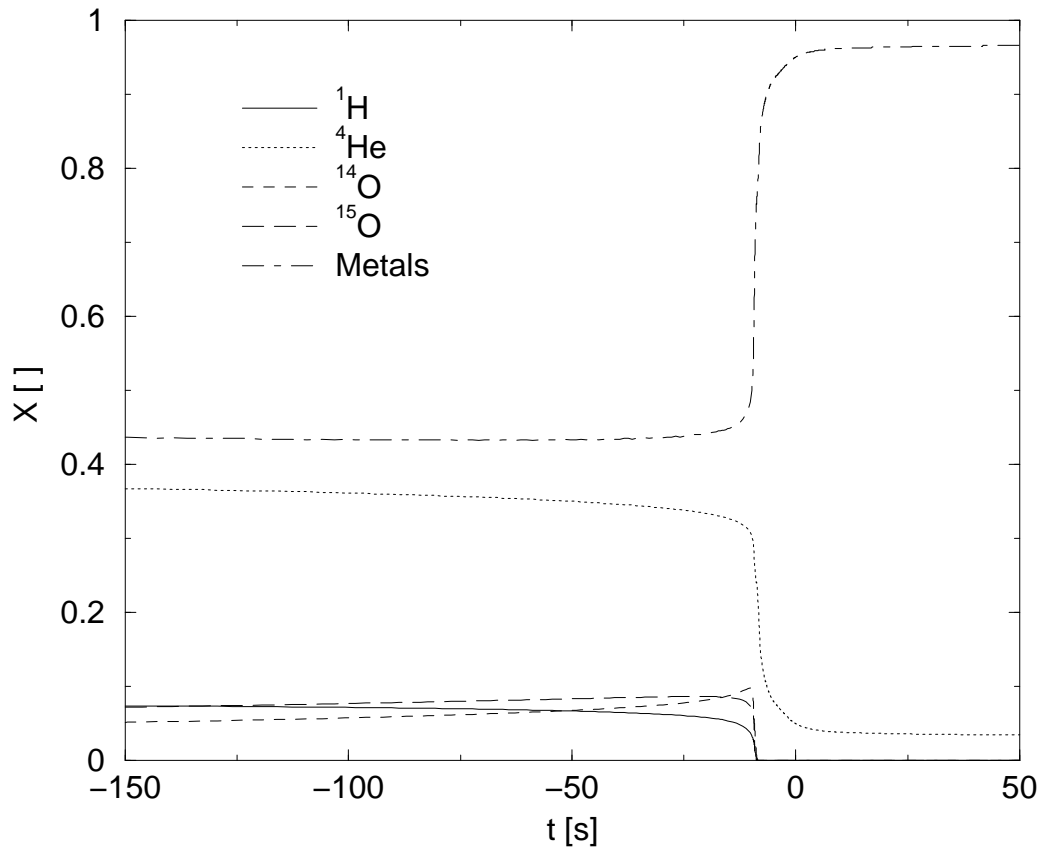


Figure 3.5: The hydrogen, helium, CNO type matter, and metal (the rest) mass fractions as a function of time. The time scale has been synchronized to coincide with the burst luminosity peak at $t = 0$. Note that the hydrogen is complete exhausted during the burst while about $\sim 5\%$ helium remains.

Fig. 3.6: $T = 5.63 \cdot 10^8 \text{ K}$, $\rho = 5.67 \cdot 10^5 \text{ g cm}^{-3}$, $X = 0.020$, $Y = 0.27$, $t = -9.2482540 \text{ s}$

At this time the increasing temperature has caused the flow rate of $^{15}\text{O}(\alpha, \gamma)^{19}\text{Ne}$ to reach 10% of the $^{15}\text{O}(\beta^+)^{15}\text{N}$ rate establishing a break-out of the hot CNO cycle (the 1% limit was breached at $t = -103.6\text{s}$) which eventually reaches ^{40}Ca

Reaching ^{19}Ne the matter can no longer return to the hot CNO cycle and the reaction flow proceeds with $^{19}\text{Ne}(p, \gamma)^{20}\text{Na}(p, \gamma)^{21}\text{Mg}$, where it is blocked by photodisintegration, because of the $^{21}\text{Mg}(p, \gamma)(\gamma, p)^{22}\text{Al}$ -equilibrium. Therefore the flow proceeds via $^{21}\text{Mg}(\beta^+, T_{1/2} = 0.122 \text{ s})^{21}\text{Na}(p, \gamma)^{22}\text{Mg}(\beta^+, T_{1/2} = 3.86 \text{ s})^{22}\text{Na}(p, \gamma)^{23}\text{Mg}(p, \gamma)^{24}\text{Al}(p, \gamma)^{25}\text{Si}$, which is again in blocked by photodisintegration from the $^{25}\text{Si}(p, \gamma)(\gamma, p)^{24}\text{P}$ reaction.

Following the decay by $^{25}\text{Si}(\beta^+, T_{1/2} = 0.634 \text{ s})^{25}\text{Al}(p, \gamma)^{26}\text{Si}$ ($T_{1/2} = 2.23 \text{ s}$), which is too long-lived for its decay to be relevant, thus $^{26}\text{Si}(p, \gamma)^{27}\text{P}(\beta^+, T_{1/2} = 0.260 \text{ s})^{27}\text{Si}(p, \gamma)^{28}\text{P}(p, \gamma)^{29}\text{S}(\beta^+, T_{1/2} = 0.187 \text{ s})^{29}\text{P}(p, \gamma)^{30}\text{S}(\beta^+, T_{1/2} = 1.18 \text{ s})$. ; this is too long, so the next decay occurs from the $^{30}\text{S}(p, \gamma)(\gamma, p)^{31}\text{Cl}(\beta^+, T_{1/2} = 0.200 \text{ s})$, until the temperature becomes sufficiently high to completely photodisintegrate most of the ^{31}Cl eventually leaving a ratio of $Y_{\text{Cl}-31}/Y_{\text{S}-30} \sim 10^{-7}$. Therefore the flow continues along $^{31}\text{S}(p, \gamma)$ (Iliadis et al. (1999)) $^{32}\text{Cl}(\beta^+, T_{1/2} = 0.298 \text{ s})^{32}\text{S}(p, \gamma)^{33}\text{Cl}(p, \gamma)^{34}\text{Ar}(\beta^+, T_{1/2} = 0.844 \text{ s})^{34}\text{Cl}(p, \gamma)^{35}\text{Ar}(p, \gamma)$ (Iliadis et al. (1999)) $^{36}\text{K}(\beta^+, T_{1/2} = 0.342 \text{ s})^{36}\text{Ar}(p, \gamma)^{37}\text{K}(p, \gamma)^{38}\text{Ca}$.

Since ^{39}Sc and ^{40}Sc are almost proton unbound the flow must wait for ^{38}Ca ($T_{1/2} = 0.440 \text{ s}$) and ^{39}Ca ($T_{1/2} = 0.860 \text{ s}$) to β^+ -decay before the flow stops at the well-bound ^{40}Ca isotope. Thus in total the timescale for this sequence is (c.f. van Wormer et al. (1994)) $\tau = \ln(2)^{-1} \sum T_{1/2} \sim 8\text{s}$ which is slower than the time it takes to cover the star with a deflagration wave (c.f. sec. 1.2.1) by a factor four. Therefore a one-dimensional approximation is still reasonable.

However, as the (α, p) -process ignites and the temperature increases, the reaction flow will move closer to the dripline decreasing the β -half-lives which makes the timescales comparable. This means that our model is no longer predictive of hydrodynamically influenced (extensive) observables such as the time-dependent luminosity, however, our model still provides a local (intensive) description of the burning conditions, and therefore a realistic description of the reaction flow.

Fig. 3.7: $T = 7.15 \cdot 10^8 \text{ K}$, $\rho = 5.06 \cdot 10^5 \text{ g cm}^{-3}$, $X \approx 0$, $Y = 0.233$, $t = -8.667018 \text{ s}$

Half a second later the $^{14}\text{O}(\alpha, p)^{17}\text{F}$ breakout reaction reaches 1/3 of the flow rate of the $^{15}\text{O}(\alpha, \gamma)^{19}\text{Ne}$ -reaction. This starts the hot CNO bi-cycle: $^{14}\text{O}(\alpha, p)^{17}\text{F}(p, \gamma)^{18}\text{Ne}(\beta^+)^{18}\text{F}(p, \alpha)^{15}\text{O}$. A meta bi-cycle is created from the decay branch of $^{19}\text{Ne}(\beta^+)^{19}\text{F}(\alpha, \gamma)^{16}\text{O}(p, \gamma)^{17}\text{F}$ thus returning this cycle to the bi-cycle.

At this stage $^{22}\text{Mg}(p, \gamma)^{23}\text{Mg}$ and $^{22}\text{Mg}(\beta^+, T_{1/2} = 3.86 \text{ s})^{22}\text{Na}$ become comparable. Consequently the flow path through $^{23}\text{Mg}(p, \gamma)^{24}\text{Si}(\beta^+, T_{1/2} = 0.102 \text{ s})^{24}\text{Al}$ competes with $^{22}\text{Mg}(\beta^+, T_{1/2} = 3.86 \text{ s})^{22}\text{Na}(p, \gamma)^{23}\text{Mg}(p, \gamma)^{24}\text{Al}$ effectively creating a shortcut. Since the flow rates are about equal, the effective timescale becomes the mass fraction weighted harmonic mean of the two half-lives $\approx 0.14 \text{ s}$, which is much faster than before. This reduces the total timescale to reach ^{40}Ca to $\sim 5 \text{ s}$. A similar shortcut exists between ^{25}Si and ^{27}P , however, here the Q -value is only 141 keV , so the faster path is suppressed by photodisintegration.

Very little ^{31}Cl now exists, so the flow must pass through the $^{30}\text{S}(\beta^+, T_{1/2} = 1.18 \text{ s})$ reaction, which is the slowest weak reaction in the flow and adds about a second to the total timescale.

Other short cuts arise e.g. $^{32}\text{Cl}(p, \gamma)^{33}\text{Ar}(\beta^+, T_{1/2} = 0.173 \text{ s})^{33}\text{Cl}$ against $^{32}\text{Cl}(\beta^+, T_{1/2} = 0.298 \text{ s})^{32}\text{S}(p, \gamma)^{33}\text{Cl}$ or $^{36}\text{K}(p, \gamma)^{37}\text{Ca}(\beta^+, T_{1/2} = 0.175 \text{ s})^{37}\text{K}$ vs. $^{36}\text{K}(\beta^+, T_{1/2} = 0.342 \text{ s})^{36}\text{Ar}(p, \gamma)^{37}\text{K}$. The potential effectiveness of these short cuts in changing the timescale of the flow is given by their half-lives. The weights are given by the (p, γ) -reaction rate on the original isotope i.e. ^{32}Cl and ^{36}K .

The flow breaks into the pf -shell nuclei by proton-captures on ^{39}Ca and ^{40}Ca (Wiescher & Görres (1989)). Very fast β^+ -decays on the highly radioactive Sc and Ti isotopes that obtain causes the flow to spread (fig.3.7) and makes an analysis of the timescales difficult.

A hot CNO like cycle exists on $^{40}\text{Ca}(p, \gamma)^{41}\text{Sc}(p, \gamma)^{42}\text{Ti}(\beta^+, T_{1/2} = 0.199 \text{ s})^{42}\text{Sc}(p, \gamma)^{43}\text{Ti}(\beta^+)^{43}\text{Sc}(p, \alpha)^{40}\text{Ca}$. However, breakout occurs via $^{43}\text{Ti}(p, \gamma)^{44}\text{V}$ and $^{43}\text{Sc}(p, \gamma)^{44}\text{Ti}$ which forms paths eventually passing through ^{45}V ($T_{1/2} = 0.547 \text{ s}$). These isotopes may either do a beta-decay followed by a proton-capture or do a proton-capture followed by a beta-decay and end up in ^{46}V ($T_{1/2} = 0.422 \text{ s}$), which decays to the stable ^{46}Ti . This effectively stops the rp -process for these conditions, and due to the very low hydrogen abundance at this depth, the flow will not break out of the $A = 46$ isotopes. Since this represents a hurdle to the flow it is important to determine the (p, γ) -rates on the V isotopes correctly. Comparing the effects of substituting in the rates of Fisker et al. (2001a), and Fisker et al. (2001b)

has shown that these rates influence the shape of the luminosity curve – preliminary studies have also shown that external observables e.g. Δt , $\max(F_b)$, may be highly dependent on these rates.

Fig. 3.7 also shows some reprocessing of ^{49}Cr and ^{52}Cr , which burns close to the valley of stability and eventually ends up in the nickel-zinc region.

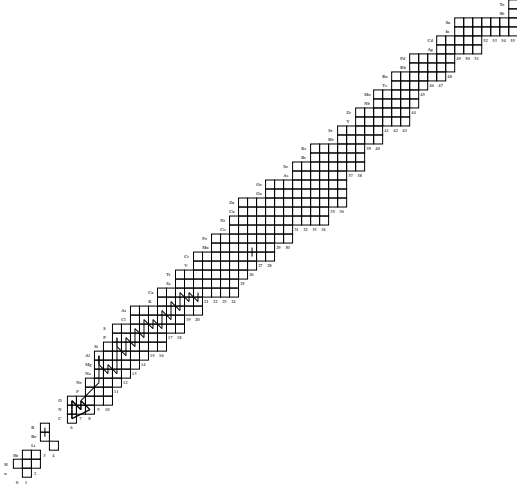


Figure 3.6: Ignition

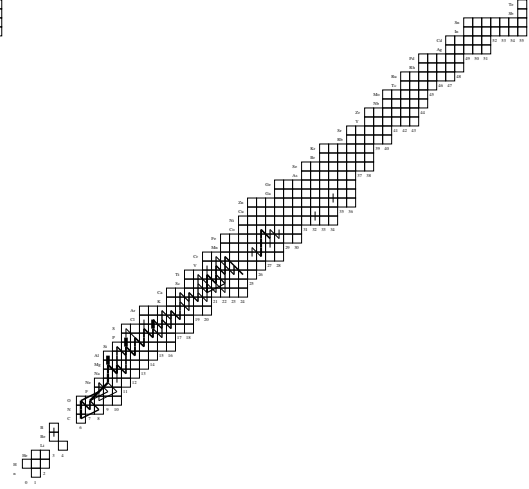


Figure 3.7: Ignition

Fig. 3.8: $T = 9.60 \cdot 10^8 \text{ K}$, $\rho = 4.06 \cdot 10^5 \text{ g cm}^{-3}$, $X \approx 0$, $Y = 0.10$, $t = -6.6445538 \text{ s}$

The protons are exhausted within one second. This can also be seen in Fig. 3.5. Once this happens, the proton-rich isotopes near the driplines decays towards the valey of stability, where they undergo (α, p) -reactions. The released protons capture on the most abundant isotopes with the largest capture cross sections. This is primarily ^{12}C , which is still synthesized by the triple-alpha process, but also stable or relatively long lived isotopes such as ^{21}Ne , ^{21}Na , ^{22}Na , ^{24}Mg , ^{26}Al , and ^{26}Si . Since most protons are absorbed by ^{12}C , the overall effect of these reactions is to move the proton-rich isotopes closer to the alpha-chain ($N = Z$ even-even) isotopes.

Fig. 3.9: $T = 1.01 \cdot 10^9 \text{ K}$, $\rho = 3.97 \cdot 10^5 \text{ g cm}^{-3}$, $X \approx 0$, $Y = 0.05$, $t = -0.23604405 \text{ s}$

The flow through the alpha-chain nuclei is clearly seen in Fig. 3.8 which shows the reaction flow at the time where maximum temperature is achieved. Notice

that $^{12}\text{C}(p, \gamma) ^{13}\text{N}(\alpha, p) ^{16}\text{O}$ is much stronger than the direct $^{12}\text{C}(\alpha, \gamma) ^{16}\text{O}$ -reaction as long as the (α, p) -reactions are still possible on heavier isotopes.

The reaction flow continue with (α, γ) -reactions up to ^{36}Ar . Eventually the downward heat flux from the upper regions becomes too weak to sustain the (α, p) -reactions and the reactions die out leaving only radioactive isotopes that slowly decay to stabler ones.

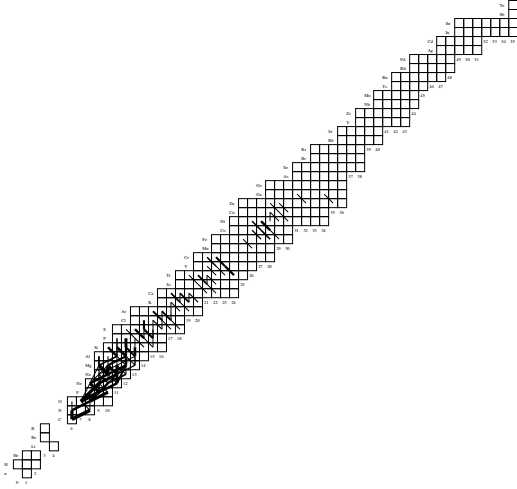


Figure 3.8: Ignition

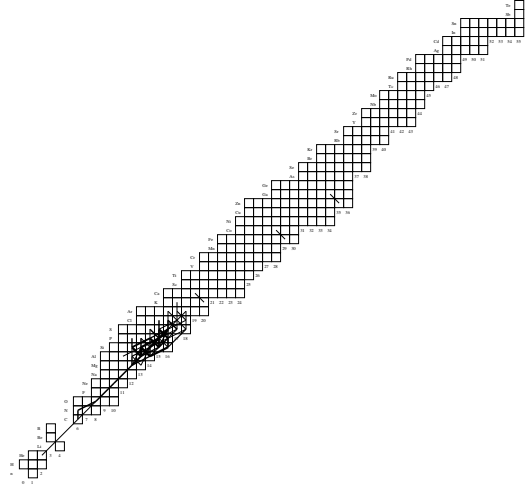


Figure 3.9: Ignition

3.2.2 Above the ignition point

It is relevant to know the reaction flow and its energy release at the depth, which reach the highest temperature during the burst, because it heats up adjacent and colder regions. This is because heat is transported as electrons and photons are diffused along a negative temperature gradient. The highest temperature of a burst ignited by mixed hydrogen and helium is reached just above the point of point of ignition c.f. Fig. 3.4.

Fig. 3.10: $T = 6.18 \cdot 10^8 \text{ K}$, $\rho = 1.84 \cdot 10^5 \text{ g cm}^{-3}$, $X = 0.541$, $Y = 0.360$, $t = -8.6670187 \text{ s}$

The $^{15}\text{O}(\alpha, \gamma)^{19}\text{Ne}$ -reaction is less important at this depth, because less “hot CNO material” has been created due to lower operating temperatures and densities of the triple-alpha process. So while the reaction burns off the existing ^{15}O , the runaway at this depth occurs, when the heat from the ignition point below increases the triple-alpha reaction, so the $^{12}\text{C}(p, \gamma) ^{13}\text{N}(p, \gamma)$

$^{14}\text{O}(\alpha, p)^{17}\text{F}$ reaction path dominates. This is because ^{14}O ($T_{1/2} = 76.4\text{ s}$) does not have the time to decay during the runaway. At this point the $^{15}\text{O}(\alpha, \gamma)^{19}\text{Ne}$ -reaction does establish a very weak flow to ^{30}S along a flow path identical to the initial path in the deeper region. Since this depth contains former surface ashes there is more ^{40}Ca than at the ignition point which contains ashes from the convective region. The ^{40}Ca starts capturing protons, which are also more abundant, establishing a flow to ^{46}Ti .

Fig. 3.11: $T = 6.66 \cdot 10^8\text{ K}$, $\rho = 1.72 \cdot 10^5\text{ g cm}^{-3}$, $X = 0.539$, $Y = 0.358$, $t = -8.47754325\text{ s}$

At this point $^{14}\text{O}(\alpha, p)^{17}\text{F}$ breakout reaction reaches 1/3 of the flow rate of the $^{15}\text{O}(\alpha, \gamma)^{19}\text{Ne}$ -reaction. This happens at a lower temperature for this depth, because the $^{14}\text{O}/^{15}\text{O}$ abundance-ratio is relatively higher.

The breakout establishes the hot CNO bi-cycle; in contrast to the ignition point, the meta bi-cycle is not established, because it is already sufficiently hot and there is sufficient hydrogen to capture on ^{19}Ne destroying it immediately.

The heat flux building up rapidly from the ignition point below means that short cuts e.g. $^{23}\text{Al}(p, \gamma)^{24}\text{Si}(\beta^+, T_{1/2} = 0.102\text{ s})^{24}\text{Al}$ competing with $^{22}\text{Mg}(\beta^+, T_{1/2} = 3.86\text{ s})^{22}\text{Na}(p, \gamma)^{23}\text{Mg}(p, \gamma)^{24}\text{Al}$ and $^{25}\text{Si}(p, \gamma)^{26}\text{P}(p, \gamma)^{27}\text{S}(\beta^+, T_{1/2} = 0.021\text{ s})^{27}\text{P}$ competing with $^{25}\text{Si}(\beta^+, T_{1/2} = 0.220\text{ s})^{25}\text{Al}(p, \gamma)^{26}\text{Si}(p, \gamma)^{27}\text{P}$ quickly becomes dominated by the leg closest to the proton dripline.

A weak flow into the pf -shell now occurs through the ^{39}Ca isotope. However, most of the burning on these isopes is due to proton capture on residual ^{40}Ca from the last burst. This reaction sequence ends in ^{46}Ti as for Fig. 3.7.

In addition previous ashes starts to burn: ^{49}Cr and ^{50}Cr burns into the Ni and Co isotopes, and stable ^{64}Zn and long-lived ^{57}Co ($T_{1/2} = 270\text{ d}$) start capturing protons.

Fig. 3.12: $T = 7.40 \cdot 10^8\text{ K}$, $\rho = 1.54 \cdot 10^5\text{ g cm}^{-3}$, $X = 0.535$, $Y = 0.355$, $t = -8.19643055\text{ s}$

$^{14}\text{O}(\alpha, p)^{17}\text{F}$ is now as strong as $^{15}\text{O}(\alpha, \gamma)^{19}\text{Ne}$.

The $^{46}\text{Ti}(p, \gamma)^{47}\text{V}$ -reaction, which is the bottleneck to the heavier during the early stages becomes active.

The flow in the pf -shell burns between Fe and Ni. ^{59}Cu , ^{60}Zn , and ^{65}Zn ($T_{1/2} = 244\text{ d}$) starts burning.

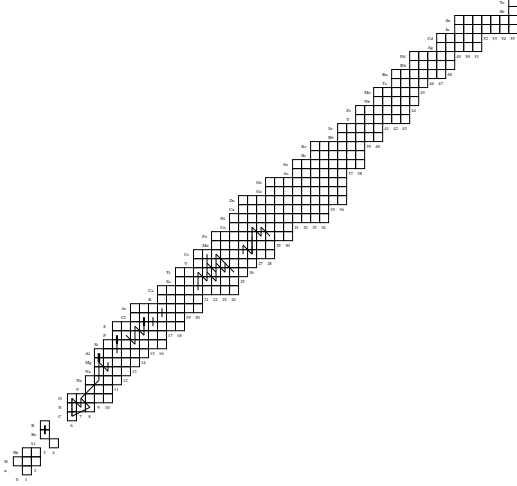


Figure 3.10: Above ignition

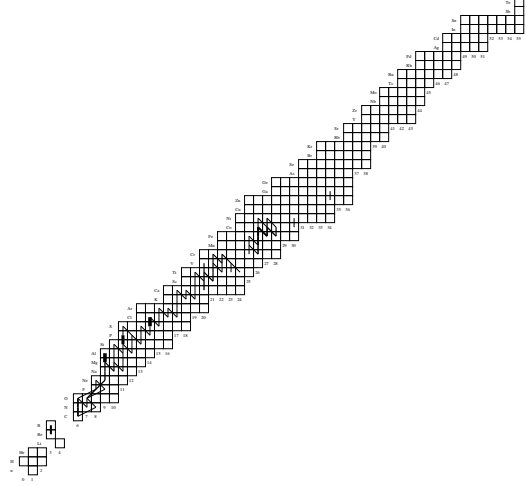


Figure 3.11: Above ignition

Fig. 3.13: $T = 8.33 \cdot 10^8 \text{ K}$, $\rho = 1.36 \cdot 10^5 \text{ g cm}^{-3}$, $X = 0.528$, $Y = 0.349$, $t = -7.7879397 \text{ s}$

Presently the flow through the lighter isotopes stops at the ^{30}S ($T_{1/2} = 1.18 \text{ s}$) waiting point with only a small flux following from its decay.

The initial residual amount of ^{40}Ca is not fully depleted and burned into the nickel-copper-zinc region. Along with the initial residual chromium, they are however stopped at the $N = 28$ isotone due to the long half-lives of ^{55}Co ($T_{1/2} = 18 \text{ h}$) and ^{56}Ni ($T_{1/2} = 6.1 \text{ d}$).

In addition stable and long lived isotopes beyond zinc slowly start to burn. However, the $^{46}\text{Ti}(p, \gamma)^{47}\text{V}$ -reaction is still too weak to connect to the flow through the lighter nuclei to iron-group flow, whence the latter moves on by itself.

Fig. 3.14: $T = 9.27 \cdot 10^8 \text{ K}$, $\rho = 1.20 \cdot 10^5 \text{ g cm}^{-3}$, $X = 0.508$, $Y = 0.336$, $t = -6.6445538 \text{ s}$

A couple of seconds after its breakout, $^{14}\text{O}(\alpha, p)^{17}\text{F}$, becomes so fast any ^{14}O is immediately destroyed. Consequently ^{15}O is only created via the hot CNO bi-cycle. However, the bi-cycle will become void, because it is now sufficiently hot for alpha-particles to penetrate the Coulomb barrier of ^{18}Ne , thus skipping its $T_{1/2} = 1.67 \text{ s}$ β^+ -decay.

The flow which started from the captures on the residual Cr isotopes, which were later processed in proton captures has now been burned beyond Co. The progression from the $N = 28$ isotone to the $N = 29$

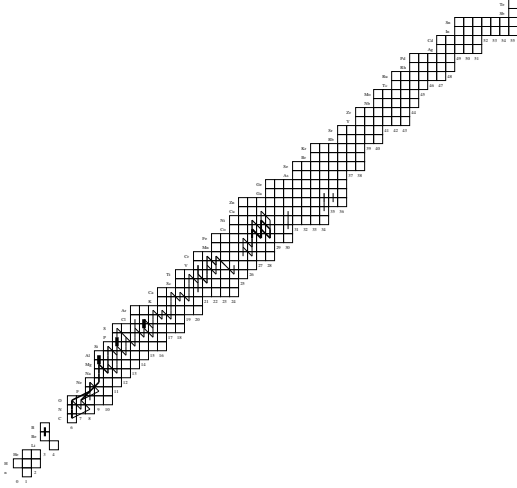


Figure 3.12: Above ignition

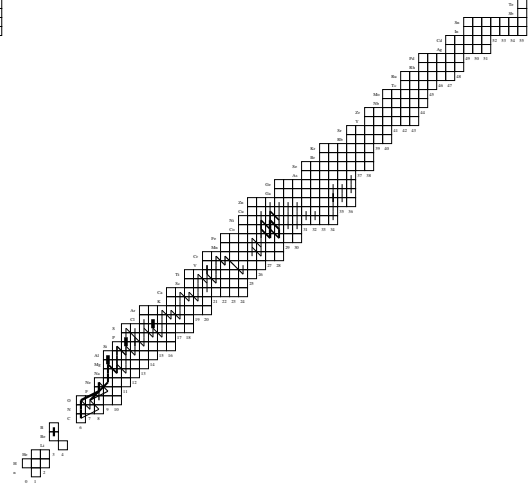


Figure 3.13: Above ignition

goes through $^{58}\text{Cu}(\beta^+, T_{1/2} = 3.2 \text{ s})$ and $^{59}\text{Zn}(\beta^+, T_{1/2} = 0.182 \text{ s})$, since a further proton capture is prevented by photodisintegration. Subsequently the flow proceeds via $^{59}\text{Cu}(p, \gamma) ^{60}\text{Zn}$ ($T_{1/2} = 2.4 \text{ m}$), which is a waiting point due to the photodisintegration of ^{61}Ga . However, a proton separation energy of $Q = 644 \text{ keV}$ permits the formation of sufficient ^{61}Ga which can either proceed via $^{61}\text{Ga}(p, \gamma) ^{62}\text{Ge}(\beta^+, T_{1/2} = 0.083 \text{ s}) ^{62}\text{Ga}$ or $^{61}\text{Ga}(\beta^+, T_{1/2} = 0.150 \text{ s}) ^{61}\text{Zn}(p, \gamma) ^{62}\text{Ga}$, whence the further flow depends on the parameters of these rates such as described earlier for similar configurations. $^{64}\text{Ge}(\beta^+, T_{1/2} = 63.7 \text{ s})$ is reached via subsequent and alternating proton captures and β^+ -decays. However, ^{65}As is proton-unbound. Therefore further flow depends on either a $2p$ -capture or a slow decay.

Meanwhile heavier previous ashes ($N > 32$) react as they are bumped up the isotones by repeated proton-captures.

Fig. 3.15: $T = 9.31 \cdot 10^8 \text{ K}$, $\rho = 1.19 \cdot 10^5 \text{ g cm}^{-3}$, $X = 0.507$, $Y = 0.335$, $t = -6.5430033 \text{ s}$

While it is evident from the flow chart that most of the flow is still blocked at ^{30}S ($T_{1/2} = 1.18 \text{ s}$), the rp -process now extends to ^{64}Ge ($T_{1/2} = 63.7 \text{ s}$) as $^{46}\text{Ti}(p, \gamma) ^{47}\text{V}(p, \gamma) ^{48}\text{Cr}(p, \gamma) ^{49}\text{Mn}$ and the (still weak) shortcut $^{46}\text{V}(p, \gamma) ^{47}\text{Cr}(p, \gamma) ^{48}\text{Mn}(p, \gamma) ^{49}\text{Fe}(\beta^+, T_{1/2} = 0.070 \text{ s}) ^{49}\text{Mn}(\beta^+ T_{1/2} = 0.382 \text{ s}) ^{49}\text{Cr}(p, \gamma) ^{50}\text{Mn}(p, \gamma) ^{51}\text{Fe}$ now closes the gap.

Heavier isotopes with $N > 32$ continue to ^{72}Kr ($T_{1/2} = 17 \text{ s}$) where the flow is stopped by photodisintegration of compound isotopes.

At this time the temperature is sufficiently high for photodisintegration of ^{27}S to prevent the shortcut, which was previously established between ^{25}Si and ^{27}P .

However, at the same temperature the $^{21}\text{Mg}(\alpha, p)$ ^{24}Al and the $^{22}\text{Mg}(\alpha, p)$ ^{25}Al reactions become significant. The latter circumvents the ($T_{1/2} = 0.102\text{ s}$) half-life of ^{25}Si , thus shortening the reaction flow timescale.

^{38}Ca starts photodisintegration, but since ^{39}Sc is proton unbound, the flow must await a ($T_{1/2} = 0.438\text{ s}$)-decay, since this reaction is a bottleneck.

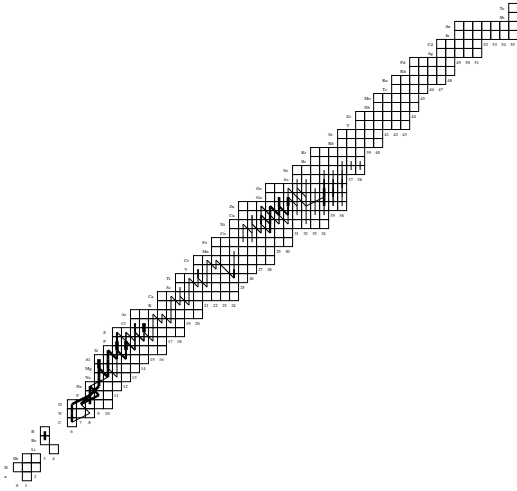


Figure 3.14: Above ignition

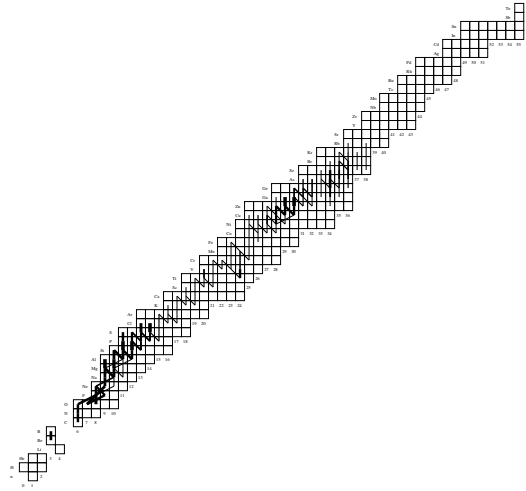


Figure 3.15: Above ignition

Fig. 3.16: $T = 9.53 \cdot 10^8\text{ K}$, $\rho = 1.17 \cdot 10^5\text{ g cm}^{-3}$, $X = 0.494$, $Y = 0.326$, $t = -5.5928312\text{ s}$

Increasing the temperature further $^{26}\text{Si}(\alpha, p)^{29}\text{P}$ now circumvents the decays of the $N = 12$ isotone decreasing the flow timescale. However, the flow must still wait at ^{30}S , which abundance increase, but while a stronger flow now passes through ^{30}S ($T_{1/2} = 1.18\text{ s}$) $^{30}\text{P}(p, \gamma)$ $^{31}\text{S}(p, \gamma)$ ^{32}Cl , $^{30}\text{S}(p, \gamma)$ (γ, p) ^{31}Cl $^{32}\text{Ar}(\beta^+, T_{1/2} = 0.210\text{ s})$ ^{32}Cl , the flow path which depends on the proton separation energy of ^{31}Cl , becomes viable. The stronger flow continues to ^{64}Ge with unchanged flow paths.

The $^{49}\text{Mn}(p, \gamma)$ $^{50}\text{Fe}(\beta^+, T_{1/2} = 0.100\text{ s})$ ^{50}Mn starts becoming competitive with $^{49}\text{Mn}(\beta^+ T_{1/2} = 0.382\text{ s})$ $^{49}\text{Cr}(p, \gamma)$ ^{50}Mn acting to decrease the effective flow rate between ^{49}Mn and ^{50}Mn .

Photodisintegration is now strong for ^{53}Ni , ^{54}Ni , and ^{55}Ni , where the former are shifted towards nickel. However, the latter proceeds via $^{55}\text{Ni}(p, \gamma)$

$^{56}\text{Cu}(p, \gamma) ^{57}\text{Zn}(\beta^+, T_{1/2} = 0.40 \text{ s}) ^{57}\text{Cu}$, which circumvents the slower $^{56}\text{Ni}(\beta^+, T_{1/2} = 6.1 \text{ d})$.

A similar phenomenon occurs for the zinc isotopes, where ^{60}Zn ($T_{1/2} = 2.4 \text{ m}$) is circumvented by $^{60}\text{Zn}(p, \gamma) ^{61}\text{Ga}(p, \gamma) ^{62}\text{Ge}(\beta^+, T_{1/2} = 0.083 \text{ s}) ^{62}\text{Ga}$.

$^{64}\text{Ge}(\beta^+, T_{1/2} = 63.7 \text{ s})$ finally becomes sufficiently abundant to yield a small flow extending the rp -process through ^{68}Se with ($T_{1/2} = 35.5 \text{ s}$), ^{72}Kr with ($T_{1/2} = 17 \text{ s}$), and ^{76}Sr with ($T_{1/2} = 9.00 \text{ s}$), which are all restricted by photodisintegration at this temperature.

Fig. 3.17: $T = 9.81 \cdot 10^8 \text{ K}$, $\rho = 1.17 \cdot 10^5 \text{ g cm}^{-3}$, $X = 0.450$, $Y = 0.302$, $t = -3.0751059 \text{ s}$

As the temperature keeps increasing, the alpha particles now become sufficiently energetic to allow the $^{30}\text{S}(\alpha, p) ^{33}\text{Cl}$ -reaction, thus breaking out of the ($T_{1/2} = 1.18 \text{ s}$) waiting point. However, the flux is relatively weak at this temperature, so the characteristic time scale is only changed slightly. The flow subsequently proceeds via $^{33}\text{Cl}(p, \gamma) ^{34}\text{Ar}$ ($T_{1/2} = 0.844 \text{ s}$), which is the next waiting point. For these types of burst, the temperature never becomes sufficiently high for the (α, p) -process to continue beyond this point. For less charged targets, however, the (α, p) -process completely dominates the flow.

Opening the $^{46}\text{Cr}(p, \gamma)$ -reaction, a shortcut between ^{46}Cr and ^{48}Mn becomes viable. This combines with the $^{46}\text{V} \rightarrow ^{49}\text{Mn}$ -shortcut creating a super-shortcut between ^{46}Cr and ^{49}Mn , where all rates are important.

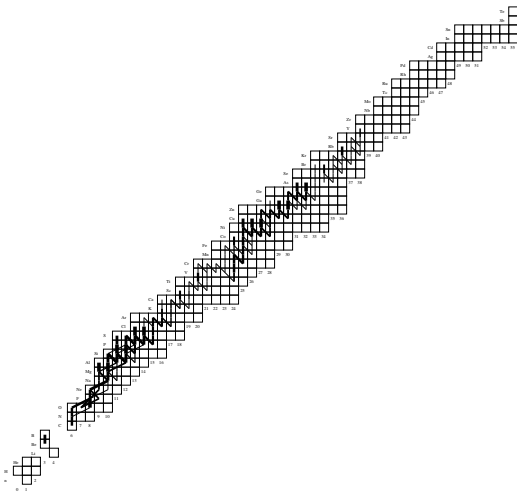


Figure 3.16: Above ignition

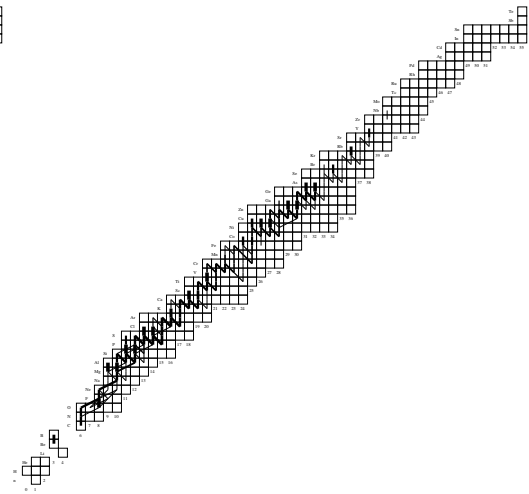


Figure 3.17: Above ignition

Fig. 3.18: $T = 1.00 \cdot 10^9 \text{ K}$, $\rho = 1.19 \cdot 10^5 \text{ g cm}^{-3}$, $X = 0.408$, $Y = 0.291$, $t = -1.0917942 \text{ s}$

This region has now reached its maximum temperature; the reaction flow-path is identical to the flow in Fig. 3.17, but due to the higher temperature the flow is faster.

Fig. 3.19: $T = 9.06 \cdot 10^8 \text{ K}$, $\rho = 1.68 \cdot 10^5 \text{ g/cm}^3$, $X = 0.280$, $Y = 0.237$, $t = 6.67416000 \text{ s}$

There is still plenty of hydrogen and the temperature is above 0.9 GK, so the flow continues to develop with more isotopes reaching ^{64}Ge . A very weak leak now exists due to the double proton capture $^{64}\text{Ge}(p, \gamma) ^{65}\text{As}(p, \gamma) ^{66}\text{Se}(\beta^+, T_{1/2} = 0.071 \text{ s}) ^{66}\text{As}$ shortcut, and following the decay of ^{76}Kr the flow eventually reaches ^{80}Sr .

In addition trace amounts of ^{84}Tc are produced – this effectively constitute the end of the rp -process, which is short of the prediction of Schatz et al. (1999), the reason being the much lower peak temperature achieved by our model.

The high temperature also allows (p, α) -reactions on ^{59}Cu and ^{63}Ga , which return to the ^{56}Ni and ^{60}Zn waiting points respectively.

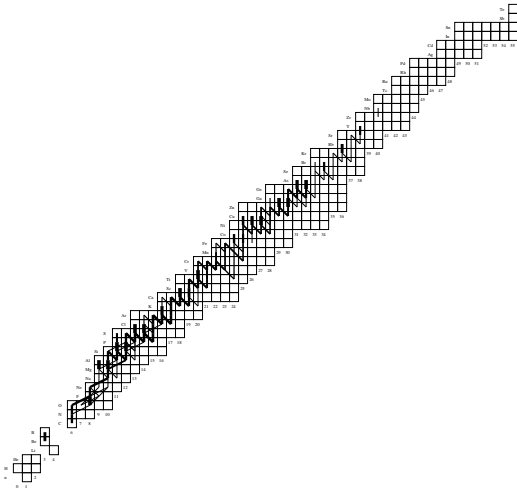


Figure 3.18: Above ignition

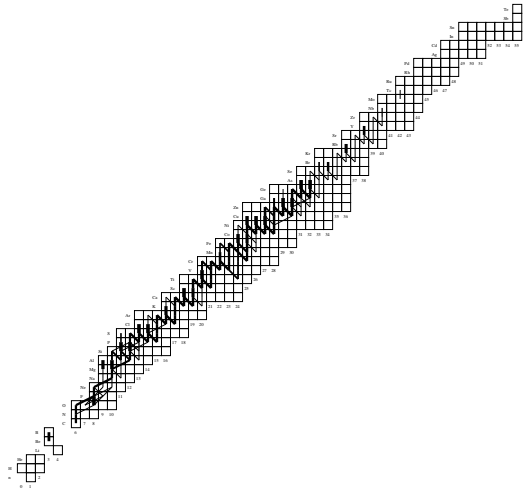


Figure 3.19: Above ignition

Fig. 3.20: $T = 7.15 \cdot 10^8 \text{ K}$, $\rho = 3.55 \cdot 10^5 \text{ g cm}^{-3}$, $X = 0.032$, $Y = 0.133$, $t = 31.704493 \text{ s}$

Half a minute after the burst the rp -process is still operating, but the hydrogen is almost depleted, and the temperature has decreased 30% from the maximum temperature. This means that the right legs of the flow paths are beginning to dominate again – in particular it means that the flow past ^{68}Se now runs slower and further away from the dripline i.e. $^{68}\text{Se}(\beta^+, T_{1/2} = 35.5 \text{ s})$ $^{68}\text{As}(p, \gamma)$ $^{69}\text{Se}(p, \gamma)$ $^{70}\text{Br}(\beta^+, T_{1/2} = 0.079 \text{ s})$ $^{70}\text{Se}(p, \gamma)$ $^{71}\text{Br}(p, \gamma)$ $^{72}\text{Kr}(\beta^+, T_{1/2} = 17 \text{ s})$ $^{72}\text{Br}(p, \gamma)$ $^{73}\text{Kr}(p, \gamma)$ $^{74}\text{Rb}(\beta^+, T_{1/2} = 0.065 \text{ s})$ $^{74}\text{Kr}(p, \gamma)$ $^{75}\text{Rb}(p, \gamma)$ $^{76}\text{Sr}(\beta^+, T_{1/2} = 9.00 \text{ s})$ $^{76}\text{Rb}(p, \gamma)$ $^{77}\text{Sr}(p, \gamma)$ $^{78}\text{Y}(\beta^+, T_{1/2} = 0.055 \text{ s})$ $^{78}\text{Sr}(p, \gamma)$ $^{79}\text{Y}(p, \gamma)$ $^{80}\text{Zr}(\beta^+, T_{1/2} = 3.90 \text{ s})$ $^{80}\text{Y}(p, \gamma)$ $^{81}\text{Nb}(\beta^+, T_{1/2} = 0.210 \text{ s})$ $^{81}\text{Zr}(p, \gamma)$ ^{82}Nb .

The lower temperature also means that the hot CNO bi-cycle becomes active again, since $^{18}\text{Ne}(\beta^+, T_{1/2} = 1.67 \text{ s})$ becomes competitive with $^{18}\text{Ne}(\alpha, p)$ ^{21}Mg again.

Fig. 3.21: $T = 6.36 \cdot 10^8 \text{ K}$, $\rho = 4.29 \cdot 10^5 \text{ g cm}^{-3}$, $X \approx 0$, $Y = 0.108$, $t = 44.85772 \text{ s}$

The hydrogen is practically exhausted from this region, so while the (α, p) -process still operates up to ^{25}Si , the flow is basically stopped at ^{46}Ti again due to lack of protons. Heavier isotopes follow constant A decay-chains back to the valley of stability.

Following this, there is a brief period of (α, p) -reactions on light isotopes close to $A = Z$, which is very similar to Fig. 3.8 and Fig. 3.9.

3.2.3 Convective region

The size of the convective region is shown in Fig. 3.3, which shows a trace of the burst conditions for different depths (pressures) during a complete revolution of the limit cycle. Note that the convective zone only exist during the phase where the temperature rises (the cycle revolves clockwise). The figure shows that the convective zone does not reach the surface for this burst, but stays in a narrow region between $y = 5.5 \times 10^6 \text{ g cm}^{-2}$ and $y = 3.3 \times 10^7 \text{ g cm}^{-2}$. The quantitative analysis of the turbulent convective burning is complicated by the mixing of matter between convective zones that occurs as soon as and as long as a superadiabatic temperature gradient is established. However, the convective timescale, $\tau_{con.} \equiv \Lambda/v_{edd.} \sim 10^{-6}-10^{-5} \text{ s} \ll \tau_{rp}$, is generally faster than the typical timescale of the rp -process whence the explosive burning may be taken to have approximately the same composition

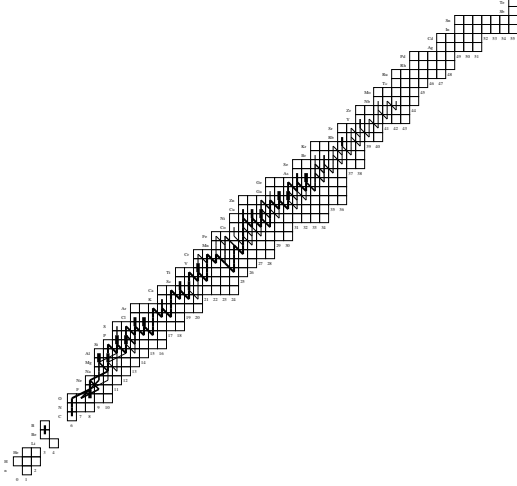


Figure 3.20: Above ignition

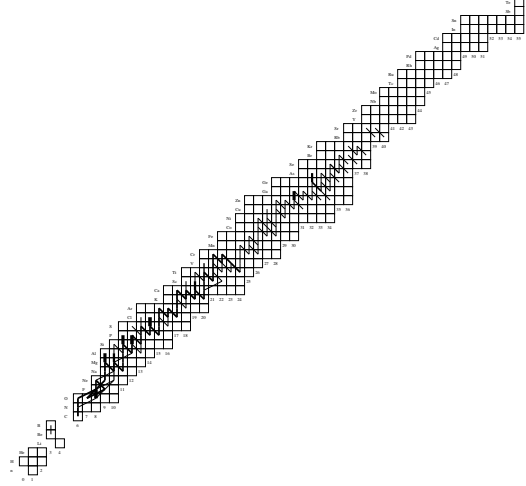


Figure 3.21: Above ignition

throughout the entire convective zone (see the convective model of Rembges (1999)) although burning happens at different temperatures and densities at the top and bottom of the convective zone respectively. Furthermore, turbulent convective burning does not happen above temperatures of 7×10^8 K, whence the (α, p) -process, which has a much shorter timescale, does not become active. Therefore this region could be computed by models with a simplified description of the compositional evolution but a more complex (2D) hydrodynamical implementation. The following analysis of this region concentrates on the bottom of the convective region, because it is hotter and denser, and therefore the reactions proceed faster here.

Fig. 3.22: $T = 6.72 \cdot 10^8$ K, $\rho = 9.81 \cdot 10^4$ g cm⁻³, $X = 0.492$, $Y = 0.272$, $t = 30.0$ s

The convective period during this burst lasts about 1.7 s in which fresh unburned matter from the top of the convective zone is mixed into the bottom and back again. This means that temperature dependent particle-captures are effectively weaker, whereas the weak decays remain unaltered.

Due to the lower pressure the region attains a maximum temperature of ~ 0.9 GK whence the high-T short cuts available to the deeper layers as described in the previous sections never come into play; instead the reaction flow mostly represented by the flow chart of Fig. 3.22.

The (α, p) -process extends to ^{26}Si after which the flow passes through $^{26}\text{Si} \rightarrow ^{28}\text{P}$ -short cut. The ^{30}S waiting point still acts as a bottleneck

with only a small leak via $^{30}\text{S}(p, \gamma) ^{31}\text{Cl} \rightarrow ^{32}\text{Ar}(\beta^+, T_{1/2} = 0.210 \text{ s}) \rightarrow ^{32}\text{Cl}$. This flow passes through the $^{34}\text{Ar}(\beta^+, T_{1/2} = 0.844 \text{ s})$ bottleneck and on through $^{37}\text{Ca}(\beta^+, T_{1/2} = 0.175 \text{ s}) \rightarrow ^{37}\text{K}(p, \gamma) \rightarrow ^{38}\text{Ca}(\beta^+, T_{1/2} = 0.440 \text{ s})$ into the pf -shell isotopes.

The $^{42}\text{Ti} \rightarrow ^{44}\text{V}$ is dominated by the lower leg, and the flow subsequently reaches the $A = 46$ decay-line which is dominated by the breakout from ^{46}Ti leading to the ^{49}Mn decay.

The flow then moves through the nickel isotopes until ^{55}Ni where its decay is now the strongest flow path. The reaction flow subsequently moves through the zinc isotopes until finally ending up in ^{64}Ge where photodisintegration effectively ends the flow at this depth.

Fig. 3.23: $T = 3.78 \cdot 10^8 \text{ K}$, $\rho = 1.81 \cdot 10^5 \text{ g cm}^{-3}$, $X = 0.417$, $Y = 0.240$, $t = 96.2 \text{ s}$

The huge thermal mass around and below the ignition region maintains the convective region at temperatures that are sufficiently high for the $^{14}\text{O}(\alpha, p) ^{17}\text{F}$ -reaction to remain active for more than a minute after the burst. Since there is still a large amount of unburned hydrogen left, the flow up to ^{49}Mn continues as before in Fig. 3.22. However, now it is no longer possible to keep the remaining flow close to the dripline, as β^+ -decays are now competitive with the slower proton-captures.

Thus Fig. 3.22 shows the building up of ^{49}Cr and ^{50}Cr from which part of the *next* burst will ignite on, once they have accreted down into the ignition region.

The waiting points ^{60}Zn , ^{64}Ge , ^{68}Se , and ^{72}Kr also start decaying back to the valley of stability. However, at this time protons still capture on the daughter particles resulting in a distribution all along the stable isotopes. Once temperatures drop below 0.3 GK proton captures on heavy particles essentially cease and isotopes are left to decay.

3.2.4 Surface

In this type of burst the convective region does not extend to the surface of our model. This means that heavier ashes are not brought to the surface, if the convective model does not severely underestimate the convective strength. Since the matter is extremely opaque with mean free photon paths of $\sim 10^{-4} \text{ cm}$, the photons are in local thermal equilibrium (LTE) and exhibit a black body spectrum with no lines, whence no direct comparisons can be made between the lines of rp -process reaction products of this model and observations.

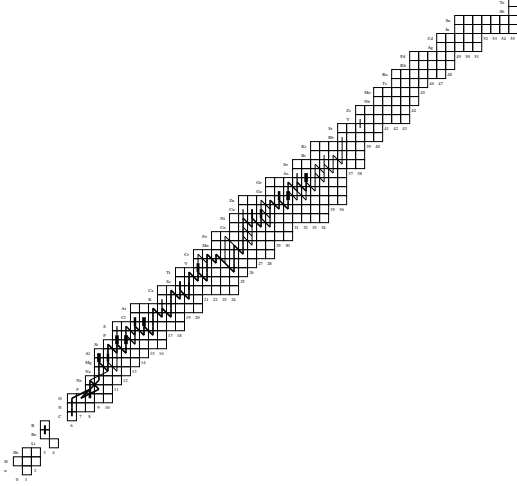


Figure 3.22: Convection region

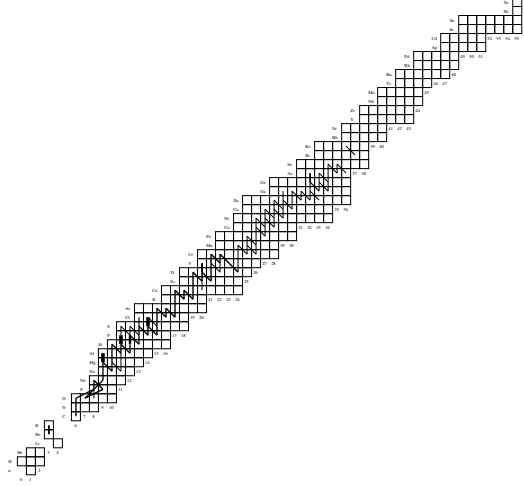


Figure 3.23: Convection region

The extent of reaction flow at this depth is shown in Fig. 3.24 and ends at ^{46}Ti , whence heavier elements in the layers above, which *would* be observable, could not have been generated by the *rp*-process. This means that fast accreting XRBs are an unlikely source of *p*-nuclei, because they are only produced deeper in the atmosphere. This region is limited by $T < 0.6$ GK and the initial reactions are characterized by proton captures on the accreted heavy elements that may have been destroyed by the surface impact (Bildsten et al. (1992)) – the abundance of heavier elements (\sim a few percents) is insignificant for this region as it does not act as a burst trigger in any way.

3.2.5 Ocean (ashes)

The inner parts of the neutron star acts as a buffer absorbing heat from the burst. However, for this accretion rate it is radiated outwards again after the burst whence it does not heat the crust (Fujimoto et al. (1984)). The early reaction flow which is caused by conductive heating (cooking) is similar to the reaction flow in Fig. 3.9. Later it is characterized by alpha-captures on alpha-chain nuclei extending to ^{36}Ar . Note that here we also have $^{12}\text{C}(p, \gamma)$ $^{13}\text{N}(\alpha, p)$ ^{16}O being much stronger than the direct $^{12}\text{C}(\alpha, \gamma)$ ^{16}O -reaction. Here the protons are supplied by many weak (α, p)-reactions on stable isotopes in the sulfur region.

Aside from the issues mentioned in sec. 1.4.1, the composition is most interesting to test the assumptions of the current superburst theory, which attempts an explanation of the eight superbursts, which have been observed

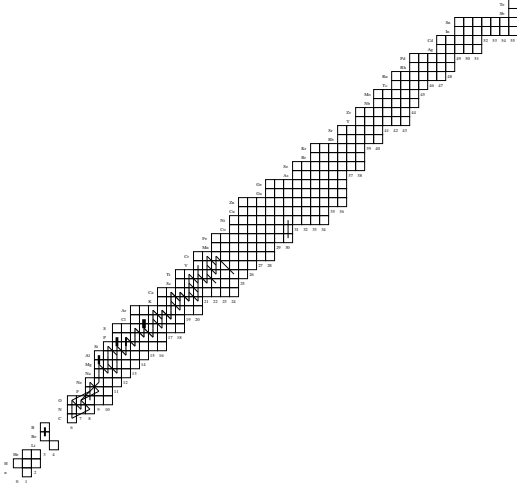


Figure 3.24: Surface

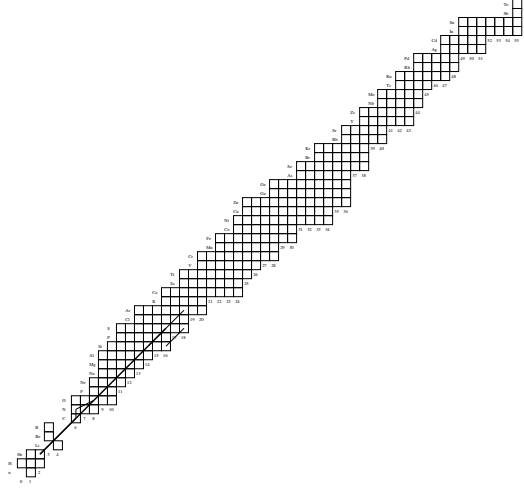


Figure 3.25: Ocean

so far (Cumming & Bildsten (2001)) The theory suggests that residual carbon becomes thermally unstable and ignites in the ocean on a timescale of years. However, this would require a large mass fraction ($X_{c12} \sim 0.1$) of ^{12}C to survive the burning to keep a recurrence timescale of years while simultaneously ensuring that rest of the ashes are as heavy as possible ($A > 100$) to ensure a steep temperature gradient and thus avoiding a stable burning of the carbon. As can be seen from Fig. 3.26, only a few percent of the carbon material survives. This is primarily because helium also survives the burst and subsequently capture on the carbon and virtually eliminates it. Also the average mass of the ashes is $A \sim 64$. This was also the result of Fisker et al. (2003) and Woosley et al. (2004).

These parameters lie outside the analytically permissible parameters of Cumming & Bildsten (2001), yet one may speculate that the analytic approximation is too crude. To confirm this a selfconsistent calculation of a superburst, which includes the tracking of thousands of XRBs generating the ashes for just one superburst, is required. This would be possible using our code.

During preliminary semianalytic calculations of superburst cooling curves, it was noticed that the triple-alpha was burning in a stable mode for about a month following the burst due to the thermal stabilizatory effects of the heat flux from the ocean and crust. This generated a mass fraction of $X_{c12} \sim 0.6(!)$ while exhausting the *troublesome* helium. Therefore all the fuel for the next superburst may be generated during the cooling of the last superburst.

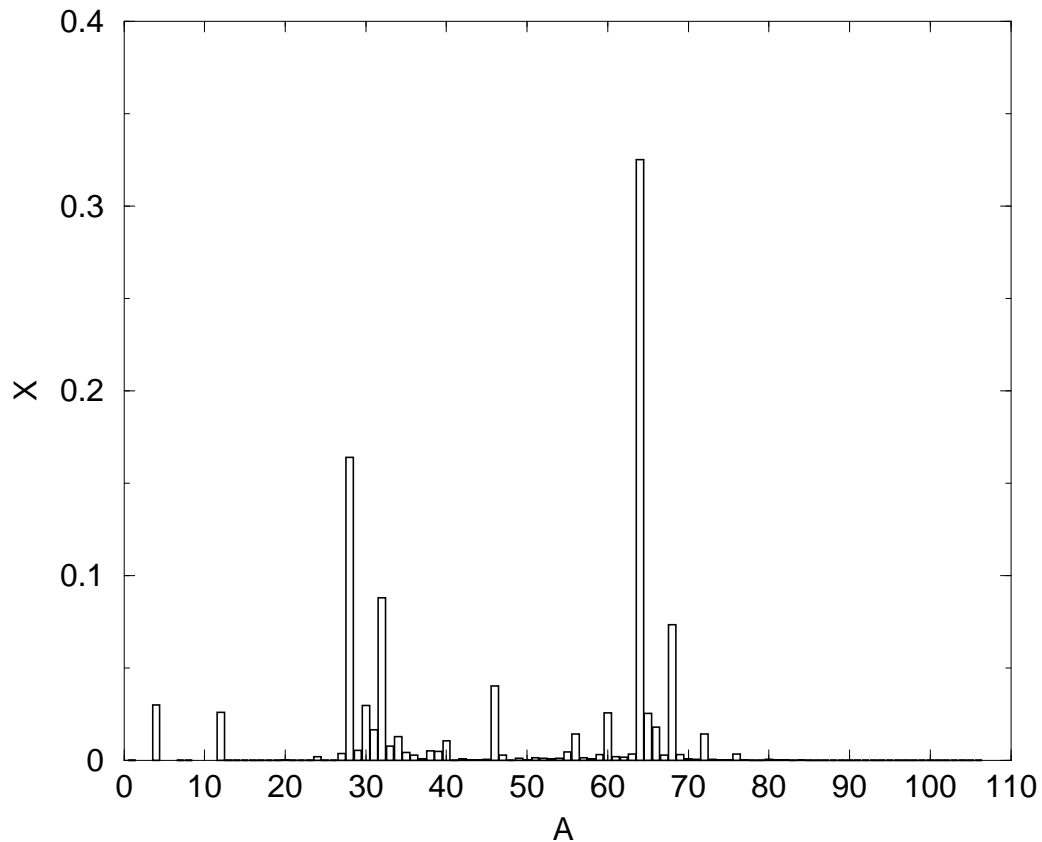


Figure 3.26: The mass fraction of the ashes about midway in between bursts plotted as a function of nucleon number: The peaks correspond to ${}^4\text{He}$; ${}^{12}\text{C}$; ${}^{28}\text{Si}$; ${}^{32}\text{S}$ and associated isotopes reacting in this region; ${}^{40}\text{Ca}$; ${}^{46}\text{Ti}$; ${}^{56}\text{Ni}$ and daughters; ${}^{60}\text{Zn}$ and daughters; ${}^{64}\text{Ge}$ and daughters; ${}^{68}\text{Se}$ and daughters; ${}^{72}\text{Kr}$ and daughters; and ${}^{76}\text{Sr}$ and daughters. Ashes heavier than $A = 40$ are primarily made above the ignition point during a burst and subsequently accreted into the ocean, whereas lighter ashes are made directly in the ocean during the helium burning in the heat bath following a burst.

Since high accretors might increase their recurrence time due to a changed accretion flow, which at this point concentrates around the neutron star equator, it may also be the carbon is generated during stable helium burning. It would require a realistic treatment of the accretion flow to determine this.

The last idea, which remains to be tested is the sensitivity to the $^{15}\text{O}(\alpha, \gamma)^{19}\text{Ne}$ -reaction rate, which despite its importance for the XRB run-away is actually poorly known ; other preliminary runs found that a decrease in this rate would also stabilize helium burning. Currently only an upper limit to this rate has been measured experimentally (Davids et al. (2003)).

Chapter 4

The He ignited flash

We consider another X-ray burst source, where $\dot{M} = 5 \cdot 10^{16} \text{ g s}^{-1}$, $M_\infty = 1.4 M_\odot$, and $R_\infty = 10 \text{ km}$. The slower accretion rate creates highly unstable helium base at the bottom of the accreted layer. Its ignition creates a large convective flux that distorts the familiar burst shape of chapter 3 and turns it into a *double peaked* shape. The shape of the double peak relies to a great extent on the “original” shape of the burst and also on the strength of the convection and the exact composition prior to the runaway.

4.1 The He flash

For a constant accreting rate of $\dot{M} = 0.045 \dot{M}_{Ed.}$ or $5 \cdot 10^{16} \text{ g s}^{-1}$, it requires about half a day before the continuous accretion process has pressed the matter down to a depth, where the helium which has now been formed in significant quantities (see Fig. 4.1) becomes thermally unstable.

As the material is pressed downwards into hotter regions the triple-alpha process starts the runaway by being the primary contributor violating the condition given by eq. [1.2].

The accumulated helium at the base burns completely within tenths of a second and reaches the Eddington limit with a maximum temperature approximately given by

$$T_{max} \approx \sqrt[4]{3P_{ign.}/a_{rad.}}, \quad (4.1)$$

since most of the pressure at the ignition point, $P_{ign.}$, is supported by radiation eventually (Koike et al. (1999); Cumming & Bildsten (2000)). The steep temperature gradient peaking at $T_9 \sim 1.4$ creates a convective region, which is sufficiently large to allow a highly efficient convective heat transport to the

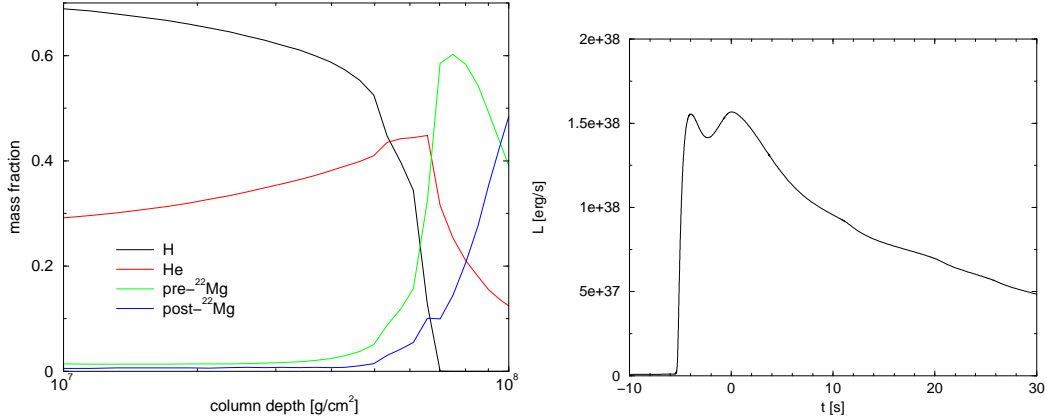


Figure 4.1: The composition of the neutron star atmosphere is shown as a function of increasing column density, $y = -\int_R^{R-r} \rho dr$, ten seconds prior to the runaway which ignites at $y \sim 0.8 \cdot 10^7 \text{ g cm}^{-2}$. Figure 4.2: $L(t)$ as a function of time. The time-scale has been synchronized so that second peak coincides with $t = 0$.

surface. Observationally this results in a rise time of the surface luminosity that is less than a second (Wallace et al. (1982)) and that is the cause of the first peak in the surface luminosity. For higher accretion rates a combined H/He flash ensues, which is slower and has weaker convection if any (See chap. 3). Therefore it is not possible to separate the two peaks for faster accretors.

The heat transport ignites the shell of mixed H/He above the ignition point. Following the breakout of the hot CNO cycle in that shell the flow up to ⁴⁰Ca is determined by a competition between the (α, p) process, (Wallace & Woosley (1981)), which is very temperature dependent, because of the strong Coloumb-barrier against alpha-capture, and the rp -process (Wallace & Woosley (1981); van Wormer et al. (1994); Schatz et al. (1998)), which is only temperature dependent in the sense that the temperature determines the ratio of the proton-rich isotopes within an isotone and thus which isotopes β^+ -decay and move the flow between the isotones (Rembges et al. (1997)). It is the detailed behavior of this flow, which determines the burst behavior following the first peak. If the reaction flow stops at a “waiting-point” isotope, the nuclear energy release rate decreases and causes a dip in the surface luminosity.

4.2 *sd*-shell structure

If the flowpaths have a simple and known structure, then an analysis of the influence of the reaction rates can be performed without involving the full detailed numerical machinery of e.g. chap. 3, but rather by considering the strength of different competing reaction rates (Fisker et al. (2004)); this is done below.

Since the isotopes in the *sd*-shell exhibit structure (see Fig. 4.3), general statements on the flow can be made. The even-even $T_z \equiv (N - Z)/2 = -1$

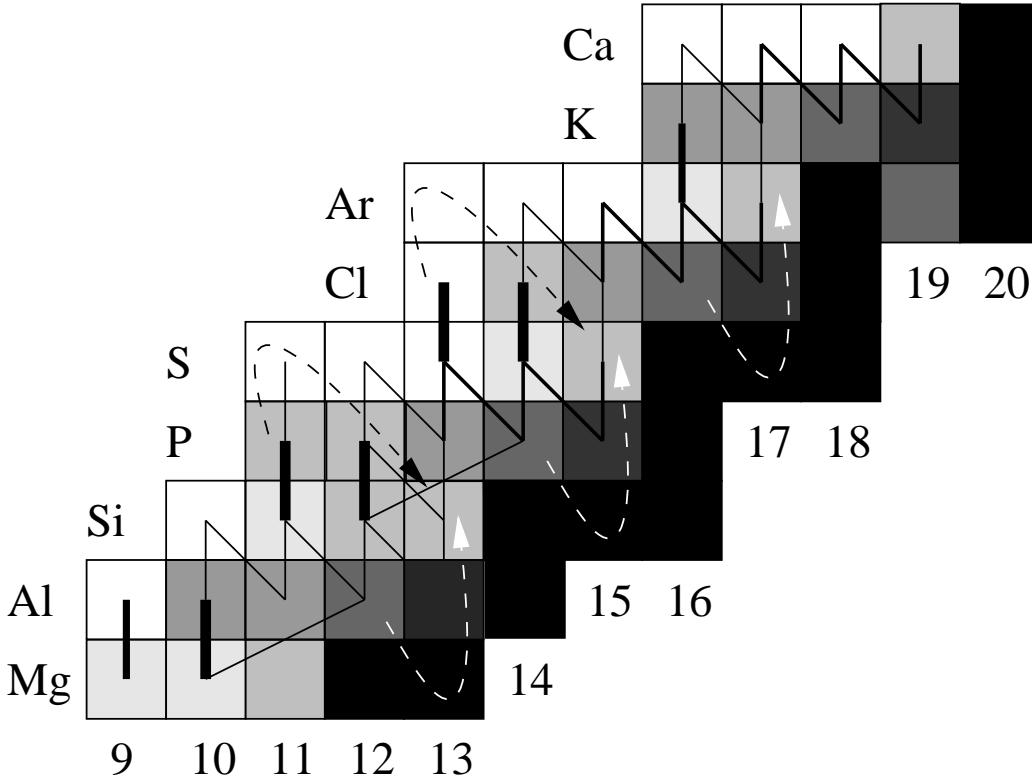


Figure 4.3: Targets with (p, γ) Q -values of ≤ 0.0 , $0.0-0.5$, $0.5-2.5$, $2.5-3.5$, $3.5-5.5$, $5.5-8.0$ in increasing levels of gray. Stable nuclei are colored black. The reaction flow rates, $f_{ij} = \dot{Y}_{i \rightarrow j} - \dot{Y}_{j \rightarrow i}$, during the burst peak temperature are shown in solid lines. The thickness indicates the strength of the reaction flow with the exception of isotopes in (p, γ) - (γ, p) equilibrium which are shown in thick lines though the net flow is close to zero. The reaction paths which circumvent the waiting points are indicated with dashed arrows (see. 4.2.2)

isotopes ^{22}Mg , ^{26}Si , ^{30}S , and ^{34}Ar , we consider, are significant waiting points

because most of the reaction flow passes through them. The isotopes become actual waiting points depending on the interplay between the temperature-dependent branching reactions which link these isotopes to other isotopes in the reaction network. These reactions will be explained now.

The potential waiting point isotopes have low (p, γ) Q -values (colored red in Fig. 4.3), so as the temperature exceeds $T_9 \sim 1$ they enter (p, γ) - (γ, p) equilibrium (shown by double arrows in Fig. 4.3) with their proton capture compound isotope (Thielemann et al., 1994), whence the ratio of the target and the compound isotope becomes proportional to a Boltzmann factor, $\exp(-k_B T/Q)$, along with a spin statistics factor and independent of the reaction rate. For (p, γ) -reactions with low Q -values this shifts the ratio back towards the waiting point nuclei. Therefore the leak via the β^+ -unstable compound isotope is insignificant, when the equilibrium has been reached, effectively blocking the reaction flow through that path. The isotopes are generally produced by proton induced captures and in addition to the (p, γ) - (γ, p) equilibrium and the β^+ -decay a third branching of the flow from these isotopes originates in the (α, p) -process which commences on ^{14}O and proceeds via $^{14}\text{O}(a, p)$ $^{17}\text{F}(p, \gamma)$ $^{18}\text{Ne}(a, p)$ $^{21}\text{Na}(p, \gamma)$ $^{22}\text{Mg}(a, p)$ $^{25}\text{Al}(p, \gamma)$ $^{26}\text{Si}(a, p)$ $^{29}\text{P}(p, \gamma)$ $^{30}\text{S}(a, p)$ $^{33}\text{Cl}(p, \gamma)$ $^{34}\text{Ar}(a, p)$ $^{37}\text{K}(p, \gamma)$ ^{38}Ca . Therefore the destruction rate (see e.g. van Wormer et al. (1994)) of these β^+ -unstable isotopes with decay times of a few seconds depends on the interplay between one production reaction and three destruction reactions whose exact details depend on nuclear data and the density and temperature due to the interaction with the hydrodynamics.

4.2.1 The waiting point isotopes

The waiting point impedance occurs close to peak temperature when the matter ends up in the potential waiting point candidate, $^A_Z X$, where further flow is blocked because the isotope is in (p, γ) - (γ, p) equilibrium with $^{A+1}_{Z+1} X$. It could also be that the $^A_Z X(p, \gamma)^{A+1}_{Z+1} X$ is too slow to cause a significant flow away from $^A_Z X$, but for an X-ray burst this is most likely not the case. Penetrating the Coulomb barrier with an alpha-particle requires a high temperature, so unless the temperature is sufficiently high for the (α, p) -reaction to carry on the flow, the flow has to await for the β^+ -decay to proceed. If a major part of the mass is blocked at a waiting point, naturally few reactions can occur. This results in a dip in the energy generation rate, which translates to the surface producing the dip in bolometric surface luminosity.

4.2.2 The paths around the waiting points

The potential waiting point isotopes are important because most of the reaction flow passes through them. Consequently they are also bottlenecks of the flow. The reason is that for high temperatures the flow is shifted towards the proton dripline, thus only two possible flow paths circumventing them need consideration. The first path depends on branching between the β^+ -decay ($t_{1/2} \sim$ few seconds) of the even-N $T_z = -1/2$ isotope and the proton-capture going to the bottleneck, but because of the high temperature the proton-capture rate is very much larger making the decay insignificant in comparison. The second path would depend on double β^+ -decays of very proton-rich isotopes between successive odd-Z isotones.

4.3 The reaction flow

This section describes reaction flow of the second burst of the base model. As mentioned in section 4.2 the isotopic properties exhibit a certain structure (see Fig. 4.3). This results in consecutively repeated patterns of the flow as seen in Fig. 4.4. The flow through the various patterns differ because the isotopic properties are not exactly identical and because the out-flow of the first pattern comprise the in-flow of the second pattern, etc., while the hydrodynamics respond on a time-scale comparable to the flow through all patterns.

The first pattern starts with the $T_Z = (N - Z)/2 = -1$ isotope, ^{22}Mg . It is in $(p, \gamma)(\gamma, p)$ equilibrium with ^{23}Al , which is not completely photodisintegrated because the Q -value ($Q = 126.4$ keV) is sufficiently high. The small amount of ^{23}Al ($Y_{23\text{Al}}/Y_{22\text{Mg}} \sim 5 \cdot 10^{-5}$) captures another proton to form ^{24}Si . This isotope has a half-life of $T_{1/2} = 0.102$ s and decays to ^{24}Al followed by a proton capture to ^{25}Si which is in $(p, \gamma)(\gamma, p)$ equilibrium with ^{26}P which may capture another proton. The flow along this branch is weak and instead ^{25}Si decays to ^{25}Al with $T_{1/2} = 0.220$ s. A larger fraction of the flow to this isotope proceeds directly via the $^{22}\text{Mg}(\alpha, p)^{25}\text{Al}$ -reaction. The half-life of ^{25}Al ($T_{1/2} = 7.2$ s) is

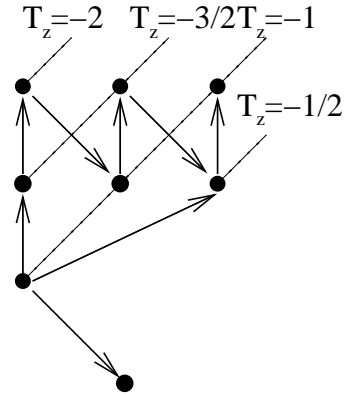


Figure 4.4: Although the pattern resembles the hot CNO cycle it is not a cycle but a competition between the “sawtooth” rp -process, an (α, p) -reaction, and a β^+ -decay.

long compared to the time-scale of the burst. Therefore the flow branching via its β^+ -decay is insignificant and the flow can only proceed via $^{25}\text{Al}(p, \gamma)^{26}\text{Si}$, which becomes a bottle neck of the entire reaction flow.

The pattern repeats for the next $T_Z = (N - Z)/2 = -1$ isotope, ^{26}Si , which is in $(p, \gamma)(\gamma, p)$ equilibrium with ^{27}P . Here the Q -value ($Q = 893$ keV) is large ($Y_{27\text{P}}/Y_{26\text{Si}} \sim 0.1$) so the “saw-tooth” path $^{27}\text{P}(p, \gamma)^{28}\text{S}(\beta^+)^{28}\text{P}(p, \gamma)^{29}\text{S}(\beta^+)^{28}\text{P}$ trumps the now comparably weaker (α, p) reaction path which is starting to feel the effect of the Coulomb barrier. A third path is the branching via $^{26}\text{Si}(\beta^+)$ followed by multiple proton captures, but since ^{26}Si has a half-life of $T_{1/2} = 2.2$ s, the flow through this path is comparably weak, so the two dominant paths coincide at ^{29}P . Here the $^{29}\text{P}(p, \gamma)^{30}\text{S}$ -reaction comprise another bottle neck, because the $^{29}\text{S}(p, \gamma)^{30}\text{Cl}(\beta^+)^{30}\text{S}$ -reaction path is suppressed, since the Q -value of the (p, γ) reaction is only 313 keV.

The resulting $T_Z = (N - Z)/2 = -1$ isotope, ^{30}S , is in $(p, \gamma)-(\gamma, p)$ equilibrium with ^{31}Cl and the equilibrium is strongly shifted towards ^{30}S , because the Q -value of the (p, γ) reaction is only 293 keV. Thus the flow can only go via $^{30}\text{S}(\beta^+)^{30}\text{P}$ ($T_{1/2} = 1.18$ s) or via the experimentally unknown $^{30}\text{S}(\alpha, p)^{33}\text{Cl}$ that is effectively blocked because of the now strong Coulomb barrier. This is demonstrated in Fig. 4.5, which shows the condition

$$\lambda_{\beta^+} = N_A \rho Y_\alpha \Delta(T) < \sigma v >_{(\alpha, p)}, \quad (4.2)$$

which demarcates the (ρ, T) -space between a dominant β^+ -decay (below the line) and a dominant alpha capture (above the line) assuming that $Y_\alpha = 0.5/4 = 0.125$, where the temperature dependent function $\Delta(T)$ accounts for the uncertainty in the reaction rate which is set to be constant for the sake of simplicity. Plotting eq. [4.2] with $\Delta(T) = 10^2$ and $\Delta(T) = 10^{-2}$ gives an estimate of the effect of the uncertainty of the reaction rate. The plot ignores the (p, γ) -reaction leak which would move the line downwards.

Since ^{30}S is the product of the $^{29}\text{P}(p, \gamma)^{30}\text{S}$ bottleneck-reaction, most of the flow passes through ^{30}S , and since this flow can only proceed via the $T_{1/2} = 1.18$ s β^+ -decay, which is comparable to the burst-timescale, the isotope becomes a waiting point, unless the hydrodynamical model has underestimated the temperature or the theoretical $^{30}\text{S}(\alpha, p)^{33}\text{Cl}$ -rate is underestimated. If most of the mass is locked up in a waiting point then few nuclear reactions occur and $\epsilon_{nuc.}$ decreases as noted at the end of section 4.2. This is observed as a dip in the bolometric surface luminosity as shown in Fig. 4.2. Following the β^+ -decay of ^{30}S , the flow proceeds via multiple proton captures through $^{30}\text{P}(p, \gamma)^{31}\text{S}(p, \gamma)^{32}\text{Cl}(p, \gamma)^{33}\text{Ar}(\beta^+)$ ending up at ^{33}Cl , which may also be reached by $^{30}\text{S}(\alpha, p)^{33}\text{Cl}$, however, the flow through this channel is insignificant as shown above in Fig. 4.5.

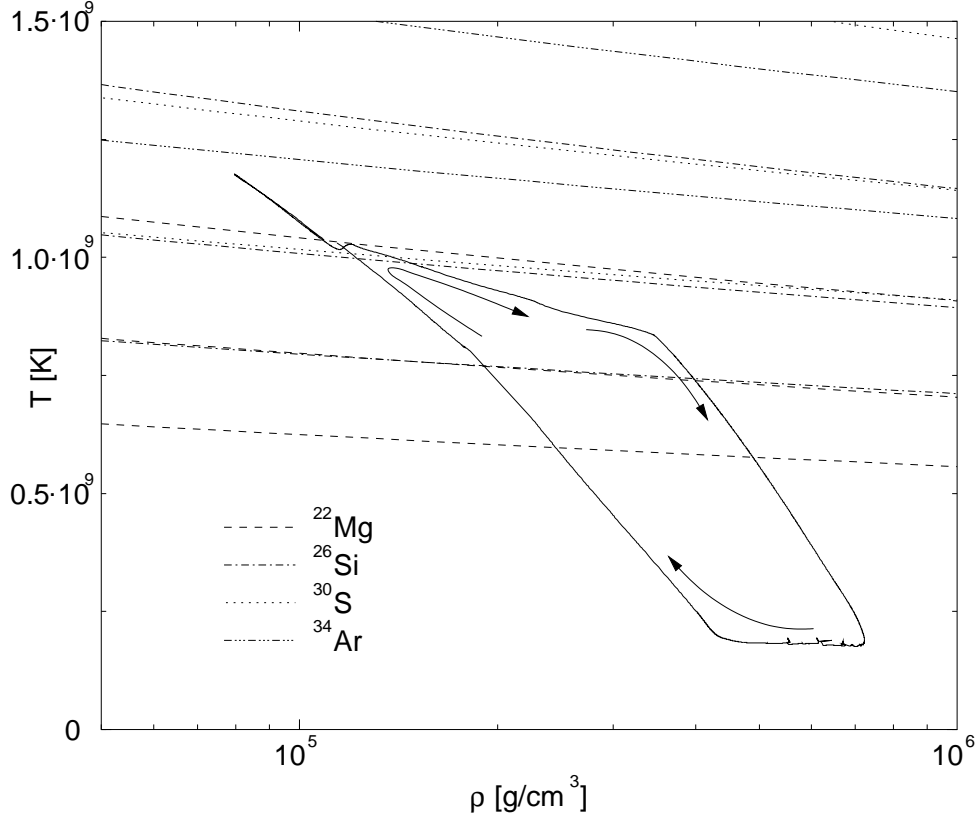


Figure 4.5: The demarcation lines of eq. [4.2] are plotted thrice with $\Delta(T) = \{10^{-2}, 1, 10^2\}$ and $Y_\alpha = 0.125$ for the ^{22}Mg , ^{26}Si , ^{30}S , and ^{34}Ar isotopes. The demarcation line for underestimating $^{34}\text{Ar}(\alpha, p)^{37}\text{K}$ by a factor 10^2 falls outside the graph. In addition the solid line shows the thermodynamic trace of the shell conditions during a full burst cycle. The arrows indicate the time direction of the cycle.

At the $T_Z = (N - Z)/2 = -1$ isotope, ^{34}Ar , the previously discussed pattern emerges again. The $^{34}\text{Ar}(p, \gamma)^{35}\text{K}$ has a Q -value of 78keV ($Y_{35\text{K}}/Y_{34\text{Ar}} \sim 2 \cdot 10^{-5}$) effectively blocking the “saw-tooth” path. Additionally the (α, p) reaction path is blocked due to the strong Coulomb barrier so the β^+ -decay half-life with $T_{1/2} = 0.839$ s is the strongest branch again; this is also readily demonstrated in Fig. 4.5.

Since similar conditions exists for ^{30}S and ^{34}Ar , they become waiting points building up their mass fraction, until they decay. This is directly seen in Fig. 4.6, and Fig. 4.7, which show the evolution of ^{30}S , and ^{34}Ar . These two isotopes are also the most abundant isotopes during the early flow.

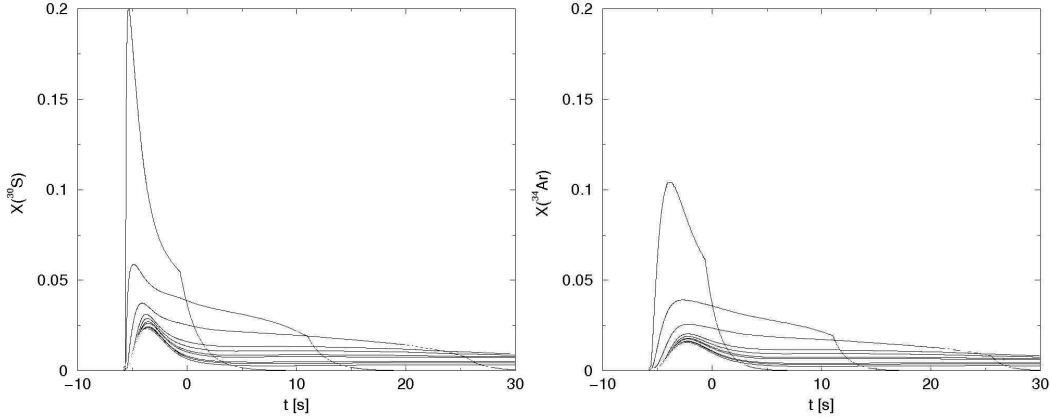


Figure 4.6: The mass fraction of ^{30}S as a function of increasing column density. Figure 4.7: The mass fraction of ^{34}Ar for the same column densities as in Fig. 4.6.

4.4 Observational features (double peaks)

While most of the observable burst sources show a single peak in the luminosity curve, some burst observations have shown a double peaked structure in the bolometric light curve¹ (Sztajno et al. (1985); van Paradijs et al. (1986); Penninx et al. (1989); Kuulkers et al. (2002) and possibly Seon & Min (2002)). Several theories have been proposed to explain such double peaks: Heat transport impedance in a two-zone model (Regev & Livio (1984)), localized burning (Shara (1982)), interactions with the accretion disc (Melia & Zylstra (1992)), a result of a H flash developing into a combined H/He flash (Hanawa & Fujimoto (1984)), shear instabilities (Fujimoto et al. (1988)) or increased proton capture on heavier nuclei (Ayasli & Joss (1982)).

Above we have suggested an explanation similar to Hanawa & Fujimoto (1984), where the convective heat transport of the helium flash drives the first peak and the rp -process and its waiting points determine the second peak. The model output is too crude to compare directly with observations, but figures 4.8–4.11 show that subsequent bursts from the same “source” (model) may vary quite a lot.

Whereas most of the real-world double peaked bursts tend to have a dominating first peak, our model tends to have a dominating second peak. This suggests that either our convective model is too weak or that the helium does

¹Not to be confused with an ordinary double peaked burst, which is simply the result of reaching the Eddington luminosity, which lifts, expands, and cools the envelope thus moving its black body spectrum out of the satellite counters giving the false impression that the luminosity has decreased. See e.g. Paczyński (1983a) for an explanation.

not burn sufficiently hot. The later would be the case, if the triple-alpha reaction is too slow during the explosive burning, or if the burst ignites too early at a lower depth thus limiting its peak temperature c.f. eq. [4.1].

Taam et al. (1996) and Woosley et al. (2004) obtained irregular burst recurrence times by decreasing the accreted abundance of CNO type material². Since such isotopes may be destroyed on impact (Bildsten et al. (1992)), there is some uncertainty regarding their concentration. This work only considers a solar abundance composition of the accreted matter.

The separation between the two peaks is due to the nuclear waiting points explained in chap. 3, whence a comparison with observations might give hints as to whether the reaction flow can break out of a given waiting point or not. In our model the separation tends to around 4-5 seconds – the observed bursts tend to have a shorter peak separations.

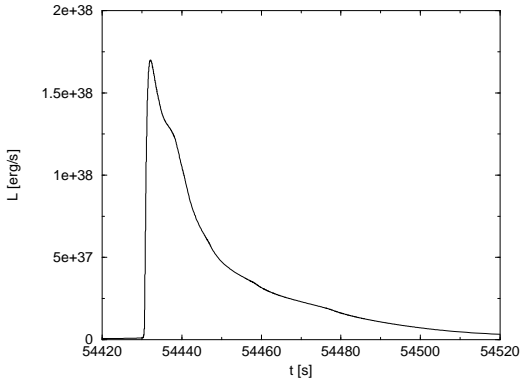


Figure 4.8: First burst

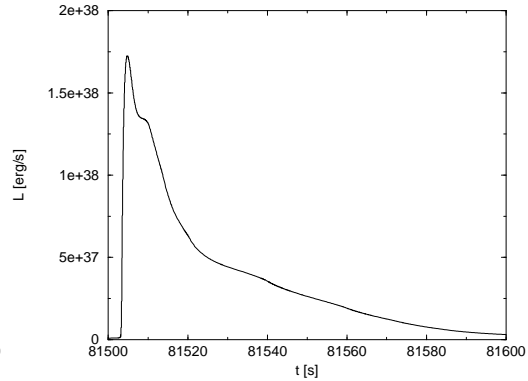


Figure 4.9: Second burst

4.4.1 Mass ejection and spectral lines

This type of burster sometimes acquire enough helium at the base layer to make the convection region extend to the surface. There the matter may be thrown out into the accretion disk and subsequently ejected. It only needs to acquire enough kinetic energy to overcome the gravitational potential up to the innermost stable orbit of the disk.

²Following the discussion in sec. 3.1 the reason is actually quite obvious: The hot CNO cycle rate and therefore the helium production rate depends on the concentration of CNO material, whence lower accreted abundances means that characteristic burning timescale becomes much larger with the implied inherent uncertainty (see also Fujimoto et al. (1987a))

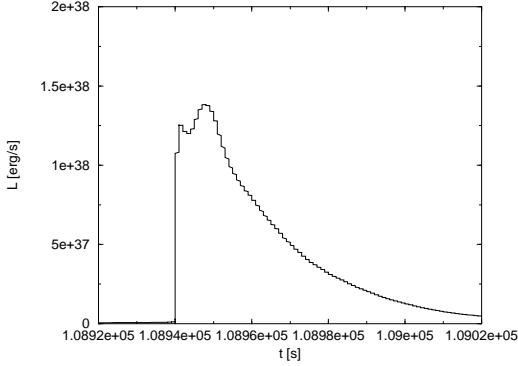


Figure 4.10: Third burst

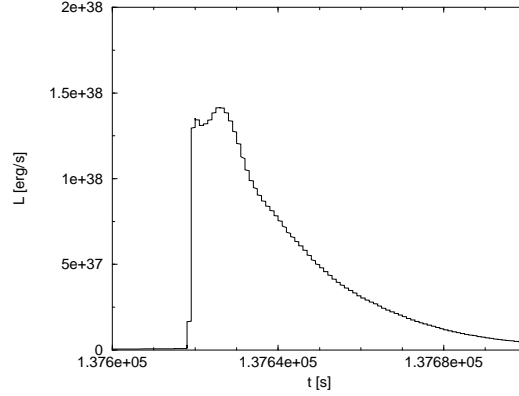


Figure 4.11: Fourth burst

Fig. 4.12 indicates the convective strength as a function of depth and time. Note that even the random component of the velocities is very much smaller than the escape velocity of the neutron star, but even if the matter is not thrown out, its composition may still be observed during this period, since the convective overturn extends to the surface for a brief period around $t \sim -1.75$ s, whence the chemical composition of deeper layers may be observed. Since the reaction flow has not proceeded very far at this point, only lighter waiting point isotopes such as ^{30}S and ^{46}Ti has been created.

A direct observation of the spectral lines of ^{30}S and ^{46}Ti would however indicate that they are indeed waiting points. This permits conclusions on the burst temperature, the convective model, and/or the reaction rates linking to these isotopes.

4.5 Specific reaction rate effects

4.5.1 $^{30}\text{S}(\alpha, p)^{33}\text{Cl}$ and $^{34}\text{Ar}(\alpha, p)^{37}\text{K}$

We investigate the relevance $^{30}\text{S}(\alpha, p)^{33}\text{Cl}$ and $^{34}\text{Ar}(\alpha, p)^{37}\text{K}$ on the burst shape by assuming a local rest mass accretion rate of $M = 5 \cdot 10^{16} \text{ g s}^{-1}$ and computing the bolometric luminosity curves for the current (α, p) -reaction rates, which are based on the code `NON-SMOKER` (Rauscher & Thielemann, 2001). In addition luminosity curves were computed assuming that the $^{30}\text{S}(\alpha, p)^{33}\text{Cl}$ and $^{34}\text{Ar}(\alpha, p)^{37}\text{K}$ -reaction rates have been underestimated by a factor 100 i.e. $\Delta(T) = 100$ in eq. [4.2]. This implicitly tests any uncertainty in the β^+ -decay half lives. The luminosity curves are shown in Fig. 4.14, while a trace of the temperature and density is shown in Fig. 4.5 using the unaltered reaction rates. Fig. 4.14 shows that if the $^{30}\text{S}(\alpha, p)^{33}\text{Cl}$ -reaction

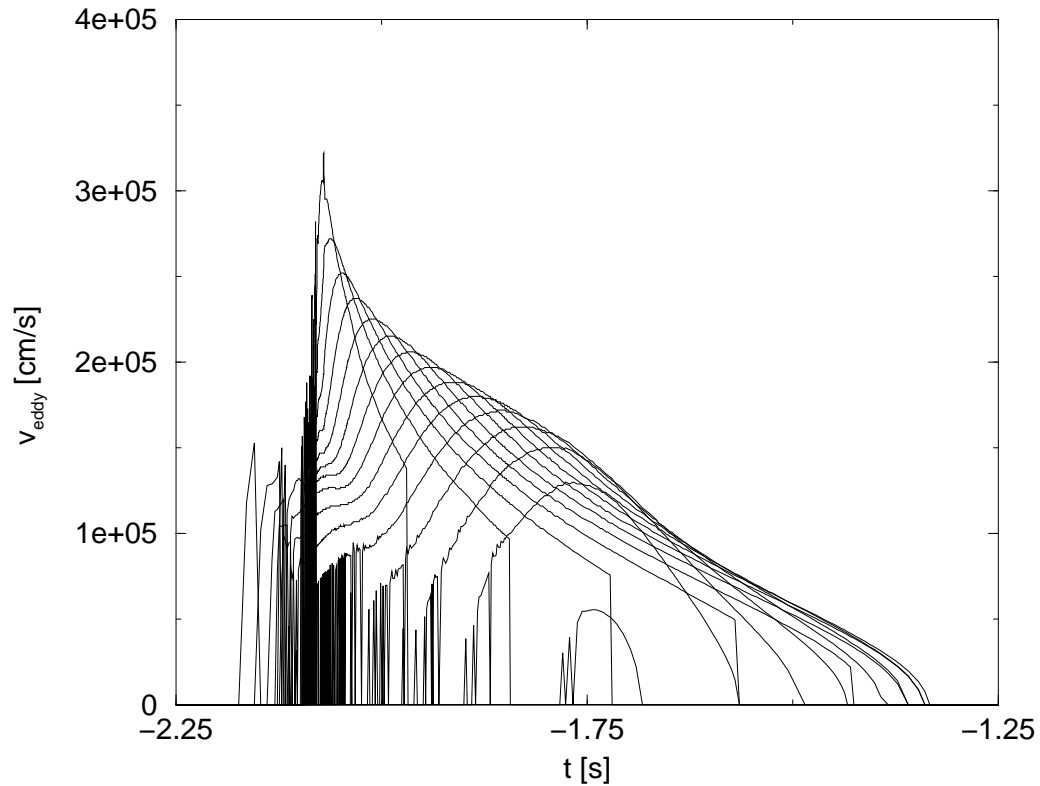


Figure 4.12: The velocity of the eddies (i.e. the random component of the velocity field) in the convective zone as a function of time. In this graph the time coordinate has been synchronized to coincide with the *first peak*. The innermost “bubble”-shaped curve at $t \sim -1.75$ s describe the speed of the eddies reaching the surface. The second innermost curve describes the region just below it and so on. The “noisy” behavior during the build-up of the convection is due to the limitations of static convective model (see sec. A.5.1).

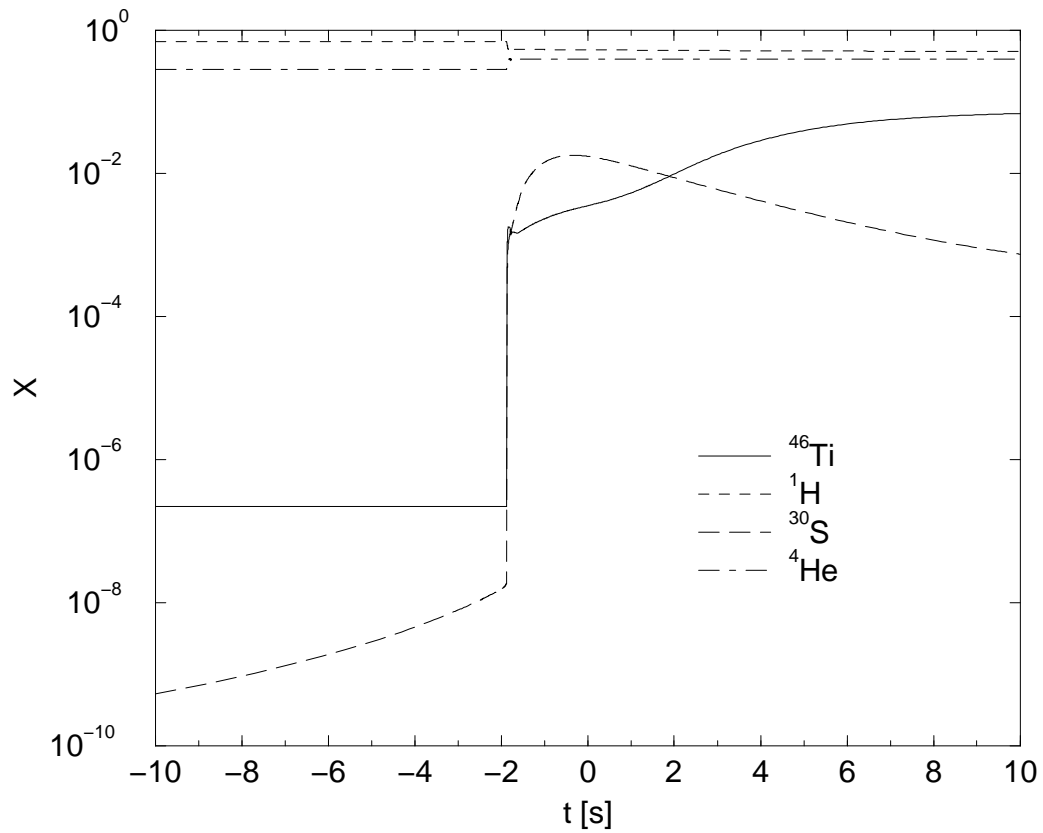


Figure 4.13: The mass fraction at the surface of the most abundant isotopes. The timescale is as in Fig. 4.12; notice that the composition changes almost instantly once the convective bubbles reach the surface around $t \sim -1.75$ s.

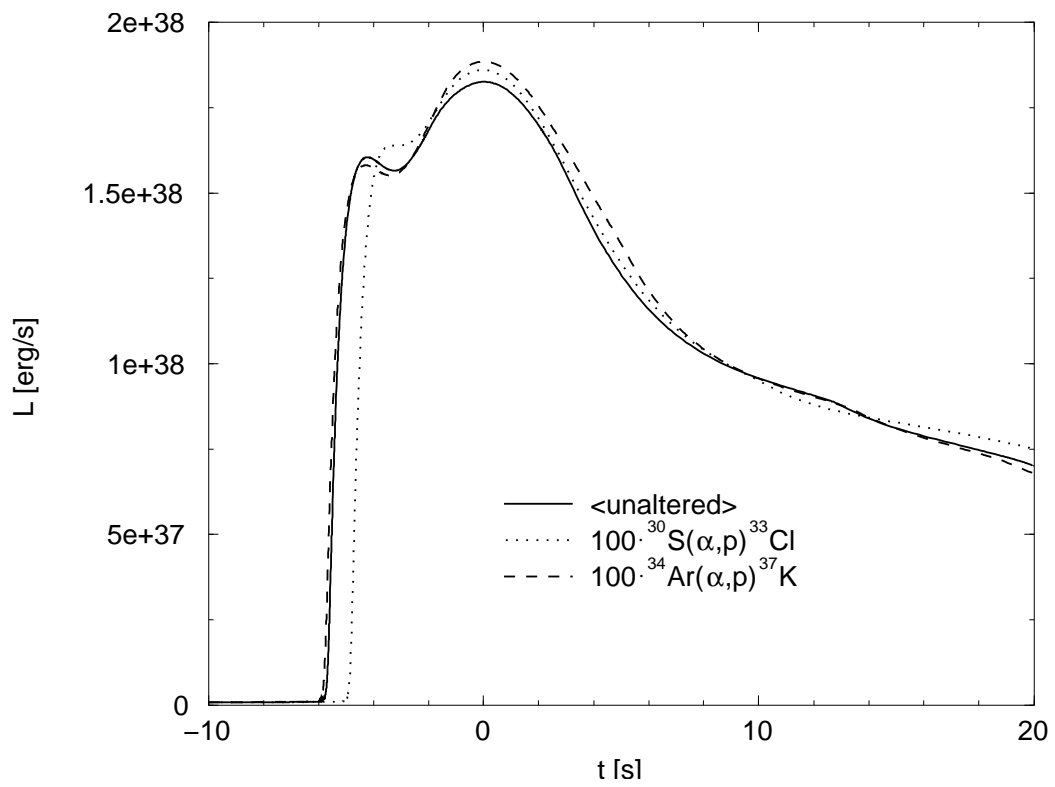


Figure 4.14: The computed luminosity is plotted as a function of time for the three cases. The three luminosity curves have been synchronized to make the second burst peaks coincide.

were faster then the dip in the luminosity would decrease or possibly be eliminated. Increasing the $^{34}\text{Ar}(\alpha, p)^{37}\text{K}$ -reaction decreases the dip slightly, indicating that the ^{34}Ar -waiting point plays a smaller role in creating the full dip in the unaltered model. In both cases increasing the rate of either (α, p) -reaction increases the luminosity of the second peak, indicating that a combination would increase the luminosity further.

Chapter 5

Summary

This work is the first extensive investigation of the nuclear reaction flow of an XRB under realistic conditions. It has been made possible by building a new computational model. This model distinguishes itself by introducing for the first time: the full general relativistic hydrodynamical equations, a relativistically corrected grey atmosphere, a relativistically corrected convection, modern approximations of the opacities and conductivities, neutrino losses, and a realistic inner boundary describing the core as a function of the nuclear EOS and neutrino cooling.

In addition all quantities are solved by conservative equations allowing a precise tracking off all released energy. This reveals details in the luminosity, which can be considered unprecedented. Yet the complicated coupling between different layers make an analysis of the nucleosynthesis based on the luminosity curve a dubious business, so except for crude predictions, one should be wary of making definite conclusions between observations, theory, and experiment when so many steps with too much room for uncertainty are involved (Shannon & Weaver (1963)).

The main result of our calculations is complete description of the reaction flow – including branchings and waiting points – as a function of realistic temperatures and densities, which is hopefully useful to the reaction library community to help determine the focus of their efforts.

Furthermore we showed that:

- ... the peak burst temperature is not as high as previously assumed. This means that tellurium is not generated in quantity. The average mass of the ashes is ~ 64 . At the same time carbon is basically destroyed by helium captures thus exiting the parameter space of current superburst theories.

- ... convection does not hit the surface for mixed hydrogen/helium bursters. Therefore we predict that spectral lines, observed during such bursts, are not due to material, which was burned at any significant depth.

...convection extending to the surface is present in helium ignited bursters. Here we predict a sudden rise in helium, sulfur, and titanium as the turbulent overturn breaches the surface accompanied by a sudden decline of hydrogen, which is mixed into the star.

... an interplay between the helium flash and the rp -process produces a roughly identifiable structure in the burst, which has been observed.

As for the future — aside from the list of reasons in sec. 1.4.1 — the next emphasis in terms of applications would be a more detailed investigation of individual reaction rates. In terms of further development, the emphasis would be on creating the first self-consistent superburst model and creating a more complete model of supernova fallback. In terms of extending the code, the emphasis would be to couple it with a more realistic treatment of the accretion process and the atmosphere.

The road to Ithaka...

The final burst code is mixture of different source codes, which have been collected from a large amount of people, thus allowing me to savor the very diverse styles of programming in the physics community. First and foremost I thank Matthias Liebendörfer for AGILE (hydrocode) and answering a lot of questions during the early stages. The initial idea of solving for the shift vectors was also his idea. I thank Raph Hix for handing over his well documented and efficient reaction network, which finally made me scrap my own. The EOS was also from Raph, but originally belonged to Ken Nomoto. I thank Ed Brown for his hospitality during my visit at U. of Chicago and for making the interface for the core boundary code and otherwise keeping me supplied with luminosity tables. I thank my “XRB-predecessor”, Felix Rembges, for general discussions during the early stages including a collaboration on my first XRB-paper. I thank Ulrich Geppert (and Pawel Haensel and Julian Zdunik) for help on understanding the crust/core behavior.

Discussions are sometimes helpful in reaching a true understanding of the problem and possibly even in reaching a solution and my supervisor Friedel Thielemann with his broad knowledge has been very helpful in that regard and also in breaking new frontiers into the physics community, in particular to Hendrik Schatz, whom I also thank for a great stay at NSCL/MSU and for discussions on double peaked bursts and the burst physics.

Occasionally “research” can be frustrating, so it is nice to be able to lament this fact together with fellow suffering roomies: Darko, Roland, and Carla, who also did the proofreading.

Finally I would like to thank everyone, who has read this far.

Appendix A

The computational model

The limits of a numerical model is due to the ignorance or the exclusion of the physical aspects. Physics is not the search for truth but for calculatability or in this case computability. While it would not pose too much of a problem to formulate the equations required to describe the X-ray burst, a complete solution would be very difficult – therefore reducing the problem to a tractable or solvable one by the right approximations is the biggest challenge facing the computational physicist – thus the field currently seems to be more driven by the affordable amount of computing power and the sophistication of the numerical technique rather than revolutionary ideas.

Units and notation: *To facilitate interdisciplinary reading and easy understanding all equations are given in cgs units and “natural” constants are not set to one. All quantities in this thesis are defined as being measured by a local observer, unless the variable is suffixed with a superscript e.g. R^∞ for the radius as measured by an observer at infinity. Conversion factors are given in Woosley et al. (2004).*

A.1 General discussion

Type I X-ray bursts occur in the atmosphere, which is bounded by the neutron star ocean and the photosphere, where the accretion shock converts the kinetic energy of the infalling material into heat. The photosphere is transparent to X-rays, so the heat is instantly radiated away, effectively decoupling the thermal response of the photosphere from the atmosphere (Joss (1978)), which only “sees” matter slowly advecting downwards from above. The heat of the burst is transported outwards to the photosphere and inwards to the ocean. However, in between bursts the heated layers cool again as heat is

transported outwards, thus layers lying sufficiently deep are never heated (Fujimoto et al. (1984)). Therefore they do not dynamically interact with the atmosphere, whence it is not necessary to include the deep layers of the ocean and the crust to describe the burst as long as they are described by a reasonable boundary condition.

Consequently only the atmosphere needs dynamical consideration¹. While the timescale of the nuclear runaway is measured in microseconds, the intervals between bursts can last hours or days. Therefore an implicit code is a prerequisite to self-consistently track the long intervals in between bursts, where the neutron star is accreting in a quiescent mode without using the computational resources for the tracking of very small timesteps required to keep an explicit solution stable. However, the implicit scheme requires an inversion of the Jacobian matrix connecting the independent variables of the system. The large number of variables makes the problem computationally intractable, whence the system must be decoupled into parts, which are individually implicitly treated, but as these different and individually implicit parts have a comparable timescales for the physically interesting problem, it is possible to couple and evolve them explicitly by using operator splitting (Henyey et al. (1959)).

A.2 Hydrodynamics

In a gravitationally dominated field the macroscopic motion of the matter is completely determined by the Einstein field equation(s), $G_{\mu\nu} = 8\pi T_{\mu\nu}$, where G is the Einstein curvature tensor and T is the stress-energy tensor. For the stress-energy tensor, we assume local thermal equilibrium (LTE), thereby neglecting viscous effects. Shear is also neglected, but heat transport is included. Assuming and imposing a spherically symmetric comoving metric as described by Misner & Sharp (1964) the general relativistic equivalent of the Euler equations have been derived in a conservative form and implemented in the code `AGILE` (Liebendörfer et al. (2002)).

A.2.1 Shift vector solution

To resolve the thin shells of the helium runaway (with typical masses of maybe $10^{-15} M_{\odot}$) while at the same time allowing the inclusion of very thick

¹Since all relevant times are longer than it takes a sound wave to cross a pressure scale height, many models also ignore hydrodynamical effects (Taam (1981, 1982); Ayasli & Joss (1982)).

shells (with typical masses of maybe up to $10^{-5}M_\odot$ or even more) for future studies of e.g. self-consistent superburst calculations, we have modified the discretization to handle zone variables differing over many orders or magnitude: Consider the discretization of the Poisson equation (eq. [50] of Liebendörfer et al. (2002)) which is repeated here for convenience

$$m_{i+1}^{t+\Delta t} - m_i^{t+\Delta t} = \Gamma_{i'}^{t+\Delta t} \left(1 + \frac{e_{i'}^{t+\Delta t}}{c^2} \right) da_{i'}^{t+\Delta t}, \quad (\text{A.1})$$

where $\Gamma_{i'}^{t+\Delta t} = \sqrt{1 + (u_i^{t+\Delta t}/c)^2 + 2Gm_i^{t+\Delta t}/r_i^{t+\Delta t}c^2}$, $e_{i'}^{t+\Delta t}$ is the internal energy of a zone, $m_i^{t+\Delta t}$ is the total gravitational mass inside the gravitational radius, $r_i^{t+\Delta t}$, and $da_{i'}^{t+\Delta t} = a_{i+1}^{t+\Delta t} - a_i^{t+\Delta t}$ is the rest mass of a zone. Variables with primed indices are defined on the center-grid while variables with unprimed indices are defined on the edge-grid. When **AGILE** is compiled with *double precision*, the numerics yields a maximum of 15 decimals of precision. This is insufficient to resolve the thin surface shells as noted above. An immediate problem is in the terms: $m_{i+1}^{t+\Delta t} - m_i^{t+\Delta t}$ and $da_{i'}^{t+\Delta t} = a_{i+1}^{t+\Delta t} - a_i^{t+\Delta t}$, where two large numbers are subtracted giving a number which is smaller by several orders of magnitude. This is more easily seen in from the commonly occurring expression, $r_{i+1}^{t+\Delta t} - r_i^{t+\Delta t}$, where r at the surface may be on the order of 10^6 cm, while the difference i.e. the zone width, is only a few cm. Therefore the original discretization of **AGILE** is not suitable for a simultaneous inclusion of both thin and thick shells, as the numerical scheme has to compensate by being extremely accurate, and even then this can not reclaim the precision already lost in the differencing.

Now consider the shift vectors, aptly named $\Delta a_i^{t+d\Delta t}$, $\Delta m_i^{t+\Delta t}$, and $\Delta r_i^{t+\Delta t}$, so that

$$m_i^{t+\Delta t} \equiv m_i^t + \Delta m_i^{t+\Delta t} \quad (\text{A.2})$$

$$r_i^{t+\Delta t} \equiv r_i^t + \Delta r_i^{t+\Delta t} \quad (\text{A.3})$$

$$da_i^{t+\Delta t} \equiv da_i^t + \Delta da_{i+1}^{t+\Delta t} - \Delta da_i^{t+\Delta t} \quad (\text{A.4})$$

Substituting these into eq. [A.1] yields

$$(m_{i+1}^t - m_i^t) + (\Delta m_{i+1}^{t+\Delta t} - \Delta m_i^{t+\Delta t}) = \Gamma_{i'} \left(1 + \frac{e_{i'}}{c^2} \right) (da_i^t + \Delta a_{i+1}^{t+\Delta t} - \Delta a_i^{t+\Delta t}). \quad (\text{A.5})$$

In general $m_i \gg \Delta m_i$, etc. is required. In calculating a time step m_i^t is constant, so $(m_{i+1}^t - m_i^t)$ of eq. [A.5] will be a small *constant* number comparable to $\Delta m_i^{t+\Delta t}$ which then becomes the new independent variable. Now realize that the precision which was lost in the differencing is reclaimed. There is a

precision loss with a magnitude of $\sim \log(m_i/m_{i+1} - 1)$ but that is very small compared to the precision loss of the original discretization.

In **AGILE** a_i is an independent variable, but by using $da_i^{t+\Delta t} = da_i^t + \Delta da_{i+1}^{t+\Delta t} - \Delta da_i^{t+\Delta t}$ accretion is easily included by setting $\Delta da_i^{t+\Delta t} = \dot{A} dt$ for all i . Then the zone masses will remain constant within a numerical uncertainty which is relative to each individual zone mass rather than being relative to a large number (e.g. $\max(a_i)$) as would be the case of eq. [A.1].

This does include numerical diffusion of the composition. The magnitude of this diffusion depends on the number of iterations per time (i.e. the size of the timestep) and the accretion rate, \dot{A} , and is very roughly given by

$$\left(1 - \frac{\Delta t \dot{A}}{da_i} \frac{x_i - 1}{x_i}\right)^{t/\Delta t}, \quad (\text{A.6})$$

where Δt is the size of a timestep and t is the integrated amount of timesteps.

The Einstein equations are complete by substituting eqs. A.2–A.4 into the original equations of Liebendörfer et al. (2002) and arranging the numerical differencing such that large terms of the previous timestep (e.g. m_i^t) are always subtracted before adding the difference of the corrective terms (e.g. $\Delta m_i^{t+\Delta t}$).

A.2.2 Adaptive grid modification

AGILE uses a modification of the **SAGE** adaptive grid of Dorfi & Drury (1987). We have rewritten the adaptive grid in **AGILE** to accommodate the use of shift vectors, which were necessary to maintain the equations describing the extreme variable ranges. The new generalizable adaptive grid has been optimized for the XRB scenario but it could be made shock capturing if desired.

Let $N_i = \Delta a_i$ be the mass of zone i , and $n_i = a_i^{t+\Delta t} - a_{i-1}^{t+\Delta t}$ be the mass, which is advected into zone i , during a time step Δt . Both variables have the units of mass/zone. Let k be a constant and introduce the logarithmic series $X_i = k^i$ and let $\hat{N}_i = N_i/X_i$ and $\hat{n}_i = n_i/X_i$. If the grid equation, which will be derived shortly, maintains this constant value by solving for the shift vectors, the mass zones will be logarithmically distributed with this particular choice of X_i .

In order to generalize the grid equation and make it dependent on other variables e.g. the velocity to make it shock capturing, we introduce the desired resolution

$$R_i^{grid} = \sqrt{1 + \sum_j \left(w_j \frac{N_{scale} f_i^j - f_{i-1}^j}{F_{scale}^j N_i} \right)^2}, \quad (\text{A.7})$$

where the sum is over all other independent variables, w_j is a weight factor, which determines the significance of the given variable, N_{scale} and F_{scale}^j are overall scales for the independent variables, and f_i^j is the value of the variable j at grid point i . One is free to choose a different expression for R_i^{grid} and the code currently uses $R_i^{grid} = 1$.

Normalize R^{grid} and introduce a similarly normalized

$$R_i^{current} = N_i / \hat{N}_i, \quad (\text{A.8})$$

which describes the current resolution.

The requirement for an initial relaxation onto the adaptive grid can be avoided by modifying the desired resolution R^{grid} to include a fraction of the current resolution such that

$$R_i = (1 - sloth)R_i^{grid} + R_i^{current}sloth, \quad (\text{A.9})$$

where *sloth* determines how the resolutions are mixed. In the XRB code we use $sloth = \exp(-dt/0.1)$, where dt is the time step and 0.1 is a selected parameter. This ensures that in cases of long time steps, the desired resolution will determine how the grid moves, whereas short time steps will maintain the current grid spacing.

Finally the adaptive grid equation, which is solved implicitly with the hydrodynamics, becomes

$$\left(\hat{N}_i R_i - \hat{N}_{i-1} R_{i-1} \right) + (\hat{n}_i R_i - \hat{n}_{i-1} R_{i-1}) = 0. \quad (\text{A.10})$$

This formulation avoids numerical singularities in the Jacobian matrix. The first parenthesis contains constant (big) terms, while the second parenthesis determines how the grid points have to be moved. If the terms of the first parenthesis nearly cancel then the current resolution is nearly equal to the desired resolution, and the grid points will hardly move. Additionally any movement will be close to numerically random and unimportant. As a consequence this formulation will not be numerically ill-conditioned, unless the relative grid changes are greater than the full precision of the variables (e.g. 15-16 orders of magnitude for *double precision*)! In its present incarnation the grid equation will maintain a logarithmic profile of the mass zones and thus advect accreted mass downwards.

A.3 Boundary conditions

The juxtaposed grids of Liebendörfer et al. (2002) require different boundary conditions. In general von Neumann boundary conditions are used where the

variable has a ghost zone and Dirichlet boundary conditions are used, where there are no ghost zones. The temperature and density of the inner boundary are thus left roaming and are determined by eq. [A.30] together with the outer boundary condition and a luminosity which is due to thermonuclear and compressional heat generation in the model minus neutrino heat losses and pycnonuclear energy generation, which enters as a source in the deepest zone. The radius and gravitational mass are given as hard inner boundary conditions. The lapse time is also roaming and determined by a gradient.

A.3.1 The outer boundary

The outer boundary condition for the lapse function (von Neumann: gradient is set to zero) and the redshift (Dirichlet: set to match the Schwarzschild solution) are as in Liebendörfer et al. (2002). The accretion is handled by

$$\Delta da_{ng}^{t+\Delta t} = \dot{A}\Delta t. \quad (\text{A.11})$$

This automatically advects the correct amount of matter at zero (Lagrangian) velocity and identical temperature into the outermost zone – the advection between the other zones is accounted for by eq. [A.10]. In addition the temperature and density are now determined by a radiative zero boundary condition or a so-called grey atmosphere.

A.3.2 The grey photosphere

An accurate description of the photosphere involves radiation transport and the interaction with the accreting matter and is very difficult to implement. We therefore neglect these interactions and opt for a crude description using a radiative zero photosphere, which yields a rough description of the bolometric luminosity (Joss et al. (1973); Kippenhahn & Weigert (1994)). Here we derive a new relativistically corrected version of this atmosphere model.

Assuming hydrostatic equilibrium, the temperature and pressure of the neutron star is described by Glen & Sutherland (1980)

$$\frac{\partial P}{\partial r} = \frac{-G(m + 4\pi r^3 P/c^2)(\rho + P/c^2)}{r^2 \left(1 - \frac{2Gm}{c^2 r}\right)}, \quad (\text{A.12})$$

where P is the pressure, r is the radius, G is the gravitational constant, m is the gravitational mass, c is the speed of light and ρ is the density of the rest mass.

$$\frac{d}{dr} (Te^\phi) = \frac{-3\kappa\rho L_\gamma e^\phi}{16\pi acT^3 r^2 \sqrt{1 - \frac{2Gm}{c^2 r}}}, \quad (\text{A.13})$$

where T is the temperature, e^ϕ is the red shift correction factor, κ is the opacity, L_γ is the photon luminosity and a is the radiation constant. As the energy density of the pressure is low in the photosphere compared to the rest mass energy density the Tolman-Oppenheimer-Volkoff equation simplifies to

$$\frac{\partial P}{\partial r} = \frac{-Gm\rho}{r^2 \left(1 - \frac{2Gm}{c^2 r}\right)}. \quad (\text{A.14})$$

Likewise the gravitational field may be assumed to be constant over the width of the photosphere, thus e^ϕ is constant and can be divided out, so

$$\frac{\partial T}{\partial r} = \frac{-3\kappa\rho L_\gamma}{16\pi acT^3 r^2 \sqrt{1 - \frac{2Gm}{c^2 r}}}. \quad (\text{A.15})$$

Resulting in

$$\frac{\partial P}{\partial T} = \frac{16\pi GacmT^3}{3\kappa L_\gamma \sqrt{1 - \frac{2Gm}{c^2 r}}}. \quad (\text{A.16})$$

Now assuming that the opacity remains constant and that the release of nuclear energy is effectively zero, the luminosity will be constant and the equation can be integrated from the naive zero boundary conditions (viz. $P = 0$ and $T = 0$) so that

$$\int_0^{P_{surf}} dP = \int_0^{T_{surf}} \frac{4\pi Gacm}{3\kappa L_\gamma \sqrt{1 - \frac{2Gm}{c^2 r}}} dT^4 \quad (\text{A.17})$$

or

$$P_{surf} = \frac{4\pi GacmT_{surf}^4}{3\kappa L_\gamma \sqrt{1 - \frac{2Gm}{c^2 r}}}. \quad (\text{A.18})$$

The outer boundary is defined by $P_{surf} := 5.1 \cdot 10^{20} \text{ dyn cm}^{-2}$ and eq. [A.18] is discretized as

$$P_{surf} = \frac{4\pi Gacm_{nq}T_{nq}^4}{3\kappa_{nq}L_{\gamma,nq-1} \sqrt{1 - \frac{2Gm_{nq}}{c^2 r_{nq}}}}, \quad (\text{A.19})$$

where it is necessary to use $L_{\gamma,nq-1}$ because L_{nq} is undefined and consequently

$$L_{nq} = L_{\gamma,nq-1}, \quad (\text{A.20})$$

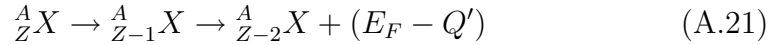
where nq refers to the outermost zone in the discretization and $nq - 1$ to the second outermost zone. This model atmosphere sacrifices accuracy of T_{surf} for accuracy of the heat transport, which is important, because it defines the observable light curve, whereas the T_{surf} only defines the rate of the nuclear reactions before the accreted matter is advected into the next zone.

Possible improvements

Several authors have noted that peak luminosity reaches the Eddington limiting luminosity of the neutron star atmosphere. This violates the assumptions of the radiative zero boundary condition requiring a sophisticated replacement employing wind and transport equations.

A.3.3 The ocean

Eventually ashes are advected into the ocean and subsequently the crust. Increasing the density the Fermi energy, E_F , of the electrons eventually exceeds the Q -value of electron capture for a given isotope at which point an electron capture will happen releasing $E_F - Q = 0$ energy. Now, if the electron capture Q' -value of the resulting nuclei is lower than E_F another reaction occurs releasing an energy of $E_F - Q' > 0$.



Further increases in density allows energy releasing pycnonuclear reactions and subsequent electron captures to occur, where the end result is a chemical equilibrium composed of neutrons and a few electrons and protons.

Using a static approximation Haensel & Zdunik (1990) calculated the rate of energy release based on a pure iron ashes and got 1.45MeV/nucleon. Recently these authors repeated their calculation for the distribution composition of Schatz et al. (1999) and got the same value (Haensel & Zdunik (2003)).

This energy is transported outwards or inwards depending on the temperature gradient, which depends on the opacities, the temperature, and the type of neutrino emissions of the neutron star core (Fujimoto et al. (1984)).

Since the ocean does not thermally interact with any one burst, the energy release of the electron captures and pycnonuclear reactions can be treated as a non-dynamical boundary condition. Here we use the code of Brown (2000, 2003) to calculate the thermal luminosity of the crust given the temperature, which is calculated by the dynamical model, at the atmosphere-ocean interface.

A.4 Opacities and conductance

Throughout the model the mean free path of photons and electrons is very short and many collisions occur traversing a zone width. Therefore electrons and photons are in LTE and heat transport follows Fourier's law and Fick's

law respectively. Heat conduction can be included alongside with radiation in Fick's law by defining a conductive opacity (Yakovlev & Urpin (1980); Kippenhahn & Weigert (1994))

$$\kappa = \frac{4acT^2 m_*}{\pi k_B^2 \rho n_e} \nu_c, \quad (\text{A.22})$$

where $E_F = (m_* - m_e)c^2$ and $\nu_c = \nu_{ee} + \nu_{ei}$ is the collision frequency due to electron interactions with other electrons or ions. The “radiative” opacity is then given by the harmonic sum of the total opacity due to radiation and conductivity respectively.

Using the total opacity it is possible to derive the temperature gradient of a model without convection (Thorne (1977))

$$\nabla_{rad.} = \underbrace{\frac{3}{16\pi} \frac{\kappa L P m}{G a c T^4}}_{\nabla_{classical-rad.}} \left[\frac{(1 + 4\pi r^3 P / (m c^2))}{H \sqrt{1 - \frac{2Gm}{c^2 r}}} + \left(1 - \frac{1 + e/c^2}{H}\right) \right]. \quad (\text{A.23})$$

Here κ is the opacity, L is the luminosity, c is the speed of light, G is the gravitational constant, $a = 7.565914 \times 10^{-15} \text{ erg cm}^{-3} \text{ K}^{-4}$ is the radiation density constant, T is the temperature, r is the radius, and m is the gravitational mass inside a sphere with a radius r , P is the pressure, ρ is the density, e is the specific internal energy, $H = 1 + e/c^2 + P/\rho c^2$ is the enthalpy correction factor, and the “rad” subscript indicates the gradient, which would be obtained if all heat was transported by radiation. The square bracket contains the relativistic corrections to the classical formula of e.g. Kippenhahn & Weigert (1994). This gradient is directly proportional to the opacity of the matter which depends on the composition and the temperature and density. Therefore it is important to know the opacity accurately as it indirectly determines the relation between density and temperature in the stellar profile and thus the conditions for the thermonuclear ignition and subsequent runaway (Rakavy & Shaviv (1967)).

The most important contribution to the opacity in the upper atmosphere is electron scattering and free-free absorption. In deeper layers where the accreted matter ignites, the matter is degenerate and electron conductivity dominates. The electron conductivity is described by electron-electron- and electron-ion scattering. In yet deeper layers electrons interacting with phonons and impurities become important but we do not consider these layers in our model. In calculating the contributions from free-free absorption we adopt the fitting formulas of Schatz et al. (1999) to Itoh et al. (1990). For electron-ion scattering, we use the Schatz et al. (1999) generalization of

the results of Yakovlev & Urpin (1980). For electron-electron scattering we adopt the expression given in Potekhin et al. (1997).

Electron scattering is very important in the upper atmosphere and directly enters into the boundary condition defining the Eddington limiting luminosity. Here we generalize the approximation, which Paczyński (1983a) used for a pure $Z/A = 2$ (e.g. Helium) composition, to an arbitrary composition so that

$$\kappa = \kappa_0 / (1.0 + 2.7 \times 10^{11} \rho / T^2) / (1.0 + (T / 4.5 \times 10^8)^{0.86}), \quad (\text{A.24})$$

where

$$\kappa_0 = \frac{8\pi}{3} \left(\frac{e^2}{m_e c^2} \right)^2 \frac{1}{m_u} \sum_i \frac{Z_i}{A_i} X_i \quad (\text{A.25})$$

is the average Thomson scattering cross section for a given composition assuming fully ionized matter. Here ρ is the mass density, T is the temperature, m_e is the electron mass, m_u is the unit mass, e is the electron charge, c is the speed of light, and A_i , Z_i , and X_i , are the nucleon number, proton number and nucleon fraction respectively with $\sum X_i = 1$.

A.5 Convection

The assumption of spherical symmetry rules out any form of hydrodynamical convection, since convection is inherently a multi-dimensional phenomena. Therefore convection is included phenomenologically using Böhm-Vitense's stellar adaption of Prandtl's mixing length theory (MLT) (Cox & Guili (1968)).

Formally, the condition for stability against convection for a bubble of matter is given by the Schwarzschild-Ledoux criterium which also holds relativistically, because it is a local criterium (Thorne (1966))

$$\left(\frac{d \ln T}{d \ln P} \right)_* \leq \left(\frac{d \ln T}{d \ln P} \right)_{bubble} - \sum_{x \in \{Y_e, Y_e^2, \dots\}} \frac{\chi_x}{\chi_T} \left(\frac{d \ln x}{d \ln P} \right)_*, \quad (\text{A.26})$$

assuming that $(\epsilon_{nuc} - \epsilon_{cool})_{bubble} \approx 0$ so that $(d \ln T) / (d \ln P)_{bubble} \approx (d \ln T) / (d \ln P)_{ad.} \equiv (\Gamma_2 - 1) / \Gamma_2$ Cox & Guili (1968). The sum over the moments of composition of the equation of state (EOS) accounts for compositional gradients in the stellar environment and $\chi_x \equiv \left(\frac{\partial \ln P}{\partial \ln x} \right)_{\{\dots\} \setminus x}$, where x may be any state-variable of the EOS, and the *other* state-variables are fixed.

A thermonuclear runaway rapidly creates a very steep temperature gradient exceeding the adiabatic gradient thus violating eq. [A.26]. This causes

convective bubbles to form and rise until they dissolve after travelling a *mixing length*, Λ , and release heat. This heat transport tends to decrease the steepness of the gradient that caused it in the first place. Thus the inequality of eq. [A.26] turns into an equality and convective motion ceases.

The convective heat flux is given by (Cox & Guili (1968))

$$F_c = \frac{1}{2}\rho \langle v \rangle c_p \Lambda \left(-\frac{dT}{dr} \Big|_{\star} + \frac{dT}{dr} \Big|_{ad.} \right), \quad (\text{A.27})$$

where c_p is the specific heat capacity of the bubble and $\langle v \rangle$ is the average velocity of rising/descending bubble given by

$$\langle v \rangle^2 = \frac{1}{8}gQ\frac{\rho}{P}\Lambda(\nabla_{\star} - \nabla_{ad.}), \quad (\text{A.28})$$

where g is the acceleration of the gravitational field and

$$-Q \equiv \sum_{x \in \{Y_e, Y_e^2, \dots\}} \left(\frac{\partial \ln \rho}{\partial \ln x} \right)_{P, T, \dots} \left(\frac{\partial \ln x}{\partial \ln T} \right)_{P, \dots} + \left(\frac{\partial \ln \rho}{\partial \ln T} \right)_{P, Y_e, Y_e^2, \dots} \quad (\text{A.29})$$

Heat transport may be incorporated in the radiative gradient (eq. [A.23]) by augmenting $\nabla_{classical-rad.}$ such that (Cox & Guili (1968); Thorne (1977))

$$\nabla_{classical-rad.} := \nabla_{classical-rad.} + \frac{3c_p \kappa \sqrt{Q\rho^5} g \Lambda^2}{16\sqrt{2}ac\sqrt{PT^3}} (\nabla_{\star} - \nabla_{ad.})^{3/2}, \quad (\text{A.30})$$

Convective mixing is described by a time-dependent diffusion equation using the same method as Wallace et al. (1982) and Woosley et al. (2004) except that secular convection such as semiconvection is not included, because it is not important during the short time timescales of the bursts considered in this work, and because the diffusion speed is lower than the advection speed (Bildsten et al. (1993)).

A.5.1 Shortcomings of mixing length theory

There are at least two fundamental problems of applying MLT to the XRB application. The first problem is that the mixing length, Λ , is not known ab initio, but in the non-degenerate regime, where MLT has proved to be highly successful, it is reasonable to say that Λ is on the order of the pressure scale height, since bubbles will expand and diffuse into each other and dissolve after travelling about such a distance (see e.g. Shu (1991)). In the degenerate regime of the neutron star atmosphere the pressure scale height is around 5-10 meters which is much higher than the height of the convective

zone. This violates the most basic assumption of MLT, since the size of the convective turnover ($\equiv \Lambda$) obviously can not be bigger than the convective zone itself! Therefore Λ has been reset to a fixed length of 1 cm in this study. The second problem is that MLT was developed for hydrostatic atmospheres and assumes that heat transporting turbulence is either on or off depending on the violation of eq. [A.26], whereas in a dynamical situation the turbulent field develops or decays over a period of time comparable to the runaway timescale. Therefore a time-dependent theory might give quantitatively different results (Wuchterl & Feuchtinger (1998)). Despite the shortcomings of MLT for the XRB simulation we implement it, because no other general relativistic implementations currently exists (Fryer et al. (1996)). In addition we have performed simulations where convective heat transport was set to zero. These runs did not qualitatively change the reaction flows which are the main conclusions of this work, so we leave the implementation of a more advanced time-dependent convection theory (e.g. Kuhfuss (1986)) for future work.

A.6 Equation of state

Type I X-ray bursts occur in the upper atmosphere, where accreted atoms are assumed to be fully ionized. The abundance of the electrons is determined by the composition. Their contribution to the pressure and the internal energy is calculated by assuming an arbitrarily relativistic and arbitrarily degenerate gas. The baryon contribution is described as an ideal gas to a good approximation. Photons are assumed to be in LTE, because the mean free path is short, and the photon partial pressure is given by $P_\gamma = a_{rad} T^4/3$.

These things are all contained in K. Nomoto's EOS code, which we adopted for this study, because it is fast and returns continuous and differentiable variables. This was necessary for eq. [A.26] and eq. [A.29] in our implementation of the the MLT. If an EOS is not differentiable, at least to a first order, and very fast, it is generally and regretfully useless.

A.7 Neutrino bremsstrahlung

The fraction of energy lost via neutrino emission due to bremsstrahlung is insignificant in the burst region, but we include it for completeness. The loss from pair ($e^+ + e^- \rightarrow \nu_{e,\mu,\tau} + \bar{\nu}_{e,\mu,\tau}$), photo ($e^\pm + \gamma \rightarrow e^\pm + \nu_{e,\mu,\tau} + \bar{\nu}_{e,\mu,\tau}$), and plasma (plasmon $\rightarrow \nu_{e,\mu,\tau} + \bar{\nu}_{e,\mu,\tau}$) neutrino emission are all calculated using the formulations of Schinder et al. (1987).

A.8 Reaction network

We describe the *rp*-process and its resulting ashes using a generalized reaction network incorporating the reaction equations in the form of Hix & Thielemann (1999)

$$\begin{aligned} \frac{dY_i}{dt} = & \sum_j N_j^i \lambda_j Y_j + \sum_{j,k} N_{j,k}^i \rho N_A \langle \sigma v \rangle_{j,k} Y_j Y_k \\ & + \sum_{j,k,l} N_{j,k,l}^i \rho^2 N_A^2 \langle \sigma v \rangle_{j,k,l} Y_j Y_k Y_l, \end{aligned} \quad (\text{A.31})$$

where Y_i is the nuclear abundance of isotope i defined as $Y_i = X_i/A_i$, where A_i is the nucleon number and X_i is the fraction of the total number of all nucleons which is found the form of isotope i ; we also have $\sum_i X_i = 1$.

The network includes photodisintegration, β -decays and electron-, neutron²-, proton- and α -captures. The transmutation results in an overall change of binding energy and composition of the matter. The energy difference is partially due to neutrino emissions or heat, which is either absorbed or released from the matter.

$$\epsilon_{nuc} = -N_A \sum Q_i \dot{Y}_i + \sum \langle E_\nu \rangle_j \dot{Y}_{j,\text{weak}}, \quad (\text{A.32})$$

where Q_i is the Q -value of the i th reaction in erg units. N_A is Avogadro's constant, $\langle E_\nu \rangle_j$ is the energy loss from the neutrino emission due to the j th weak interaction.

Neutrino loss is included in the weak rates below $Z=32$ and ignored above as in Schatz et al. (1999). This is a reasonable approximation, since only a small fraction of material is processed above $Z = 32$. We use the weak rates of Fuller et al. (1980, 1982a,b); Langanke & Martínez-Pinedo (2001) where available. The particle reaction rates are taken from Schatz (2003) where the rates of Fisker et al. (2001a) was substituted in.

²Neutron induced reactions can be generally be neglected yielding several factors of increase of computational speed.

Z	A	Z	A
n	1	Co	51–57
H	1–3	Ni	52–62
He	3–4	Cu	54–63
Li	7	Zn	55–66
Be	7	Ga	59–67
B	8	Ge	60–68
C	12	As	64–69
N	13–15	Se	65–72
O	14–18	Br	68–73
F	17–19	Kr	69–74
Ne	18–21	Rb	73–77
Na	20–23	Sr	74–78
Mg	21–25	Y	77–82
Al	22–27	Zr	78–83
Si	24–30	Nb	81–85
P	26–31	Mo	82–86
S	27–34	Tc	85–88
Cl	30–35	Ru	86–91
Ar	31–38	Rh	89–93
K	35–39	Pd	90–94
Ca	36–44	Ag	94–98
Sc	39–45	Cd	95–99
Ti	40–47	In	98–104
V	43–45	Sn	99–105
Cr	44–52	Sb	106
Mn	47–53	Te	107
Fe	48–56		

Figure A.1: The list of isotopes incorporated in the network calculations. Since the focus was to describe the reaction flow of the *rp*-process, the reactions between the light nuclei i.e. *pp*-chains have been simplified (Wiescher et al. (1989)).

Bibliography

- Anders, E., & Grevesse, M. 1989, *Geochim. Cosmochim. Acta*, 53, 197
- Asai, K., Dotani, T., Nagase, F., & Mitsuda, K. 2000, *Astrophys. J. Suppl.*, 131, 571
- Audouze, J., Truran, J. W., & Zimmerman, B. A. 1973, *Astrophys. J.*, 184, 493
- Ayasli, S., & Joss, P. C. 1982, *Astrophys. J.*, 256, 637
- Bautista, M. A., Kallman, T. R., & Angelini, L. 1998, *Astrophys. J.*, 509, 848
- Belian, R. D., Conner, J. P., & Evans, W. D. 1976, *Astrophys. J. Lett.*, 206, L135
- Bildsten, L. 1993, *Astrophys. J.*, 418, L21
- . 1995, *Astrophys. J.*, 438, 852
- . 1998a, *Astrophys. J. Lett.*, 501, L89
- Bildsten, L. 1998b, in *The Many Faces of Neutron Stars*, ed. R. Buccheri, J. van Paradijs, & M. A. Alpar (Kluwer), 419
- Bildsten, L. 2000, in *Cosmic Explosions*, ed. S. S. Holt & W. W. Zhang (AIP), 359
- Bildsten, L., & Brown, E. F. 1997, *Astrophys. J.*, 477, 897
- Bildsten, L., & Cumming, A. 1998, *Astrophys. J.*, 506, 842
- Bildsten, L., & Cutler, C. 1995, *Astrophys. J.*, 449, 800
- Bildsten, L., Salpeter, E. E., & Wasserman, I. 1992, *Astrophys. J.*, 384, 143

- . 1993, *Astrophys. J.*, 408, 615
- Brown, B. A., Clement, R. R. C., Richter, W. A., Schatz, H., & Volya, A. 2002, Proton Drip-Line Calculations and the rp-Process, astro-ph/0202103
- Brown, E. F. 2000, *Astrophys. J.*, 531, 988
- . 2003, Core code, private communication
- Brown, E. F., & Bildsten, L. 1998, *Astrophys. J.*, 496, 915
- Brown, E. F., Bildsten, L., & Rutledge, R. E. 1998, *Astrophys. J.*, 504, L95
- Caughlan, G. R., & Fowler, W. A. 1988, *At. Data Nucl. Data Tables*, 40, 283
- Champagne, A. E., & Wiescher, M. 1992, *Ann. Rev. Nucl. Part. Sci.*, 42, 39
- Cornelisse, R., Kuulkers, E., J. J. M. In't Zand, Verbunt, F., & Heise, J. 2002, *Astron. Astrophys.*, 382, 174
- Cottam, J., Paerels, F., & Mendez, M. 2002, *Nature*, 420, 51
- Cox, J., & Guili, R. 1968, *Principles of Stellar Structure Vol. 1,2* (New York: Gordon and Breach, Science Publishers)
- Cumming, A. 2003, Thermonuclear X-ray bursts: Theory vs. Observations, astro-ph/0309626
- Cumming, A., & Bildsten, L. 2000, *Astrophys. J. Lett.*, 544, 453
- . 2001, *Astrophys. J. Lett.*, 559, L127
- Davids, B., van den Berg, A. M., Dendooven, P., Fleurot, F., Hunyadi, M., de Huu, M. A., Siemssen, R. H., Hernanz, M., José, J., Rehm, K. E., & Wuosmaa, A. H. 2003, *Phys. Rev.*, C67, 065808
- Dorfi, E. A., & Drury, L. O. 1987, *J. Comput. Phys.*, 69, 175
- Ergma, E. V., & Tutukov, A. V. 1980, *Astron. Astrophys.*, 84, 123
- Fisker, J. L., Barnard, V., Görres, J., Langanke, K., Martínez-Pinedo, G., & Wiescher, M. C. 2001a, *At. Data Nucl. Data Tables*, 79, 241
- Fisker, J. L., Hix, W. R., Liebendörfer, M., & Thielemann, F.-K. 2003, *Nucl. Phys.*, A718, 614

- Fisker, J. L., Rembges, F., Barnard, V., & Wiescher, M. C. 2001b, in *The influence of binaries on stellar population studies*, ed. D. van Beveren (Kluwer Academic Publishers), 569
- Fisker, J. L., Thielemann, F.-K., & Wiescher, M. 2004, *Astrophys. J. Lett.*, 608, L61
- Fowler, W. A., Caghlan, G. R., & Zimmerman, B. A. 1967, *Ann. Rev. Astron. Astrophys.*, 5, 525
- . 1975, *Ann. Rev. Astron. Astrophys.*, 13, 69
- Fryer, C. L., Benz, W., & Herant, M. 1996, *Astrophys. J.*, 460, 801
- Fryxell, B. A., & Woosley, S. E. 1982a, *Astrophys. J.*, 261, 332
- . 1982b, *Astrophys. J.*, 258, 733
- Fujimoto, M. Y., Hanawa, T., Jr., I. I., & Richardson, M. B. 1987a, *Astrophys. J.*, 315, 198
- Fujimoto, M. Y., Hanawa, T., & Miyaji, S. 1981, *Astrophys. J.*, 246, 267
- . 1984, *Astrophys. J.*, 278, 813
- Fujimoto, M. Y., Sztajno, M., Lewin, W. H. G., & van Paradijs, J. 1987b, *Astrophys. J.*, 319, 902
- . 1988, *Astron. Astrophys.*, 199, L9
- Fuller, G. M., Fowler, W. A., & Newman, M. J. 1980, *Astrophys. J. Suppl.*, 42, 447
- . 1982a, *Astrophys. J.*, 252, 715
- . 1982b, *Astrophys. J. Suppl.*, 48, 279
- Fushiki, I., & Lamb, D. Q. 1987, *Astrophys. J.*, 323, L55
- Fushiki, I., Taam, R. E., Woosley, S. E., & Lamb, D. Q. 1992, *Astrophys. J.*, 390, 634
- Galloway, D. K., Cumming, A., Kuulkers, E., Bildsten, L., Chakrabarty, D., & Rotschild, R. E. 2004, *Astrophys. J.*, 601, 466
- Glen, G., & Sutherland, P. 1980, *Astrophys. J.*, 239, 671

- Görres, J., Wiescher, M., & Rolfs, C. 1989, *Astrophys. J.*, 3433, 365
- Gottwald, M., Haberl, F., Langmeier, A., Hasinger, G., Lewin, W. H. G., & van Paradijs, J. 1989, *Astrophys. J.*, 339, 1044
- Gottwald, M., Haberl, F., Parmar, A., & White, N. 1986, *Astrophys. J.*, 308, 213
- Grindlay, J. E., Gursky, H., Schnopper, H., Parsignault, D. R., Heise, J., Brinkman, A. C., & Schrijver, J. 1976, *Astrophys. J. Lett.*, 205, L127
- Groombridge, D., Shotton, A. C., Bradfield-Smith, W., Cherubini, S., Davinson, T., di Pietro, A., Görres, J., Graulich, J. S., Laird, A. M., Leleux, P., Musumarra, A., Ninane, A., Ostrowski, A. N., Rahigi, J., Schatz, H., Wiescher, M., & Woods, P. J. 2002, *Phys. Rev.*, C66, 055802
- Haensel, P., Kaminker, A. D., & Yakovlev, D. G. 1996, *Astron. Astrophys.*, 314, 328
- Haensel, P., Urpin, V. A., & Yakovlev, D. G. 1990, *Astron. Astrophys.*, 227, 133
- Haensel, P., & Zdunik, J. L. 1990, *Astron. Astrophys.*, 227, 431
- . 2003, *Astron. Astrophys.*, 404, L33
- Hanawa, T., & Fujimoto, M. Y. 1982, *Publ. Astron. Soc. Japan*, 34, 495
- . 1984, *Publ. Astron. Soc. Japan*, 36, 199
- Hanawa, T., & Sugimoto, D. 1983, *Publ. Astron. Soc. Japan*, 35, 491
- Hansen, C. J., & van Horn, H. M. 1975, *Astrophys. J.*, 195, 735
- Hasinger, G., & van der Klis, M. 1989, *Astron. Astrophys.*, 225, 79
- Hass, M. 2003, Hot p-p chains, private communication
- Heney, L. G., Wilets, L., Böhm, K. H., Lelevier, R., & Levee, R. D. 1959, *Astrophys. J.*, 129, 628
- Herndl, H., Jörres, Wiescher, M., Brown, B. A., & van Wormer, L. 1995, *Phys. Rev.*, C52, 1078
- Hix, W. R., Smith, M. S., Starrfield, S., Mezzacappa, A., & Smith, D. L. 2003, *Nucl. Phys.*, A718, 620

- Hix, W. R., & Thielemann, F.-K. 1999, *J. Comput. Appl. Math.*, 109, 321
- Iliadis, C., D'Auria, J. M., Starrfield, S., Thompson, W. J., & Wiescher, M. 2001, *Astrophys. J. Suppl.*, 134, 151
- Iliadis, C., Endt, P. M., Prantzos, N., & Thompson, W. J. 1999, *Astrophys. J.*, 524, 434
- Irion, R. 2002, *Science Magazine*, 297, 2199
- Itoh, N., Kojo, K., & Nakagawa, M. 1990, *Astrophys. J. Suppl.*, 74, 291
- Joss, P. C. 1977, *Nature*, 270, 310
- . 1978, *Astrophys. J. Lett.*, 225, L123
- Joss, P. C. 1981, in *IAU Symp. 93: Fundamental Problems in the Theory of Stellar Evolution*, 207–225
- Joss, P. C., & Li, F. K. 1980, *Astrophys. J.*, 238, 287
- Joss, P. C., Salpeter, E. E., & Ostriker, J. P. 1973, *Astrophys. J.*, 181, 429
- Kalogera, V. 1998, in *The Many Faces of Neutron Stars*, ed. R. Buccheri, J. van Paradijs, & M. A. Alpar (Kluwer), 505
- Kalogera, V., & Webbink, R. F. 1996, *Astrophys. J.*, 458, 301
- . 1998, *Astrophys. J.*, 493, 351
- Kippenhahn, R., & Weigert, A. 1994, *Stellar Structure and Evolution*, 3rd edn. (Berlin Heidelberg: Springer-Verlag)
- Koike, O., Hashimoto, M., Arai, K., & Wanajo, S. 1999, *Astron. Astrophys.*, 342, 464
- Kong, A. K. H., Homer, L., Kuulkers, E., Charles, P. A., & Smale, A. P. 2000, *Mon. Not. R. Astron. Soc.*, 311, 405
- Kuhfuss, R. 1986, *Astron. Astrophys.*, 160, 116
- Kuulkers, E. 2002, *Astron. Astrophys.*, 383, L5
- Kuulkers, E., Homan, J., van der Klis, M., Lewin, W. H. G., & Méndez, M. 2002, *Astron. Astrophys.*, 382, 947
- Lamb, D. Q. 2000, *Astrophys. J. Suppl.*, 127, 395

- Langanke, K., & Martínez-Pinedo, G. 2001, *Nucl. Phys.*, A673, 481
- Langmeier, A., Sztajno, M., Hasinger, G., & Trumper, J. 1987, *Astrophys. J.*, 323, 288
- Lapidus, I. I., & Sunyaev, R. A. 1985, *Mon. Not. R. Astron. Soc.*, 217, 291
- Lewin, W. H. G. 1977, *Mon. Not. R. Astron. Soc.*, 179, 43
- Lewin, W. H. G., Penninx, W., van Paradijs, J., Damen, E., Sztajno, M., Truemper, J., & van der Klis, M. 1987, *Astrophys. J.*, 319, 893
- Lewin, W. H. G., van Paradijs, J., & Taam, R. E. 1995, in *X-Ray Binaries*, ed. W. H. G. Lewin, J. van Paradijs, & E. van den Heuvel (Cambridge Univ. Press), 175
- Liebendörfer, M., Rosswog, S., & Thielemann, F.-K. 2002, *Astrophys. J. Suppl.*, 141, 229
- Liu, Q. Z., van Paradijs, J., & van den Heuvel, E. P. J. 2001, *Astron. Astrophys.*, 368, 1021
- London, R. A., Howard, W. M., & Taam, R. E. 1986, *Astrophys. J.*, 306, 170
- London, R. A., Taam, R. E., & Howard, W. M. 1984, *Astrophys. J.*, 287, L27
- Marshall, H. L. 1982, *Astrophys. J.*, 260, 815
- Melia, F., & Zylstra, G. J. 1992, *Astrophys. J.*, 398, 53
- Miller, M. C. 1999, *Astrophys. J. Lett.*, 515, L77
- Miralda-Escudé, J., Haensel, P., & Paczyński, B. 1990, *Astrophys. J.*, 362, 572
- Misner, C. W., & Sharp, D. H. 1964, *Phys. Rev.*, B136, 571
- Murakami, T., Inoue, H., Koyama, K., Makishima, K., Matsuoka, M., Oua, M., & Ogawara, Y. 1980, *Astrophys. J.*, 240, L143
- Nakamura, N., Dotani, T., Inour, H., Mitsuda, K., & Tanaka, Y. 1989, *Publ. Astron. Soc. Japan*, 41, 617
- Nomoto, K., Thielemann, F.-K., & Miyaji, S. 1985, *Astron. Astrophys.*, 149, 239

- Nozakura, T., Ikeuchi, S., & Fujimoto, M. Y. 1984, *Astrophys. J.*, 286, 221
- Paczynski, B. 1983a, *Astrophys. J.*, 267, 315
- . 1983b, *Astrophys. J.*, 264, 282
- Parmar, A. N., Oosterbroek, T., Boirin, L., & Lumb, D. 2002, *Astron. Astrophys.*, 386, 910
- Pedersen, H., van Paradijs, J., & Lewin, W. H. G. 1981, *Nature*, 294, 725
- Penninx, W., Damen, E., van Paradijs, J., & Lewin, W. H. G. 1989, *Astron. Astrophys.*, 208, 146
- Pethick, C. J., & Sahrling, M. 1995, *Astrophys. J. Lett.*, 453, L29
- Potekhin, A. Y., Chabrier, G., & Yakovlev, D. G. 1997, *Astron. Astrophys.*, 323, 415
- Prendergast, K. H., & Burbidge, G. R. 1968, *Astrophys. J. Lett.*, 151, L83
- Rakavy, G., & Shaviv, G. 1967, *Ap&SS*, 1, 347
- Rauscher, T., & Thielemann, F.-K. 2000, *At. Data Nucl. Data Tables*, 75, 1
- . 2001, *At. Data Nucl. Data Tables*, 79, 47
- Rauscher, T., Thielemann, F.-K., & Kratz, K.-L. 1997, *Nucl. Phys.*, A621, 331
- Regev, O., & Livio, M. 1984, *Astron. Astrophys.*, 134, 123
- Rembges, F. 1999, PhD thesis, University of Basel
- Rembges, F., Freiburghaus, C., Rauscher, T., Thielemann, F.-K., Schatz, H., & Wiescher, M. 1997, *Astrophys. J.*, 484, 412
- Schatz, H. 2002, *Acta. Phys. Pol. B*, 33, 227
- . 2003, REACLIB105, private communication
- Schatz, H., Aprahamian, A., Barnard, V., Bildsten, L., Cumming, A., Ouellette, M., Rauscher, T., Thielemann, F.-K., & Wiescher, M. 2001a, *Phys. Rev. Lett.*, 86, 3471
- . 2001b, *Nucl. Phys.*, A688, 150

- Schatz, H., Aprahamian, A., Görres, J., Wiescher, M., Rauscher, T., Rembges, J. F., Thielemann, F.-K., Pfeiffer, B., Möller, P., Kratz, K. L., Herndl, H., Brown, B. A., & Rebel, H. 1998, *Phys. Rev.*, 294, 167
- Schatz, H., Bildsten, L., & Cumming, A. 2003, *Astrophys. J.*, 583, L87
- Schatz, H., Bildsten, L., Cumming, A., & Wiescher, M. 1999, *Astrophys. J.*, 524, 1014
- Schinder, P. J., Schramm, D. N., Wiita, P. J., Magolis, S. H., & Tubbs, D. L. 1987, *Astrophys. J.*, 313, 531
- Seon, K.-I., & Min, K. W. 2002, *Astron. Astrophys.*, 395, 141
- Shannon, C. E., & Weaver, W. 1963, *Mathematical Theory of Communication* (Illinois: University of Illinois Press)
- Shapiro, S. L., & Teukolsky, S. A. 1983, *Black Holes, White Dwarfs, and Neutron Stars* (New York: John Wiley & Sons)
- Shara, M. M. 1982, *Astrophys. J.*, 261, 649
- Shu, F. 1991, *The physics of astrophysics* (Mill Valley, California: University Book Press)
- Spitkovsky, A., Levin, Y., & Ushomirsky, G. 2002, *Astrophys. J.*, 566, 1018
- Strohmayer, T. E., & Brown, E. F. 2002, *Astrophys. J.*, 566, 1045
- Strohmayer, T. E., Swank, J. H., & Zhang, W. 1998, *Nucl. Phys. B (Proc. Suppl.)*, 69, 129
- Swank, J. H., Becker, R. H., Boldy, E. A., Holt, S. S., Pravdgo, S. H., & Serlemitsos, P. J. 1977, *Astrophys. J. Lett.*, 212, L73
- Sztajno, M., Fujimoto, M. Y., van Paradijs, J., Vacca, W. D., Lewin, W. H. G., Penninx, W., & Trumper, J. 1987, *Mon. Not. R. Astron. Soc.*, 226, 39
- Sztajno, M., van Paradijs, J., Lewin, W. H. C., Trumper, J., Stollman, G., Pietsch, W., & van der Klis, M. 1985, *Astrophys. J.*, 299, 487
- Taam, R. E. 1980, *Astrophys. J.*, 241, 358
- . 1981, *Astrophys. J.*, 247, 257

- . 1982, *Astrophys. J.*, 258, 761
- . 1985, *Astrophys. J.*, 294, 303
- . 1993, *Astrophys. J.*, 413, 324
- Taam, R. E., & Picklum, R. E. 1979, *Astrophys. J.*, 233, 327
- Taam, R. E., Woosley, S. E., & Lamb, D. Q. 1996, *Astrophys. J.*, 459, 271
- Thielemann, F.-K., Kratz, K.-L., Pfeiffer, B., Rauscher, T., van Wormer, L., & Wiescher, M. C. 1994, *Nucl. Phys.*, A570, 329
- Thorne, K. S. 1966, *Astrophys. J.*, 144, 201
- . 1977, *Astrophys. J.*, 212, 825
- Ubertini, P., Bazzano, A., Cocchi, M., Natalucci, L., eise, J., Muller, J. M., & In't Zand, J. J. M. 1999, *Astrophys. J. Lett.*, 514, L27
- Urpin, V., & Geppert, U. 1995, *Mon. Not. R. Astron. Soc.*, 275, 1117
- Ushomirsky, G., Cutler, C., & Bildsten, L. 2000, *Mon. Not. R. Astron. Soc.*, 319, 902
- van den Heuvel, E. P. J. 1975, *Astrophys. J. Lett.*, 198, L109
- van der Klis, M., Hasinger, G., Damen, E., Penninx, W., van Paradijs, J., & Lewin, W. H. G. 1990, *Astrophys. J. Lett.*, 360, L19
- van Paradijs, J., Penninx, W., & Lewin, W. H. G. 1988, *Mon. Not. R. Astron. Soc.*, 233, 437
- van Paradijs, J., Sztajno, M., Lewin, W. H. G., Truemper, J., Vacca, W. D., & van der Klis, M. 1986, *Mon. Not. R. Astron. Soc.*, 221, 617
- van Wormer, L., Görres, J., Illiadis, C., Wiescher, M., & Thielemann, F.-K. 1994, *Astrophys. J.*, 423, 326
- Walker, M. A., & Mészáros, P. 1989, *Astrophys. J.*, 346, 844
- Wallace, R. K., & Woosley, S. E. 1981, *Astrophys. J. Suppl.*, 45, 389
- Wallace, R. K., Woosley, S. E., & Weaver, T. A. 1982, *Astrophys. J.*, 258, 696
- Wiescher, M. 2001, *Nucl. Phys.*, A688, 241

- Wiescher, M., Barnard, V., Fisker, J. L., Görres, J., Langanke, K., Martínez-Pinedo, G., Rembges, F., Schatz, H., & Thielemann, F.-K. 2002, *Eur. Phys. J.*, A15, 59
- Wiescher, M., & Görres, J. 1989, *Astrophys. J.*, 346, 1041
- Wiescher, M., Görres, J., Graff, S., Buchmann, L., & Thielemann, F.-K. 1989, *Astrophys. J.*, 343, 352
- Wiescher, M., Görres, J., & Schatz, H. 1999, *J. Phys G: Nucl. Phys.*, 25, R133
- Wiescher, M., Görres, J., Thielemann, F.-K., & Ritter, H. 1986, *Astron. Astrophys.*, 160, 56
- Wiescher, M., & Schatz, H. 2001, *Nucl. Phys.*, A693, 269
- Woosley, S. E., Fowler, W. A., Holmes, J. A., & Zimmermann, B. A. 1978, *At. Data Nucl. Data Tables*, 22, 371
- Woosley, S. E., Heger, A., Cumming, A., Hoffman, R. D., Pruet, J., Rauscher, T., Fisker, J. L., Schatz, H., Brown, B. A., & Wiescher, M. 2004, *Astrophys. J. Suppl.*, 151, 75
- Woosley, S. E., & Taam, R. E. 1976, *Nature*, 263, 101
- Wuchterl, G., & Feuchtinger, M. U. 1998, *Astron. Astrophys.*, 340, 419
- Yakovlev, D. G., & Urpin, V. A. 1980, *Sov. Astron.*, 24, 303
- Zingale, M., Timmes, F. X., Fryxell, B., Lamb, D. Q., Olson, K., Calder, A. C., Durse, L. J., Ricker, P., Rosner, R., MacNeice, P., & Turg, H. M. 2001, *Astrophys. J. Suppl.*, 133, 195

Curriculum Vitae: Jacob Lund Fisker

- Born: October 3rd 1975, Randers, Denmark
- Citizenship: Denmark

Education

- Cand.Scient in physics and mathematics (Jan/2000)
Department of Physics and Astronomy, University of Aarhus, Denmark
Large Scale Shell Model Calculations of The Forbidden β^+ Decays of ^{56}Ni and The Thermonuclear Reaction Rates in The rp -Process On Nuclei in The Intermediate Mass Range.
- Ph.D. in theoretical physics (Feb/2004)
Department of Physics and Astronomy, University of Basel, Switzerland
The reaction flow during explosive nuclear burning on an accreting neutron star.

Employment History

- University of Basel (2002-2004) System administrator for the theory group at the Institute of Physics.
- University of Basel (2000-2002) Teaching assistant in electrodynamics, nuclear physics, thermodynamics & statistical physics, and quantum mechanics.
- University of Aarhus (1999) Mentor for exchange students at the Institute of Physics and Astronomy.

Professional Experience

- University of Edinburgh, Edinburgh, Scotland, February 25th, 2004 (invited seminar)
- ISOLDE Physics Workshop and Users Meeting, CERN, Geneva, Switzerland, December 15th-17th, 2003 (invited talk)
- Graduiertenkolleg Workshop 2003, Blaubeuren, Germany, September 29th-October 2nd, 2003 (talk)

- NSCL, Michigan State University, Michigan, USA, September 19th, 2003 (nuclear theory group talk)
- Visiting the astrophysics group at the University of Chicago, Chicago, Illinois, USA, September 14th-18th, 2003 (astrophysics group talk)
- Surface Compositions of Accreting Neutron Stars, Joint Argonne National Laboratory and University of Chicago Workshop, Argonne National Laboratory, Argonne, Illinois, USA, September 12th-13th, 2003 (talk)
- University of Notre Dame, South Bend, Indiana, USA, August 25th, 2003 (seminar)
- Research visit – H. Schatz, NSCL, Michigan State University, East Lansing, Michigan, USA. (August-September 2003)
- Institut für Strahlenphysik der Universität Stuttgart, Stuttgart, Germany, July 24th, 2003 (colloquium)
- Neutron Stars On Fire, Institute for Advanced Studies, Princeton, New Jersey, USA, May 11th-13th, 2003 (talk).
- n_TOF Winter School on Astrophysics, ADS, and First Results, Ecole de Physique, Les Houches, France, February 24th-28th, 2003.
- Topical Workshop (ANS/DNP Fall Meeting): Nuclear Astrophysics at the Limits of Stability, East Lansing, Michigan, USA, October 9th, 2002.
- 1st Workshop of the Joint Institute for Nuclear Astrophysics, The r-process - new experimental, theoretical, and observational opportunities, Gull Lake, Michigan, USA, October 6th-8th, 2002.
- Nuclei In Cosmos 2002, Fuji-yoshida, Japan, July 7th - July 13th, 2002 (poster)
- 11th Workshop on “Nuclear Astrophysics”, Ringberg Castle, Lake Tegernsee, Germany, February 11th-16th, 2002.
- Graduiertenkolleg Workshop 2001, Blaubeuren, Germany, October 3rd-6th, 2001 (talk).
- NAP2001, GSI Darmstadt, Germany, May 3rd - 5th, 2001
- The influence of binaries on stellar population studies, Vrije Universiteit Brussel, Belgium, August 21th - 25th, 2000 (poster)
- 5th Nordic Summer School in Nuclear Physics, Hilleroed, Denmark, August 14th - 25th, 2000.

- Nuclei In Cosmos 2000, University of Aarhus, Denmark, June 27th - July 1st, 2000 (poster)
- Visiting the astrophysics group at the Institute of physics, University of Basel, Basel, Switzerland, December 2nd-5th, 1999 (astrophysics group talk)
- Research visit – M. Wiescher, Nuclear Structure Lab, University of Notre Dame, Indiana, USA. (March-April 1999)

Reviewed Publications

1. Halflife of ^{56}Ni in Cosmic Rays, **J.L. Fisker**, G. Martínez-Pinedo, K. Langanke, Eur. Phys. J. A5(1999)229
2. Shell-model based reaction rates for rp-process nuclei in the mass range $A=45-63$, **J.L. Fisker**, J. Görres, K. Langanke, G. Martínez-Pinedo, M.C. Wiescher, Atomic Data and Nuclear Data Tables 79(2001)241-292
3. Models for type I X-ray bursts with improved nuclear physics, S.E. Woosley, A. Heger, A. Cumming, R.D. Hoffman, J. Pruet, T. Rauscher, **J.L. Fisker**, H. Schatz, B.A. Brown, M. Wiescher, Astrophys. J. Suppl. 151(2004)75.
4. The nuclear reaction waiting points, ^{22}Mg , ^{26}Si , ^{30}S , and ^{34}Ar , and bolometrically double peaked type I X-ray bursts, **J.L. Fisker**, F.-K. Thielemann, and M. Wiescher, Astrophys. J. Lett. 608(2004)L61

Proceedings

1. Shell-model based thermonuclear (p, g) rates in the lower pf -shell, **J.L. Fisker**, J. Görres, K. Langanke, G. Martinez-Pinedo, M.C. Wiescher, Nucl. Phys. A688(2001)453c
2. The rp-process on compact binaries: Importance of exact parameters, **J.L. Fisker**, F. Rembges, V. Barnard, M.C. Wiescher, pp 569, The influence of binaries on stellar population studies, Kluwer Academic Publishers, Dordrecht, 2001.
3. Nuclear reaction rates in the thermonuclear runaway phase of accreting neutron stars, M.Wiescher, V. Barnard, **J.L. Fisker**, J. Görres, K. Langanke, G. Martinez-Pinedo, F. Rembges, H. Schatz, and F.-K. Thielemann, Eur. Phys. J. A15(2002)59-63
4. The transition to stable burning on an accreting neutron star, **J.L. Fisker**, W. Raphael Hix, M. Liebendörfer, and F.-K. Thielemann, Nucl. Phys. A718(2003)614c